Numerically optimized implementations, mitigation and simulations of Polarisation Mode Dispersion in real-time transmission systems.

Christos Braimiotis
Doctor of Philosophy

Aston University
June 2006

Aston University

Numerically optimized implementations, mitigation and simulations of Polarisation Mode Dispersion in real-time transmission systems

Christos Braimiotis

Doctor of Philosophy, May 2006

Thesis Summary

The aim of this thesis is to present numerical investigations of the polarisation mode dispersion (PMD) effect. Outstanding issues on the side of the numerical implementations of PMD are resolved and the proposed methods are further optimized for computational efficiency and physical accuracy. Methods for the mitigation of the PMD effect are taken into account and simulations of transmission systems with added PMD are presented.

The basic outline of the work focusing on PMD can be divided as follows. At first the widely-used coarse-step method for simulating the PMD phenomenon as well as a method derived from the Manakov-PMD equation are implemented and investigated separately through the distribution of a state of polarisation on the Poincaré sphere, and the evolution of the dispersion of a signal.

Next these two methods are statistically examined and compared to well-known analytical models of the probability distribution function (PDF) and the autocorrelation function (ACF) of the PMD phenomenon. Important optimisations are achieved, for each of the aforementioned implementations in the computational level. In addition the ACF of the coarse-step method is considered separately, based on the result which indicates that the numerically produced ACF, exaggerates the value of the correlation between different frequencies.

Moreover the mitigation of the PMD phenomenon is considered, in the form of numerically implementing Low-PMD spun fibres. Finally, all the above are combined in simulations that demonstrate the impact of the PMD on the quality factor (Q-factor) of different transmission systems. For this a numerical solver based on the coupled nonlinear Schrödinger equation is created which is otherwise tested against the most important transmission impairments in the early chapters of this thesis.

Keywords: Polarisation mode dispersion, Numerical physics, Probability distribution function (PDF), Autocorrelation function (ACF), Low-PMD spun fibres, optical transmission, Q-factor

For my parents

Acknowledgements

This research would not have been accomplished without the enormous contribution of a number of people that I wish to acknowledge.

First I would like to express my deepest gratitude to my supervisor Dr. Marc Eberhard. With his constant help, guidance, enthusiasm and his tireless efforts to explain various, numerical methods and physical effects in a clear and simple way, I managed to solve the problems that arose during the course of my work. Furthermore I would also like to express my sincere gratitude and appreciation for Prof. Keith Blow, without his important advice, encouragement, corrections and original ideas I would have been lost.

I also would like to thank our network manager Mr. Supun Athukorale for his enormous contribution in setting up an efficient computer system, to complete my work. I owe much gratitude to Dr. Ranjeet Bhamber for his significant advises in programming and code optimisation. Both have been important friends to me and supported me morally and socially during the course of my work.

I would also like to express my appreciation to Dr. Sonia Boscolo and Dr. Stanislav Derevyanko for many important conversations and suggestions on transmission effects and also for their friendship and encouragement. Further I would like to acknowledge Dr. Shoichiro Oda for fruitful conversations on polarisation artifacts, but mostly for his important friendship and kind character.

I would also like to express my gratitude to my parents and step-mother for their financial support but mostly for their contribution in my moral and personal growth up to this point.

Contents

List of Figures

Chapter 1

Introduction

1.1 Historical background

The increasing demand for higher information bandwidth resulted in a dramatic growth in the telecommunications industry over the recent years. The stimulation for this development, has been fuelled by the growth of the Internet. Services such as the email and online World Wide Web interactions, in a financial and social level have been widespread and common for almost any individual. Parallel to that the new global economy has introduced business and company models, that are heavily dependent on high data-rates driving the developing networks to operate at high speeds. It is important to remember that such networks exist to connect, multiple members of a certain group or organisation, as well as, to conduct group-to-group transactions. It is then obvious that the spectrum of demand can cover most of the infrastructure of modern communications including local area networks (LAN), metropolitan networks and wide area networks (WAN). Let us not forget that the new technological advances result in reduction of cost in the long run for the user, and this in turn fuels new demand and the need for new applications escalating the technological race. This is the main cause that the optical communications and processing seem so attractive as it is the only solution that undoubtedly can fulfil the high bit-rate expectations due to the enormous bandwidth capability it offers.

There is a pattern to the development of the structure of the optical networks being

deployed. Starting from the most dominant problem and as the demand and bit-rates become higher, incorporating more phenomena for research and troubleshooting.

Thus in the early days, clearly the loss was the dominant factor in optical transmission, with attenuation values which in the 1960s were greater than 1000 dB/km [1]. In 1970 , a huge step forward was achieved, by observing that at the region around the 0.632 μm wavelength range the intrinsic material scattering loss becomes very close to 20 dB/km [2]. Further investigating the problem in 1979 the authors of [3], produced a single-mode fibre with an extremely low-loss of 0.2 dB/km at 1.55 μm, where it is limited by Rayleigh scattering.

Continuously in 1986 a technical paper on low-loss rare-earth doped fibres [4], progressed into introducing the concept of erbium-doped fibre amplifiers (EDFA) as an attractive means to increase even further the transmission distance. Moreover EDFAs add amplified spontaneous emission (ASE), noise to the signal. Using such a system then increases the distance, provided that filtering is used and proper signal power.

At this point it should be mentioned, that the loss-related experiments and observations, refer to single-mode fibres. As this medium, was accepted to be more efficient in terms of the information data-rates. This due to fact that in multimode fibre, the different transmission paths of the propagating modes result in intermodal dispersion, as the velocities of propagation, of the various paths, are different, producing the spreading of the output pulse, rendering it inefficient for long distance transmission from the early days of optical transmission.

Similar to multimode, in single mode fibres dispersion exists, especially in the vicinity of 1.55 μm wavelength, which is the aim in terms of transmission having the lowest attenuation, but due to different underlying reasons. The two causes of intramodal dispersion are material and waveguide dispersion.

In material dispersion the signal disperses because the refractive index of the fibre is a function of the wavelength of the source. This in turn causes a wavelength dependence of the group-velocity which leads to pulse spreading for a single mode. On the other hand there is waveguide dispersion. According to the design of the fibre, a certain amount of power of the optical pulse propagates in the cladding, in different speed than the power in the core. Again as a result dispersion arises. More specifically

the wavenumber is given as the solution for the propagation eigenmodes of the fibre. As such it will vary depending on the frequency, which will eventually result in the dependence of the group velocity on the frequency parameter, even in the absence of material dispersion. Modern optical communications systems managed to attack the problem of dispersion, by either using dispersion shifted fibre (DSF) with approximately zero chromatic dispersion at 1.55 μm, or by using laser with a narrow spectral width, or even better by employing both methods. Another measure to overcome the problem is dispersion management (DM),by using dispersion compensating fibre (DCF) [5]. Following this approach at certain points of the fibre, after a DCF having an equal and opposite sign dispersion, to the one accumulated from the previous step, is inserted, the total dispersion is zero. But the absolute value of the dispersion per length is non-zero. Of course adding another fibre will introduce additional losses, this is why, this scheme should be accompanied by additional amplification.

At high optical powers, nonlinear effects start to become noticeable in an optical fibre. Provided that the rest of the effects can be compensated for, nonlinearities appear to be an important factor for long distance transmission, as the distortion that they might cause acts on a longer length scale than losses, noise and dispersion.

While in low bit-rate systems nonlinearities are not an important factor, with the advent of wavelength division multiplexing (WDM) systems and higher bit-rates, the amount of optical power is significant. Also erbium-doped fibre amplifiers installed in optical-fibre communication systems, replaced the electronic regenerators which were spaced every twenty kilometres or so. By doing so, the bottleneck of the limited bandwidth of the electronic components is removed, while the cost of installation and maintenance of such devices is eliminated. But in addition by including amplification in the optical domain the nonlinearity is allowed to reach the longer length scale that it is required in order for this phenomenon to become important.

The nonlinear-fibre optics date back to the invention of low-loss fibres [6]. The source of nonlinear effects is the nonlinear relation of the polarisation of the electric dipoles to the electric field [6, 7]. In this case the third order susceptibility invokes elastic effects, such as, third-harmonic generation, four-wave mixing, nonlinear refraction [7].

On the other hand there are inelastic effects, meaning that in this case the field transfers part of the energy that contains to the medium, such as in stimulated Raman scattering (SRS) and stimulated Brillouin scattering (SBS). In both these phenomena a photon in a higher frequency is annihilated to create a photon of a lower frequency and a phonon, so that the energy is conserved [6]. In SRS the phonon is optical while in SBS the phonon is acoustic. In the case of WDM systems the SRS will lead to a reduction in the power of a lower wavelength channel, with a transfer of energy to higher-wavelength channels. SRS can be limited if the power of the signal in each channel, remains below a certain threshold, depending on the number of channels and the separation between them as indicated in [8]. The other inelastic effect is SBS, in which case there is an absorption of an emitted acoustic phonon while the photon at lower frequency propagates in the opposite direction depleting the forward propagating signal. Again to reduce the SBS effect, the option would be to keep the power below the SBS threshold.

Nonlinear refraction results from the intensity dependence of the refractive index. This in turn, triggers nonlinear effects such as self phase modulation (SPM) which is important as it forms optical solitons in the anomalous dispersion regime [9] and cross-phase modulation (XPM), which it refers to the nonlinear phase shift induced to one field from another as they copropagate, such as in WDM systems.

In WDM systems the nonlinear refractive index also manifests itself in four-wave mixing. Four-wave mixing takes place in these systems, of low dispersion fibre and high overall power [10, 11]. If multiple wavelength channels are situated in the zero-dispersion point, three optical frequencies interact to produce a fourth frequency, which will grow depleting the rest of the channels, and cause severe crosstalk. A way around this problem is to use the DM technique [12, 13] explained earlier so that the dispersion will add-up to zero at some distance, while the fibre will be in the non-zero dispersion regime. Thus during the propagation of the signal, the conditions for four-wave mixing will not be satisfied.

Special attention should be given to optical solitons. In the anomalous group velocity dispersion (GVD) regime, the interplay between SPM and GVD gives rise to solitons, solitary travelling wave pulses. The mechanism by which this happens relies

on the fact that the high energy of the pulse modulates the refractive index, so that the SPM induced chirp, shifts the leading edge of the pulse to lower frequencies and thus higher speed, while at the same time the trailing edge is shifted at higher frequencies so that the speed in this part is reduced. This is counteracted by the action of a negative sign GVD. As mentioned the optical solitons appeared theoretically in [9] and later experimentally by Mollenauer, Stolen and Gordon [14]. Parallel to these Hasegawa and Tappert theoretically introduced the concept of dark soliton [15], as a dip in a bright uniform background, that can be formed in the normal-GVD regime. A third option is the dispersion-managed (DM) soliton [6]. Here the amplitude, the width and the frequency oscillate in a periodic manner.

Solitons however suffer from the effect of attenuation. The common solution to counteract losses on the transmission line are optical amplifiers such as EDFAs. The use of EDFAs affects the soliton transmission considerably, as the perturbation factor that is added by the ASE noise will influence all the soliton parameters, such as amplitude, position, frequency, and the phase of the input pulse.

Furthermore by adding noise there is a gradual degradation of the signal-to-noise ratio. But more important, there is timing jitter created by the noise factor of the system. This is less obvious than the immediate reduction of the quality of our transmission due to unwanted noise, but it can be explained, by having in mind that the frequency is changed because of the perturbation in the system. Then as the group velocity is dependent upon frequency, it is obvious, that the arrival time of the pulse will vary. This type of jitter is identified as Gordon-Haus timing jitter.

The experiment of [14] and the fascinating theory behind fibre nonlinear phenomena, stimulated further the growth of the field of ultrashort optical pulses and high-speed transmission through solitary waves of all three types, pulse, dark and DM solitons [16]-[25].

Applications on the cutting edge of technology emerge in favour of the field of nonlinear optics. Nowadays topics such as, optical routing through blocker solitons [26], spatiotemporal solitons called "light-bullets" [27], as well as, "slow-light" dubbed from the ability to control the group-velocity of light by nonlinear optical means in order to produce optical buffers and optical delay lines [28] and of course photonic

crystal fibres (PCF), optical fibres in which light is trapped by an array of air holes which run down the fibre length [29] with their rich nonlinear properties are a step closer toward all-optical processing.

Nowadays and moving on to higher-bit rates a new type of dispersion, classified as polarisation mode dispersion (PMD), became important due to the ellipticity and imperfections of optical fibres.

The appearance of polarisation effects during the transmission in the optical medium started in the early 1960s [30]. Further in late 70s the phenomenon has been revisited with papers such as in [31], referring to measurement techniques and the principles of polarisation evolution in single-mode fibres, through theory and experiment or referring to maintaining a constant polarisation by means of stress-induced, birefringence [32]. This work on keeping a constant polarisation, had as a higher aim, the improvement of heterodyne detection.

In 1978 Rashleigh and Ulrich [33] indicated that in any fibre, imperfections exist which cause the cylindrical symmetry to break. Thus the single-mode fibre can be considered a two-mode fibre, due to the fact that the refractive indices of propagation for the two orthogonal modes are different, and may exhibit mode dispersion, as even in the case of a single mode of propagation HE_{11}, the two group velocities of the two polarisations will vary.

Only after the positive aspect of optical amplification, and the mitigation of chromatic dispersion in fibres through DSF [34], the transmission reached higher lengths and gave the polarisation effects the opportunity to accumulate, and reach the length scale where they really become important. On the same time the data-rates reached to 10 Gb/s. If it is taken into account that the spread due to PMD is proportional to the square-root of the transmission length [6]. Then at 10 Gb/s, a typical value of spreading per length is 0.1~1 ps/$\sqrt{km}$, and at 1000 km that would produce a total spread of 3~30 ps, this would mean that the spread could be comparable to the pulse width of 100 ps. The problem seems worse if it is taken into account that the systems eventually will be upgraded to 40 Gb/s or higher. It is clear then that for long-haul transmission PMD is a limiting effect.

Moreover loss and chromatic dispersion contain an uncertainty related to manu-

facturing imperfections . In most cases though the probability dependence, will be minimum beyond a certain value for the parameters, of both these sources and thus predictable systems can be generated that can be designed for the worst case scenario. On the other hand PMD changes as a random process, dependent both upon wavelength and time. This requires a statistical treatment of the phenomenon as it varies from fibre to fibre or for the same fibre it varies randomly with the optical carrier frequency and ambient temperature [35]. Also it would be important to note that chromatic dispersion, can also vary with temperature these variations though are within the dispersion tolerance of the transponders. In addition we should mention another effect which depends on the polarization of the signal and causes additional impairments on the transmission. The polarization dependent loss (PDL) refers to the dependence of the loss of a link on the polarization state of the propagating wave. As such it causes fluctuations in the power evolution of the signal and thus it degrades further the signal-to-noise ratio.

Additionally, on systems that are already installed, the birefringence is really high. The problem is more severe in DSF fibres, which have been used mainly in networks due to their excellent behaviour regarding chromatic dispersion. As the core is smaller in DSF fibres they are more prone to errors caused by imperfections and ellipticity. It would be very costly to replace these links with new fibres, which would be optimised to reduce PMD to a certain degree or with polarisation maintaining fibres (PMF), fibres which preserve the state of polarisation, through an artificially increased birefringence which becomes dominant.

Taking into account the random nature of PMD, it should be noted that the system requirements for the PMD limitations can be formulated in different ways and that there is no international standard [36] or a specified way for compensating the problem. The probability densities of PMD have asymptotic tails extending to large impairments so it is not beneficial to prepare for the worst case but instead the transmission systems should be designed with a PMD outage probability in mind. And the alternative of compensation has the aim of reducing the outage probability rather than compensating exactly for PMD, which requires active components and is thus very costly. This is why one needs to examine thoroughly the statistics of PMD and the mechanisms behind it.

In the case of solitons, PMD combines with ASE, to reduce the quality of the performance of the transmission.

All these constitute the idea that efficient modelling of phenomena in optical fibre systems, is necessary, this is the reason that many telecommunication organisations now devote significant efforts to it. Especially in the case of PMD because of the inherent complexity of the subject, issues concerning optimized, in physical or computational terms, designs are still to be resolved. The work that follows is devoted to that particular aim, of providing computationally optimized implementations of PMD and including them in realistic transmission cases.

1.2 Thesis synopsis

The objective of this thesis is to provide and demonstrate numerically efficient methods for modelling PMD. Further the already existing models are compared to the proposed methods by providing statistical and numerical evidence. Additionally a numerical solver of the coupled nonlinear Shrodinger equation (CNLS), is implemented so that these different methods are incorporated and simulated within the context of real-time transmission systems, with all the important effects concerning optical transmission, such as nonlinearity, dispersion, losses and noise.

At first the coarse-step method for modelling polarisation mode dispersion is considered, where PMD is represented as a cascade of short fibre sections (waveplates), with fixed length, differential-group delay (DGD) which is the drift between the two polarisation modes and fixed principal states of polarisation (PSP). The sections are connected by polarisation scatterers, that give the coupling of the two orthogonal modes. The model is implemented and studied thoroughly through statistical tests. Modifications concerning the model have been considered and added to the existing method. The impact of such modifications on transmission are shown through simulation results.

An alternative and more physical model is also implemented. This model is derived by producing numerically the polarisation effect through the Manakov-PMD equation. It is continuously indicated that such an approach has been considered in the past by other groups, but it was rejected as being numerically inefficient, although physically

adequate, compared to the coarse-step approach. This model is further modified, so that the numerical obstacle that arose by using it, is overcome. The Manakov-PMD model, along with its modifications is analysed and studied through, the well known statistical models and compared to the coarse-step method.

In order to examine if the models are effective, they are used in transmission systems along with the rest of the well known limiting factors. For this purpose a vector-model is created and tested methodically, by introducing each factor at a time and investigate if the simulator corresponds properly to the limiting cases.

More specifically the report follows the structure presented next.

In chapter 1 a historical perspective of the optical communications in general was given. The limiting factors were outlined and the importance of PMD was stressed.

In chapter 2 the CNLS is derived and the vector model generated from that formula is tested by performing the limiting cases on that and compared to theoretical descriptions for each case.

Following in chapter 3 the theoretical background behind the PMD phenomenon is described, in the time domain as well as in the frequency domain following the Poincaré sphere formalism.

In chapter 4 the existing methods of simulating PMD are presented. The coarse-step method namely is analysed through the demonstration of its properties on the Poincaré sphere, through the theoretical derivation of the artificial rescaling, this method induces and through numerical investigations of the dispersion of a signal. Next in chapter 5 the Manakov-PMD method is examined in a similar way. Here the physical accuracy of this method is presented and numerical investigations aim to a comparison with the coarse-step method.

Statistical analysis of these two implementations follows in chapter 6, compared with the appropriate analytical models. The limitations or advantages of each method will be demonstrated here. In the case of the Manakov-PMD equation the way to numerically optimise this method is presented.

In chapter 7 the method for eliminating the side-peaks of the Autocorrelation function (ACF) of the coarse-step method is shown through the numerical results. And in chapter 8 the mitigation of PMD through Low-PMD fibres is considered.

Continuously in chapter 9 simulations of optical transmission systems are given and examined through the Q-factor parameter. The penalties that PMD induces on a system are evident.

Finally in chapter 10 the conclusion of this thesis is included.

Chapter 2

Theory of optical transmission

2.1 Introduction

One of the aims of this project has been to determine the impact of the effects such as loss, dispersion and nonlinearity with respect to the scalar and the vector model, and investigate any differences between these two. For this purpose a numerical solver of the CNLS and the nonlinear shrödinger (NLS) equation was implemented using the split-step Fourier method (Appendix A) and tested on the limiting cases for each of these effects to a good approximation with theory. In this chapter a derivation of the equations used is given along with simulations on the Q-factor of these systems.

2.2 Theoretical background

The transmission of a signal along the path of an optical fibre, is described through the NLS. The NLS equation can be derived from the Maxwell's relations which govern all electromagnetic phenomena.

Where $\mathbf{E}, \mathbf{H}$ are the electric and magnetic field vectors while $\mathbf{D}, \mathbf{B}$ are the electric and magnetic displacement. The current density is represented by $\mathbf{J}$, while ρ_f represents the charge density. In an optical fibre in the absence of free charges $\mathbf{J} = 0$, $\rho_f = 0$.

$$\nabla \times \mathbf{E} = -\frac{\partial \mathbf{B}}{\partial t} \tag{2.1}$$

$$\nabla \times \mathbf{H} = \mathbf{J} + \frac{\partial \mathbf{D}}{\partial t} \tag{2.2}$$

$$\nabla \cdot \mathbf{D} = \rho_f \tag{2.3}$$

$$\nabla \cdot \mathbf{B} = 0 \tag{2.4}$$

With the additional equations,

$$\mathbf{D} = \epsilon_0 \mathbf{E} + \mathbf{P} \tag{2.5}$$

$$\mathbf{B} = \mu_0 \mathbf{H} + \mathbf{M} \tag{2.6}$$

where $\mathbf{P}$ and $\mathbf{M}$ are the electric and magnetic field polarisation, with $\mathbf{M} = 0$ as the optical fibre medium is nonmagnetic. Also ϵ_0, μ_0 are the vacuum permitivity and vacuum permeability respectively. The electric field polarisation $\mathbf{P}$ has a linear and a nonlinear response. Thus,

$$\mathbf{P} = \mathbf{P}_L + \mathbf{P}_{NL} \tag{2.7}$$

This relation can be expanded further into a power series of $\mathbf{E}$,

$$
\begin{aligned}
\mathbf{P} = {} & \int_{-\infty}^{t} \epsilon_0 \chi^{(1)}(\mathbf{r}, t - t_1) \cdot \mathbf{E}(\mathbf{r}, t_1) dt_1 \\
& + \iint_{-\infty}^{t} \epsilon_0 \chi^{(2)}(\mathbf{r}, t - t_1, t - t_2) : \mathbf{E}(\mathbf{r}, t_1) \mathbf{E}(\mathbf{r}, t_2) dt_1 dt_2 \\
& + \iiint_{-\infty}^{t} \epsilon_0 \chi^{(3)}(\mathbf{r}, t - t_1, t - t_2, t - t_3) \vdots \mathbf{E}(\mathbf{r}, t_1) \mathbf{E}(\mathbf{r}, t_2) \mathbf{E}(\mathbf{r}, t_3) dt_1 dt_2 dt_3
\end{aligned} \tag{2.8}
$$

In Eq. 2.8 the first term amounts for the linear polarisation while the two terms that follow represent the nonlinear polarisation. Where $\chi^{(1)}, \chi^{(2)}, \chi^{(3)}$ are the first, second and third order susceptibility tensors. For the case of silica glass the second order nonlinearity that is caused by $\chi^{(2)}$ equals zero because this material is centrosymmetric. Equation 2.8 by taking into account only instantaneous effects and neglecting self-steepening and Raman scattering, can equivalently then be written as,

$$\mathbf{P} = \int_{-\infty}^{t} \epsilon_0 \chi^{(1)}(\mathbf{r}, t - t_1) \cdot \mathbf{E}(\mathbf{r}, t_1) dt_1 + \epsilon_0 \chi^{(3)} \vdots \mathbf{EEE} \qquad (2.9)$$

From the above the propagation equation is derived as follows. Taking the cross-product of 2.1, one writes

$$
\begin{aligned}
\nabla \times \nabla \times \mathbf{E} &= -\frac{\partial(\nabla \times \mathbf{B})}{\partial t} \\
\nabla \times \nabla \times \mathbf{E} &= -\mu_0 \frac{\partial(\nabla \times \mathbf{H})}{\partial t} \\
\nabla \times \nabla \times \mathbf{E} &= -\mu_0 \epsilon_0 \frac{\partial^2 \mathbf{E}}{\partial t^2} - \mu_0 \frac{\partial^2 \mathbf{P}}{\partial t^2} \qquad (2.10)
\end{aligned}
$$

Continuously, Eq. 2.10 is Fourier transformed. This implies that the operator $\frac{\partial}{\partial t}$ will be transformed to $i\omega$. Following a major simplification as in [6], that is, assuming that $\mathbf{P}_{NL}$ is a small perturbation at this stage to reduce the general complexity of the derivation, then,

$$\nabla \times \nabla \times \tilde{\mathbf{E}}(\mathbf{r}, \omega) - \epsilon(\omega) \frac{\omega^2}{c^2} \tilde{\mathbf{E}}(\mathbf{r}, \omega) = 0 \qquad (2.11)$$

The dielectric constant $\epsilon(\omega) = 1 + \tilde{\chi}^{(1)}(\omega)$ and $c = 1/\sqrt{\epsilon_0 \mu_0}$. With $\tilde{\mathbf{E}}(\mathbf{r}, \omega), \tilde{\chi}^{(1)}(\omega)$ being the Fourier transforms of the field and the susceptibility respectively. And given by,

$$\tilde{\mathbf{E}}(\mathbf{r}, \omega) = \int_{-\infty}^{\infty} \mathbf{E}(\mathbf{r}, t) \exp(i\omega t) dt \qquad (2.12)$$

$$\tilde{\chi}^{(1)}(\omega) = \int_{-\infty}^{\infty} \chi(\mathbf{r}, t) \exp(i\omega t) dt \qquad (2.13)$$

The dielectric constant is in general given by $\epsilon(\omega) = (n + i\alpha c/2\omega)^2$ with α being the absorption constant. Setting $\alpha = 0$ at this point, as the attenuation will be included later on and since at the wavelength region of interest optical losses are low, and taking

into account the identity $\nabla \times \nabla \times \mathbf{E} = \nabla(\nabla \cdot \mathbf{E}) - \nabla^2\mathbf{E}$, then 2.11 concludes to the following,

$$\nabla^2\tilde{\mathbf{E}}(\mathbf{r},\omega) + \beta^2(\omega)\tilde{\mathbf{E}}(\mathbf{r},\omega) = 0 \tag{2.14}$$

The parameter $\beta = (n(\omega)\omega/c) = \omega\sqrt{\mu_0\epsilon}$ represents the propagation constant. Assuming that the electric field has only one component, modelling the scalar approximation, $\mathbf{E}$ can be written as,

$$\mathbf{E}(z,t) \;=\; \left[E(z,t)exp(i\beta_0 z - i\omega_0 t) + \text{c.c.}\right] \tag{2.15}$$

Here $E(z,t)$ represents the slowly varying, complex amplitude, envelope of the wave and β_0, ω_0 are the wavenumber and angular frequency of the carrier. According to the same approximation the operators on the transverse components for a Cartesian coordinate system disappear, $\partial/\partial x = \partial/\partial y = 0$. In addition the rapid variation of $\frac{\partial^2}{\partial z^2}$ is neglected since $E(z,t)$ is the slowly varying. Thus the propagation equation is transformed as follows,

$$i\frac{\partial\tilde{E}}{\partial z} + (\beta - \beta_0)\tilde{E} = 0 \tag{2.16}$$

The factor $\beta^2 - \beta_0^2$ was approximated by $2\beta_0(\beta - \beta_0)$. With the propagation constant $\beta = \beta(\omega)$ and the slowly varying envelope $\tilde{E} = \tilde{E}(z, \omega - \omega_0)$ and finally the field having the Fourier transform,

$$\tilde{\mathbf{E}}(z,\omega) \;=\; \tilde{E}(z, \omega - \omega_0)\exp(i\beta_0 z) \tag{2.17}$$

At this stage nonlinearity which has been neglected for the sake of simplicity, is included. The nonlinear factor arises from the dependence of the polarisation of the medium to the power of the field. This nonlinear polarisation as mentioned, is generally

described by the third term of the right hand side of Eq. 2.8. Effectively this creates a perturbation of the refractive index, giving rise to a nonlinear term in the equation describing this quantity. Thus

$$\tilde{n}(\omega) = n(\omega) + \tilde{P}_{NL} \tag{2.18}$$

Referring only to nonlinear refraction the nonlinear term will be proportional to $n_2|E|^2$. With $|E|^2$ being the power of the field and

$$n_2 = \frac{3}{8n(\omega)} Re(\chi^{(3)}_{xxxx}) \tag{2.19}$$

As the propagation constant and the refractive index are related Eq. 2.18 is written as,

$$\frac{c\beta}{\omega} = n(\omega) + n_2|E|^2$$
$$\text{or}$$
$$\beta = \frac{\omega n(\omega)}{c} + \frac{n_2|E|^2\omega}{c} \tag{2.20}$$

The wavenumber β is thus also a function of power and one may write,

$$\beta = \beta(\omega, |E|^2) \tag{2.21}$$

Expanding this around the carrier frequency wavenumber

$$\beta - \beta_0 = \frac{\partial\beta}{\partial\omega}(\omega - \omega_0) + \frac{1}{2}\frac{\partial^2\beta}{\partial\omega^2}(\omega - \omega_0)^2 + \frac{\partial\beta}{\partial|E|^2}(|E|^2) \tag{2.22}$$

The derivatives of the wavenumber with respect to the frequency and amplitude are evaluated at $\omega = \omega_0$, $|E| = |E_0|$. Substituting this expression in Eq. 2.16, and Fourier

transforming to the time domain so that $\omega - \omega_0$ changes to $i\partial/\partial t$, this produces,

$$i\left(\frac{\partial E}{\partial z} + \beta'\frac{\partial E}{\partial t}\right) - \frac{\beta''}{2}\frac{\partial^2 E}{\partial t^2} + \frac{\partial \beta}{\partial |E|^2}(|E|^2)E = 0 \qquad (2.23)$$

The next step is to include the loss term through the absorption coefficient which has not been considered thus far and to transform the last term of Eq. 2.23 by differentiating 2.20 and dividing this by the effective area of the fibre which has been defined specifically for calculating nonlinear effects as explained in [37] - [39] and represents the portion of the energy of the modal distribution coupled to the core,

$$A_{eff} = \frac{(\int\int_{-\infty}^{\infty} |F(x,y)|^2 dx dy)^2}{(\int\int_{-\infty}^{\infty} |F(x,y)|^4 dx dy)} \qquad (2.24)$$

Equation 2.23 then results in,

$$i\left(\frac{\partial E}{\partial z} + \beta'\frac{\partial E}{\partial t}\right) - \frac{\beta''}{2}\frac{\partial^2 E}{\partial t^2} + \gamma(|E|^2)E + \frac{ia}{2}E = 0 \qquad (2.25)$$

And,

$$\gamma = \frac{n_2 \omega_0}{c A_{eff}} \qquad (2.26)$$

Identifying the terms, $\frac{\partial \beta}{\partial \omega} = \beta' = 1/v_g$ is the reciprocal of the group velocity at which the slowly varying envelope travels, $\frac{\partial^2 \beta}{\partial \omega^2} = \beta''$ is the group velocity dispersion responsible for pulse broadening the term in γ results in nonlinear refraction and last the α term represents the attenuation coefficient. Where $E = E(z,t)$ defined as the slowly varying envelope in the time domain. To define the A_{eff} the modal distribution $F(x,y)$ was used, which is included in the equations if one assumes a general equation for the field of the form

$$\mathbf{E}(\mathbf{r}, t) = F(x, y) E(z, t) \exp(i\beta_0 z - i\omega_0 t) \tag{2.27}$$

Equation 2.25 describes a scalar model. In this case the effects of polarisation are not included. For a birefringent fibre the field in general is defined as,

$$\begin{aligned}
\mathbf{E}(\mathbf{r}, t) &= \tilde{x}(F_1(x, y) E_x(z, t) \exp(i\beta_{0x} z - i\omega_0 t)) \\
&+ \tilde{y}(F_2(x, y) E_y(z, t) \exp(i\beta_{0y} z - i\omega_0 t)) + \text{c.c.}
\end{aligned} \tag{2.28}$$

The evolution of $E_x(z, t), E_y(z, t)$ can be determined exactly as in the scalar case, with the only difference that one has to expand each propagation constant $\beta_x(\omega), \beta_y(\omega)$ separately. This in turn results in two equations. Furthermore the nonlinear polarisation in this case is composed of two terms, one for each polarisation,

$$\mathbf{P}_{NL} = \chi^{(3)} \vdots \mathbf{EEE} = (\tilde{x} P_x + \tilde{y} P_y) \exp(-i\omega_0 t) + \text{c.c} \tag{2.29}$$

Each component expanded produces [6, 40],

$$P_x = \frac{3\epsilon_0 \chi^{(3)}_{xxxx}}{3} \left[\left(|E_x|^2 + \frac{2}{3}|E_y|^2 \right) E_x + \frac{1}{3}(E_x^* E_y) E_y \right] \tag{2.30}$$

$$P_y = \frac{3\epsilon_0 \chi^{(3)}_{xxxx}}{3} \left[\left(|E_y|^2 + \frac{2}{3}|E_x|^2 \right) E_y + \frac{1}{3}(E_y^* E_x) E_x \right] \tag{2.31}$$

This in effect introduces a different nonlinear perturbation of the refractive index, than in the scalar case. As determined below,

$$\Delta n_x = n_2 \left(|E_x|^2 + \frac{2}{3}|E_y|^2 \right) \tag{2.32}$$

$$\Delta n_y = n_2 \left(|E_y|^2 + \frac{2}{3}|E_x|^2 \right) \tag{2.33}$$

In these expressions the first term introduces SPM as in the scalar case while the second term results in XPM because of the dependence of the power of the orthogonal polarisation, on the intensity of the current polarisation component. The last term in Eq. 2.30, 2.31, results in degenerate four-wave mixing, although the phenomenon of four-wave mixing has not been considered in this work it is included in this derivation in favour of completion. Assuming that $\beta_x'' = \beta_y'' = \beta''$ and γ is the same, as the wavelength λ is the same for the two polarisations, then one writes for the two polarisations,

$$
i\left(\frac{\partial E_x}{\partial z} + \beta_x'\frac{\partial E_x}{\partial t}\right) - \frac{\beta''}{2}\frac{\partial^2 E_x}{\partial t^2} + \frac{ia}{2}E_x
$$
$$
= -\gamma(|E_x|^2 + \frac{2}{3}|E_y|^2)E_x - \frac{1}{3}(E_x^*E_y)E_y\exp[-2i(\beta_{0x} - \beta_{0y})] \quad (2.34)
$$
$$
i\left(\frac{\partial E_y}{\partial z} + \beta_y'\frac{\partial E_y}{\partial t}\right) - \frac{\beta''}{2}\frac{\partial^2 E_y}{\partial t^2} + \frac{ia}{2}E_y
$$
$$
= -\gamma(|E_y|^2 + \frac{2}{3}|E_x|^2)E_y - \frac{1}{3}(E_y^*E_x)E_x\exp[2i(\beta_{0x} - \beta_{0y})] \quad (2.35)
$$

The terms in Eq. 2.34,2.35 are defined as in Eq. 2.25. The different β' indicate that the signal undergoes PMD since the two wave-envelopes each for every polarisation travel with different group velocities. And we define also the quantity,

$$
\Delta\beta = \beta_{0x} - \beta_{0y} \quad (2.36)
$$

indicating the modal birefringence of the fibre. Finally the term in γ indicates the nonlinearity, and the last term on the right hand side degenerate four-wave mixing. The numerical simulators implemented according to Eq. 2.25, for the scalar case, and Eq.2.34, 2.35 for the vector case, are tested for each phenomenon individually. These test cases are presented next.

2.3   Optical attenuation

Loss is a fundamental limiting factor for any optical system. The power attenuation inside the system can be translated by the following formula which can be derived from

the NLS or the CNLS, assuming that the rest of the effects can be neglected,

$$\frac{dP}{dz} = -\alpha P \tag{2.37}$$

where α is the attenuation coefficient, operating on the optical power. This equation gives the P_{out} in terms of the input power.

$$P_{out} = P_{in} exp(-\alpha L) \tag{2.38}$$

several factors contribute physically to losses, these are mentioned below.

2.3.1 Material absorption

Material absorption is divided in two major categories intrinsic and extrinsic. Intrinsic material absorption, can be defined as the loss related to the silica material which absorbs the energy of the signal in the ultraviolet region through electronic resonances and in the infrared region through vibrational resonances. The impurities existing in the material, result in extrinsic absorption. In particular the impurity of OH-ions lead to an extremely high loss in the area of 1.4 μm.

2.3.2 Rayleigh Scattering

Rayleigh Scattering is the loss mechanism arising from local fluctuations in the density of the material. These fluctuations lead to disturbances in the refractive index, that affect the propagation of light. Rayleigh fluctuations are of intrinsic nature and present the "floor" loss limit in silica optical fibres.

2.3.3 Fibre imperfections

Obvious loss factors can be fibre imperfections such as unwanted bending or splicing of the fibre, as well as scattering at the core-cladding interface as outlined in [41].

2.3.4   Simulations

The following features were used for the loss-limited case. The map consisted of stan-
dard single mode fibre, with a length of 1 km, with a dispersion parameter of 0ps/nm
· km, a dispersion slope of 0 ps/km·nm^2, while the effective area of the fibre was
$A_{eff} = 10000$ μm^2, so that the nonlinearities are set to zero. The main effect on
the transmission was the loss that was set to 0.2 dB/km. The system was tested for
bit-rates of 10 Gbit/s and 40 Gbit/s. These were represented, respectively as a pseudo-
random bit-pattern of 2^6 bits in a time window of 6.4 ns with a resolution of 2^{11} points
for the bit-rate of 10 Gbit/s and as 2^8 bits for the same time width with a resolution
of 2^{13} points in total for the case of 40 Gbit/s. An RZ signal was used, with Gaussian
pulses of peak power of 1 mW for both cases, and a $T_{fwhm} = 33$ ps for 10Gbit/s and
$T_{fwhm} = 10$ ps for the case of 40Gbit/s. The effect of loss on the Q-factor can be seen
in figure 2.1. It is worth mentioning at this point that the Q-factor calculation for
all the effects in optical transmission is given by the well-known formula of Eq. 2.39,
where σ_1^2 , σ_0^2 are the noise variances depending upon the shot noise and thermal noise,
while μ_1 , μ_0 is the average value around which the power fluctuates from bit-to-bit for
the for the ones and zeros respectively.

$$Q = \frac{\mu_1 - \mu_0}{\sigma_0 + \sigma_1} \qquad (2.39)$$

The theoretical model for the loss-limited case was given by the following equation,

$$Q(z) = Q(0) \exp(-0.046L) \qquad (2.40)$$

Where Q(0) is taken empirically from the simulation and the factor of 0.046 is
derived from $\alpha = \alpha_{dB}/4.343$. Further the Q-factor decays exponentially with the
distance as expected for this case, alike the power of the signal. There is no difference
between the vector and the scalar model. Moreover the cases for 10 Gbit/s and 40
Gbit/s present the same decay.
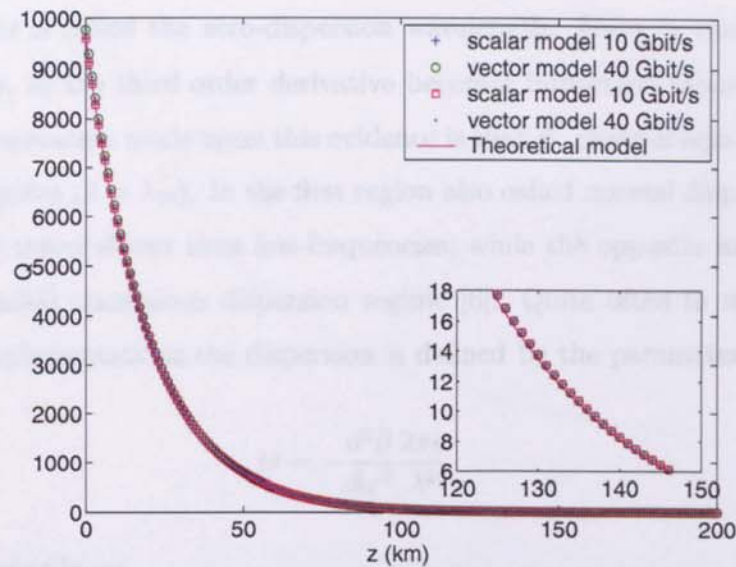
Figure 2.1: Q factor - loss limited case for 10Gbit/s and 40Gbit/s for the scalar and vector simulator compared with the analytical model.

2.4 Chromatic dispersion

2.4.1 Theoretical background

Dispersion indicates in general the spreading of the pulses in a bit-pattern and is separated in two kinds. Intermodal which is caused due to the fact that different modes travel in different group velocities, and intramodal, which is further separated in intrinsic chromatic dispersion and waveguide dispersion. Waveguide dispersion describes the phenomenon where the light coupled in the cladding travels faster than the light confined in the core [42]. Chromatic dispersion relates to the fact that different, components in the spectrum travel at different velocities due to the frequency dependence of the refractive index [6]. Chromatic dispersion plays a critical role for short optical pulses and higher bit-rates, where there exist larger spectral content, that results into a greater difference in the velocities. In the case where the nonlinearity is set to zero, in the absence of the Kerr effect and with no dispersion compensating fibre, the dispersion phenomenon can induce severe penalties to the transmission.

The effect of chromatic dispersion, can be obtained analytically, by expanding the wavenumber around a central frequency ω_0. Thus the wavenumber β, can be expressed by Eq. 2.22. The term $\frac{d^2\beta}{d\omega^2}$ represents the group velocity dispersion(GVD) parameter.

For the value of wavelength $\lambda_D = 1.27\mu m$, the second derivative, $\beta'' = \frac{d^2\beta}{d\omega^2} = 0$ ps^2/km [6]. This is called the zero-dispersion wavelength. Even in this case though dispersion exists, as the third order derivative becomes important around this region [6]. A second observation made upon this evidence is that β'' changes sign from positive ($\lambda < \lambda_D$) to negative ($\lambda > \lambda_D$). In the first region also called normal dispersion regime high-frequencies travel slower than low-frequencies, while the opposite happens in the second region called anomalous dispersion regime [6]. Quite often in numerical and experimental implementations the dispersion is defined by the parameter [6]

$$D = -\frac{d^2\beta}{d\omega^2}\frac{2\pi c}{\lambda^2} \qquad (2.41)$$

2.4.2 Simulations

The characteristics of the optical transmission were the following A standard single mode fibre with a dispersion parameter D of 20ps/nm/km, no higher order dispersion terms, loss 0 dB/km and A_{eff} of $10000\mu m^2$. It should be mentioned that A_{eff} has been assigned an unrealistic value as in the loss-limited system implemented previously, so that the nonlinearities are eliminated through Eq. 2.26. In the presence of GVD, in the normal regime and in the absence of any other effects the width of a transmitted Gaussian pulse increases according to [6],

$$T_1(z) = T_0[1 + (z/L_D)^2]^{1/2} \qquad (2.42)$$

or equivalently for the peak power of the pulse to decreases as described by the following expression,

$$P_1(z) = P_0/[1 + (z/L_D)^2]^{1/2} \qquad (2.43)$$

with T_0 being the initial width of a pulse, related to the T_{fwhm} as $T_{fwhm} = 1.665T_0$ and the dispersion length $L_D = T_0^2/|\beta''|$. For this purpose a single Gaussian pulse of peak power 1 mW and $T_{fwhm} = 33$ ps, was launched and its peak power monitored within a distance of 100 km, as shown in figure 2.2 where the theoretical model follows closely the evolution of the numerical solution.
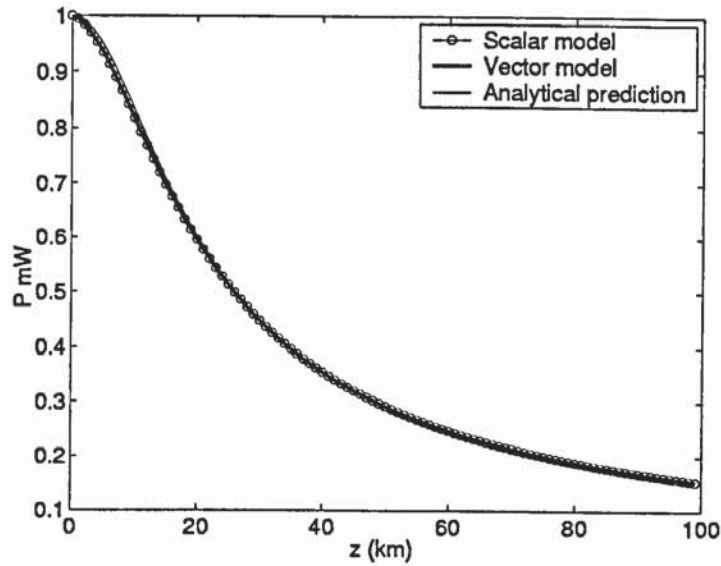
Figure 2.2: Peak power evolution for a dispersion limited system.

Furthermore the Q-factor of the system was obtained by using identical bit-patterns to those used for the loss-limited case.

One would expect the Q-factor to follow closely the model presented for the peak power of a pulse as it is shown to be true for the results of the loss-limited case. However this appears to deviate from the theoretical expectation for a single pulse. The reason for this is quite clear, if one obtains the eye diagram for both of these cases one can observe that the effect that distorts the Q-factor is intersymbol interference. That is the adjacent bits distort each other by spreading their energy beyond the assigned bit-slot. This effect commences very fast especially for higher bit-rates and gives rise to unwanted artifacts and peaks on the Q-factor. These peaks of course should not be considered as an improvement but rather a false indication of the receiver perceiving the unwanted increase in power in some bit-slots as bits. Naturally as the transmission progresses this extra distortion worsens and deteriorating further the Q-factor. The eye-diagrams produced for both the 10Gbit/s and 40Gbit/s case are presented in figure 2.4 . Finally one should also observe that the quality of the system deteriorates faster for the 40 Gbit/s case, as predicted, because of the rich spectral content in this system.
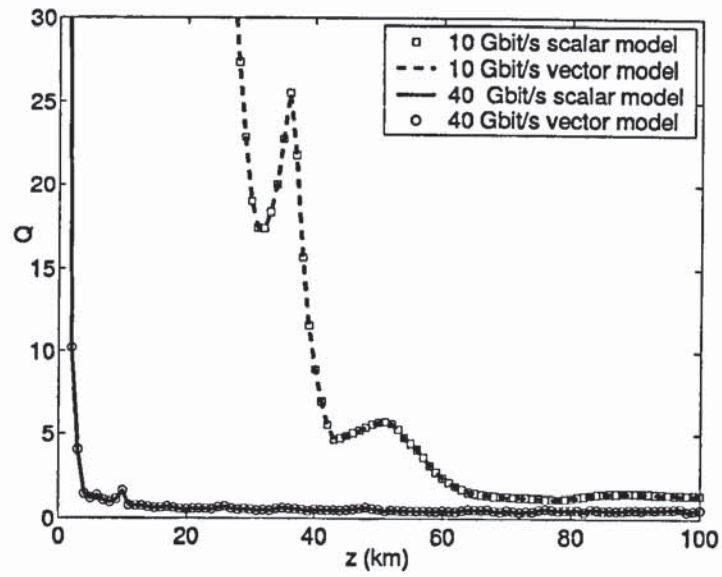
Figure 2.3: Q factor - loss limited case for 10Gbit/s and 40Gbit/s for the scalar and vector solutions compared with the analytical model.
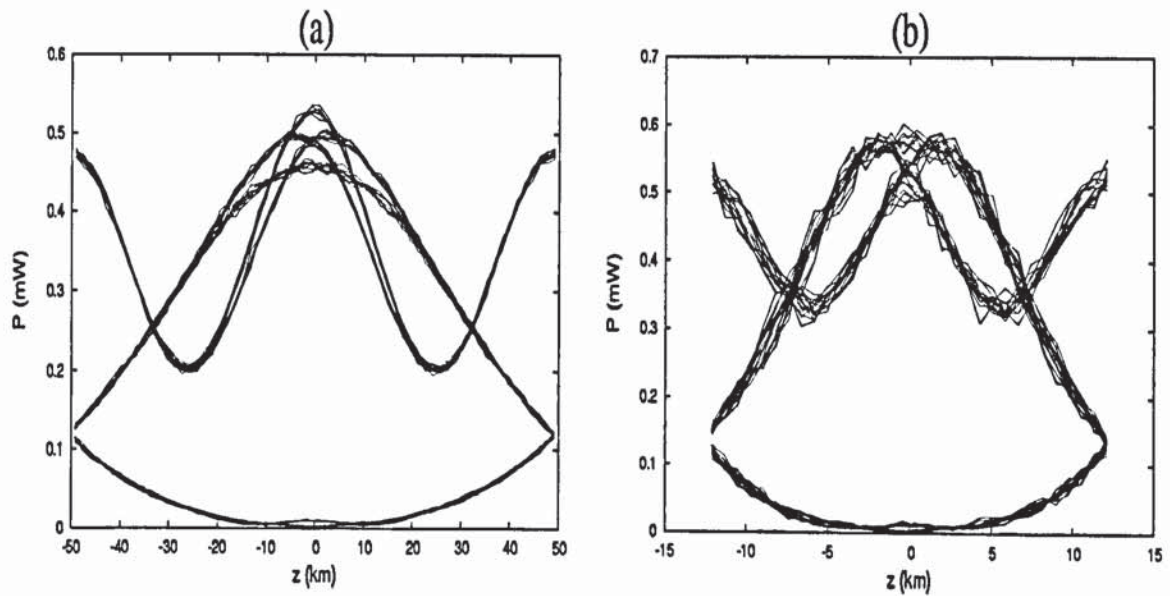
Figure 2.4: Eye-diagram plots for (a) 10 Gbit/s at 30km (b) 40 Gbit/s at 2km.

2.5 Optical noise

Initially in order to overcome the limitations imposed by optical attenuation, opto-electronic equipment was utilised. These optoelectronic repeaters were based on the principle, of optical-to-electrical conversion and subsequent regeneration of the signal before it is converted back to the optical domain. Such an operation added greatly to the cost and complexity of the transmission system. The alternative approach is to use optical amplification which is based on the stimulated emission principle. As this does not require conversion to the electrical domain it reduces the bulk of the equipment. There are several numerical models, that correspond to different types of optical amplifiers, such as semiconductor laser amplifiers, erbium doped fibre amplifiers (EDFAs), Raman and Brillouin amplifiers. In this numerical solver, the simplest model is considered as described below.

2.5.1 Optical amplifier model

The optical amplifier implementation utilised here, is adding gain to the signal according to Eq.(2.44),

$$G = \frac{P_{out}}{P_{in}} = \exp(gL) \tag{2.44}$$

The factor g is the individual gain coefficient for each amplifier and G is defined as the amplification factor. The amplifier will add noise according to a probability distribution, with variance $\sigma^2 = <(\Delta I)^2>$, with ΔI representing current fluctuations caused by noise [1]. In general the type of noise contributing to the variance equation, can be of thermal origin σ_T^2, shot noise σ_s^2, beating of signal and spontaneous emission noise σ_{sig-sp}^2, beating of spontaneous emission noise against itself σ_{sp-sp}^2 and finally beating of shot noise and spontaneous emission noise σ_{s-sp}^2. So that the total can be expressed as [43, 44, 45],

$$\sigma^2 = \sigma_T^2 + \sigma_s^2 + \sigma_{sig-sp}^2 + \sigma_{sp-sp}^2 + \sigma_{s-sp}^2 \tag{2.45}$$

2.5.2   Simulations

For the purposes of this simulation a standard single mode fibre with a dispersion parameter D of 0ps/nm/km, no higher order dispersion terms, loss 0.2 dB/km and A_{eff} of 10000 μm^2 was used. In order to introduce noise, in-line amplification was used every 40km. The parameters for each individual amplifier are a gain of 8 dB so that it compensates for the same exact amount of optical attenuation and a spontaneous emission factor of 2, the amount of noise added was determined by the spectral density $S_n = n_{sp}(G - 1)h\nu$ where $h\nu$ the photon energy, $h = 6.63 * 10^{-34} J.s$ the Planck's constant, ν the signal wavelength, G the gain of the amplifier and n_{sp} the spontaneous-emission factor related to the noise figure by $F_n \approx 2n_{sp}$. The bit-rates tested are again a 10 Gbit/s and a 40 Gbit/s rates with the same evidence as in the loss-limited system.
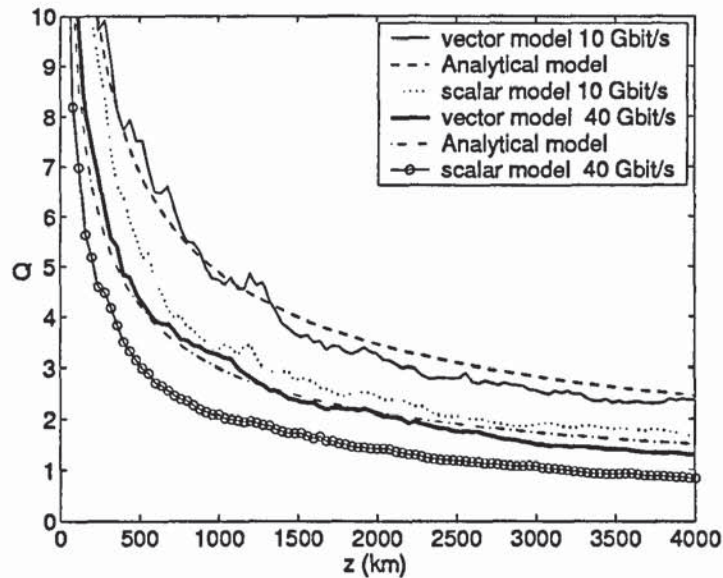
Figure 2.5: Q factor - noise limited case for 10Gbit/s and 40Gbit/s for the scalar and vector solutions compared with the analytical model.

The theoretical model introduced follows an inverse square root relation to the distance which is expressed as in the following equation,

$$Q(z) = \frac{Q(0)}{\sqrt{(z)}} \tag{2.46}$$

The observation used to produce this equation originates from the fact, that the Q-factor is inversely proportional to the standard deviation of noise which in turn

is proportional to the square root of the noise power accumulated over a specified distance. The original point $Q(0)$ depends on the bit-rate the signal power and the characteristics of the receiver but can also be substituted empirically from the evidence of the simulation.

Further observations that should be noted on the diagram is that the 40 Gbit/s curves will drop below the threshold of $Q = 6$ approximately at twice the rate of the 10 Gbit/s graphs. This can be explained because of the square root dependence, of the standard deviation of noise to the bandwidth of the signal, and thus a factor of 2 will be introduced in the case of the transition from 10 to 40 Gbit/s. Finally one notices the difference between the scalar and the vector model. This is well-known [46, 47] and accounts for the over-estimation of the signal-noise beating term for the scalar case.

2.6 Nonlinear effects

As mentioned earlier nonlinear effects stem from the dependence of the optical fibres on the strength of the electromagnetic radiation. Thus the polarisation of the fibre that depends on the orientation of the molecules of the medium varies in a nonlinear manner as in Eq. 2.9.

2.6.1 Self-phase and cross-phase modulation

The third order susceptibility $\chi^{(3)}$ gives rise to a dependence of the refractive index on the power of the electric field. The effects that result then are self-phase modulation(SPM), cross-phase modulation (XPM) and four-wave mixing (FWM). The phenomenon of SPM is the term used to express the intensity dependence of the phase of the signal to its own intensity. This causes a distortion in the frequency domain but the temporal pulse shape remains intact in the absence of chromatic dispersion. For a scalar model one writes,

$$\phi = n(\omega) + \frac{n_2\omega_0}{cA_{eff}}|E|^2 \tag{2.47}$$

The effect of XPM results from the copropagation of two or more signals in the optical fibre. In this case each signal will depend on the intensity of the others. In a

vector model where one solves for the CNLS and thus having a copropagation of two waves, both the effects of SPM and XPM affect the nonlinear phase as noted below,

$$\phi_{NL(x)} = \frac{n_2 \omega_0}{c A_{eff}} (|E_x|^2 + \frac{2}{3}|E_y|^2) \tag{2.48}$$

$$\phi_{NL(y)} = \frac{n_2 \omega_0}{c A_{eff}} (|E_y|^2 + \frac{2}{3}|E_x|^2) \tag{2.49}$$

Thus after a distance $L = z_{init} + N\Delta z$ where Δz the step size and assuming that the rest of the effects can be neglected. The field will be given by,

$$E(L,t) = \exp(\frac{i n_2 \omega_0}{c A_{eff}} N|E|^2) E(z_{init}, t) \tag{2.50}$$

$$E_x(L,t) = \exp(\frac{i n_2 \omega_0}{c A_{eff}} N(|E_x|^2 + \frac{2}{3}|E_y|^2)) E_x(z_{init}, t) \tag{2.51}$$

$$E_y(L,t) = \exp(\frac{i n_2 \omega_0}{c A_{eff}} N(|E_y|^2 + \frac{2}{3}|E_x|^2)) E_y(z_{init}, t) \tag{2.52}$$

Thus for a transmission system limited only by SPM and XPM the nonlinear phase $(\phi_{NL}, \phi_{NL(x)}, \phi_{NL(y)})$ will evolve linearly with distance.

2.6.2 Simulations

The fibre model used for the demonstration of SPM and XPM had the following characteristics a D of 0 ps/nm/km, attenuation parameter 0.2 dB/km and an A_{eff} of 100 μm^2. As mentioned earlier the temporal pulse will remain undistorted, so the Q-factor will remain at high values. Nonetheless the effect of the nonlinearities can be shown by extracting the phase out of the field for different distances and comparing it against the theoretical function calculated for the phase. This is achieved by launching a Gaussian pulse into the system of power 1mW and $T_{fwhm} = 33$ ps. The parameters used for the theoretical plotting of the phase are an $n_2 = 2.6 \times 10^{-20} m^2/W$ and a wavelength parameter $\lambda = 1.55 \mu m$. These were used to calculate the slope of each of these curves through the nonlinear coefficient as expressed by the following formula,

$$\gamma = \frac{2\pi n_2}{\lambda A_{eff}} \tag{2.53}$$

substituting these into the scalar model,

$$\phi_{NL} \simeq 1.05 \times 10^{-3} z \tag{2.54}$$

and vector equations

$$\phi_{NL(x)} \simeq 9.5 \times 10^{-4} z \tag{2.55}$$

$$\phi_{NL(y)} \simeq 8.3 \times 10^{-4} z \tag{2.56}$$
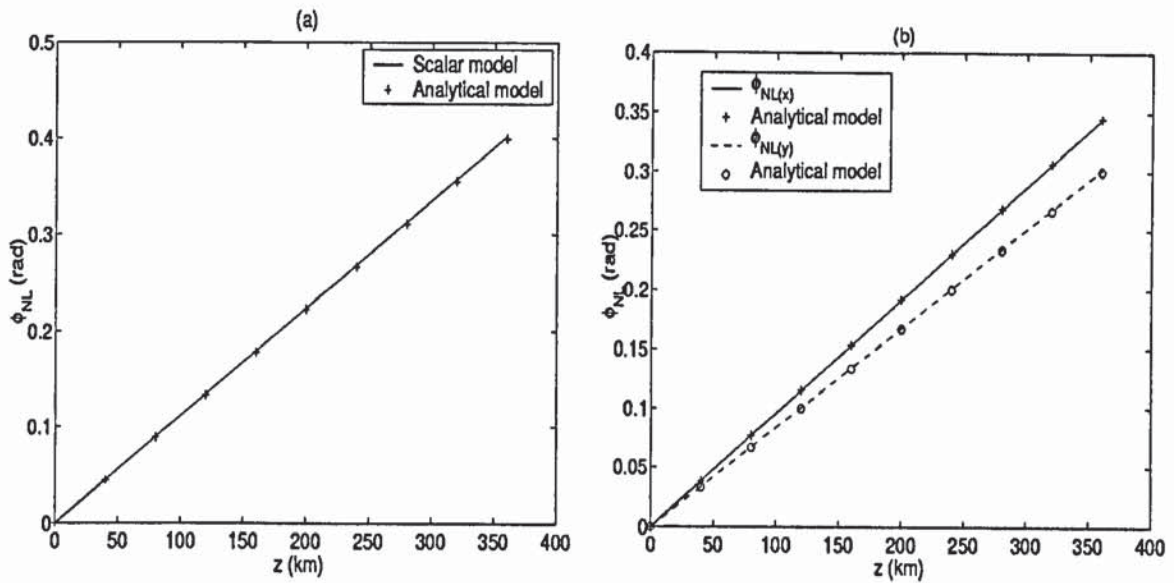
Figure 2.6: Nonlinear phase evolution with distance compared against the theoretical approximation for (a) the scalar, (b) the vector model.

Where a polarisation of 35° was used for the vector model and z is the distance parameter in (km) units. In figure 2.6 the linear relationship between nonlinear phase and distance is clearly seen for the simplest of all cases involving nonlinear effects, as well as an excellent agreement between numerical and theoretical results is demonstrated. Note the simulation for this limiting case, useful as it is for numerical purposes, is for an unphysical limit. When $\Delta\beta \to 0$, then the beat length goes to infinity which implies that the last term in 2.34,2.35 cannot be ignored. When b=0 then one will get back rotational symmetry.

Chapter 3

Polarisation mode dispersion theory

3.1 Introduction

Even single-mode fibres support two orthogonal modes of polarisation. The inherent stress and imperfections that exist within a fibre core, lead to birefringence. The two modes experience a different refractive index, which results in different propagation times for the two modes. In general the birefringence is combined with random mode coupling, occurring when power from the vertical mode couples to the horizontal and vice versa. The simplest case of applying PMD is by modelling the total transmission as a concatenation of many uniform birefringence segments randomly oriented.

3.2 Modal birefringence

In terms of mathematics the difference stems from the difference in the propagation constant of the two modes. From Eq.2.36,

$$\Delta\beta = \beta_{0x} - \beta_{0y} = \frac{\omega n_{0x}}{c} - \frac{\omega n_{0y}}{c} = \frac{2\pi}{\lambda}\Delta n. \tag{3.1}$$

or as defined in [48],

$$B_m = \frac{|\Delta\beta|}{k_0} = |\Delta n| \tag{3.2}$$

where λ is the wavelength of light, ω is the angular frequency, c is the speed of light,

40

$\Delta n = n_{0x} - n_{0y}$ is the refractive index difference, and $k_0 = 2\pi/\lambda$. The two components travel then at different speeds as their group velocities will be different and split as shown in figure 3.1,
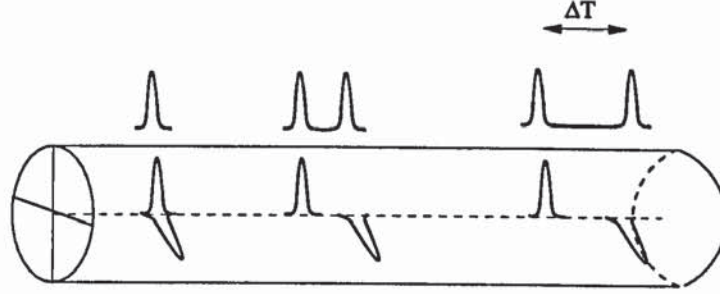
Figure 3.1: Pulse splitting due to birefringence.

Eventually this results in a pulse broadening given by [1],

$$\Delta T = \left| \frac{L}{\Delta u_g} \right| = k_0 L \frac{dB_m}{d\omega} + \frac{B_0}{c} \tag{3.3}$$

The parameter u_g represents the group-velocity and L is the total transmission length. This relation results for a uniform birefringent element only. In reality the birefringence combines with power coupling and then grows with the square root of the length. For what is more, in a uniform birefringent fibre, having a constant differential group delay (DGD) between the two orthogonal modes results in a periodic variation of the phase and thus in a periodic variation of the polarisation of the signal. The period over which the signal returns to the original polarisation is called the beat length L_B, so that

$$L_B = \frac{\lambda}{|\Delta n|} \tag{3.4}$$

Such a periodic evolution is shown in figure 3.2, and it represents the change of polarisation within a uniform birefringent segment or a polarisation maintaining fibre (PMF). In a real fibre the evolution of polarisation is random and depends on the characteristics of the signal and the characteristics of the fibre which vary in a random way. Moreover in any fibre for any wavelength there are two orthogonal polarisation states undistorted by birefringence and can be used as basis vectors for a description of PMD in all-fibres [49].
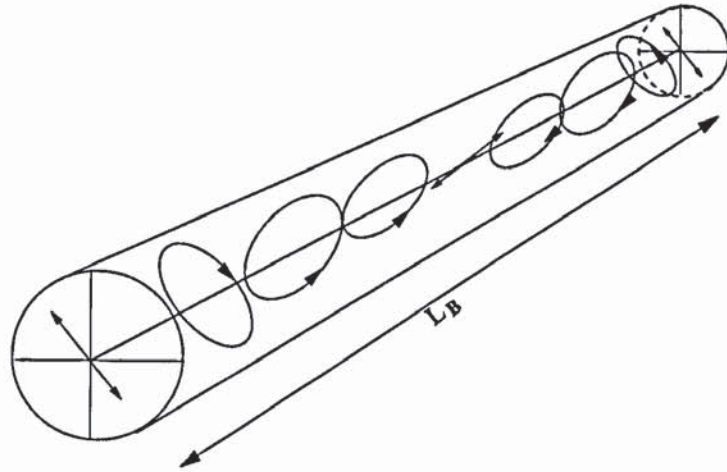
Figure 3.2: Evolution of polarisation in a uniform birefringent fibre.

3.3   Polarisation mode coupling

In general the splitting of the pulses due to birefringence combines with power coupling between the two modes which is random in nature. Thus instead of having an example such as that of figure 3.1, the resulting signal as shown in figure 3.3 will be the product of the following process. The two components of the pulse gain a delay between them so that the pulse splits into two pulses. Meeting the first local imperfection in the fibre, part of the power couples from one mode to the other. The coupled signal continues splitting linearly due to the DGD per length.
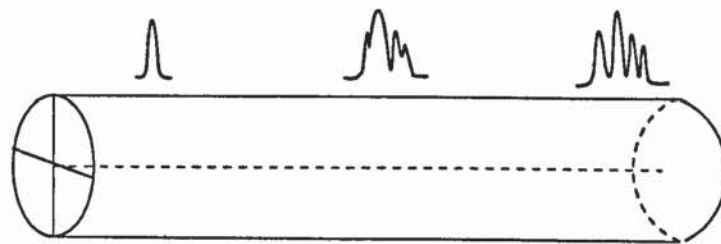
Figure 3.3: Evolution of a signal in a randomly birefringent fibre.

This continuous random distribution of mode-coupling, results in the splitting, broadening or merging of pulses, as the birefringence of one segment might counteract or reduce the effect of the previous elements. For that reason the DGD for a real fibre grows with the square-root of the fibre length. Additionally PMD will vary randomly with temperature and time which lead to the conclusion that the PMD of a system has

to be evaluated and analysed statistically.

3.4   Mathematical description of light

The launched signal can be decomposed into two lightwaves such that their electric-field directions are mutually perpendicular with different amplitudes and phases [50]. As described below,

$$\mathbf{E}_x = \hat{x} E_x \exp(i(\omega t - \beta z + \phi_x)) \tag{3.5}$$

$$\mathbf{E}_y = \hat{y} E_y \exp(i(\omega t - \beta z + \phi_y)) \tag{3.6}$$

we thus define a phase difference $\Delta\phi = \phi_x - \phi_y$, and β is the propagation constant. The electric field resulting can then be represented as,

$$\mathbf{E}(z,t) = \mathbf{E}_x(z,t) + \mathbf{E}_y(z,t) \tag{3.7}$$

It is common to express the two components in matrix formation. For that reason one might use the Jones vector or the Mueller matrix formalism. The Jones vector $\tilde{\mathbf{E}}$ for the electric field is written as,

$$\tilde{\mathbf{E}} = \begin{pmatrix} \mathbf{E}_x(t) \\ \mathbf{E}_y(t) \end{pmatrix} = \begin{pmatrix} E_x e^{i\phi_x} \\ E_y e^{i\phi_y} \end{pmatrix} \tag{3.8}$$

In normalised form one might divide by the modulus of the field that is $|E| = \sqrt{E_x^2 + E_y^2}$. In this case the Jones vector takes the form,

$$\tilde{\mathbf{E}} = \begin{pmatrix} \cos\theta e^{i\phi_x} \\ \sin\theta e^{i\phi_y} \end{pmatrix} \tag{3.9}$$

where $\cos\theta = E_x/\sqrt{E_x^2 + E_y^2}$, and $\sin\theta = E_y/\sqrt{E_x^2 + E_y^2}$. For example the horizontal and vertical states can be written* respectively as $e^{i\phi_x}(1,0)^T$ and $e^{i\phi_y}(0,1)^T$. To attain even simpler expressions for linear polarisations we can assume that $\Delta\phi =$

---

*The index T represents the matrix transpose

$\phi_x - \phi_y = 0$. With that simplification one might write in general that the Jones vector is given by $(1/\sqrt{2})(\cos\theta, \sin\theta)^T$ for example a 45^ϕ linear polarisation will be given as $(1/\sqrt{2})(1, 1)^T$. The left and right-circular polarised light has the following characteristics $E_x = E_y$ and $\Delta\phi = \pm\pi/2$ which leads to the Jones vector $(1/\sqrt{2})(1, e^{\pm i\pi/2})^T$.

According to this notation the optical medium will be represented by a 2×2 transfer matrix. Let then $\mathbf{A}$ be the transfer matrix $\tilde{E}_{in}$ being the input vector and $\tilde{E}_{out}$ the output vector, then that results in,

$$\tilde{E}_{out} = \begin{pmatrix} a_{11} & a_{12} \\ a_{21} & a_{22} \end{pmatrix} \tilde{E}_{in} = \mathbf{A}\tilde{E}_{in} \tag{3.10}$$

which implies that in the end of an optical fibre composing out of a number n of such elements the result is,

$$\tilde{E}_{out} = \mathbf{A_n}...\mathbf{A_2}\mathbf{A_1}\tilde{E}_{in} \tag{3.11}$$

An alternative method for describing the polarisation of light is the Mueller matrices formalism. The Mueller matrices method was devised in 1943 by Hans Mueller and it is a matrix method that describes polarisation adequately through the Stokes parameters [51, 52, 53, 54]. The Stokes parameters originate in the work of 1852 by G.G. Stokes [55]. According to this theory one is able to identify the polarisation of light using four filters. An isotropic filter transmitting light, with equal intensity for all the polarisation states, a second linear polariser passing the horizontal linear polarised light with maximum intensity, a $+45^\phi$ polariser, and a circular polariser transmitting with maximum intensity for the circular polarisations and being non-transparent to linear polarisations. The normalised Stokes vectors are given by [56],

$$s_0 = \frac{|E_x|^2 + |E_y|^2}{|E|^2} = 1 \tag{3.12a}$$

$$s_1 = \frac{|E_x|^2 - |E_y|^2}{|E|^2} = \cos 2\theta \tag{3.12b}$$

$$s_2 = \frac{2Re(E_x E_y^*)}{|E|^2} = \sin 2\theta \cos\phi \tag{3.12c}$$

$$s_3 = \frac{2Im(E_x E_y^*)}{|E|^2} = \sin 2\theta \sin \phi \qquad (3.12d)$$

The Stokes parameters represent coordinates on the Poincaré sphere, while s_0 represents the intensity of light. It is important to mention that orthogonal polarisation states such as horizontal and vertical linear polarisation are represented by antiparallel vectors on the Poincaré sphere.
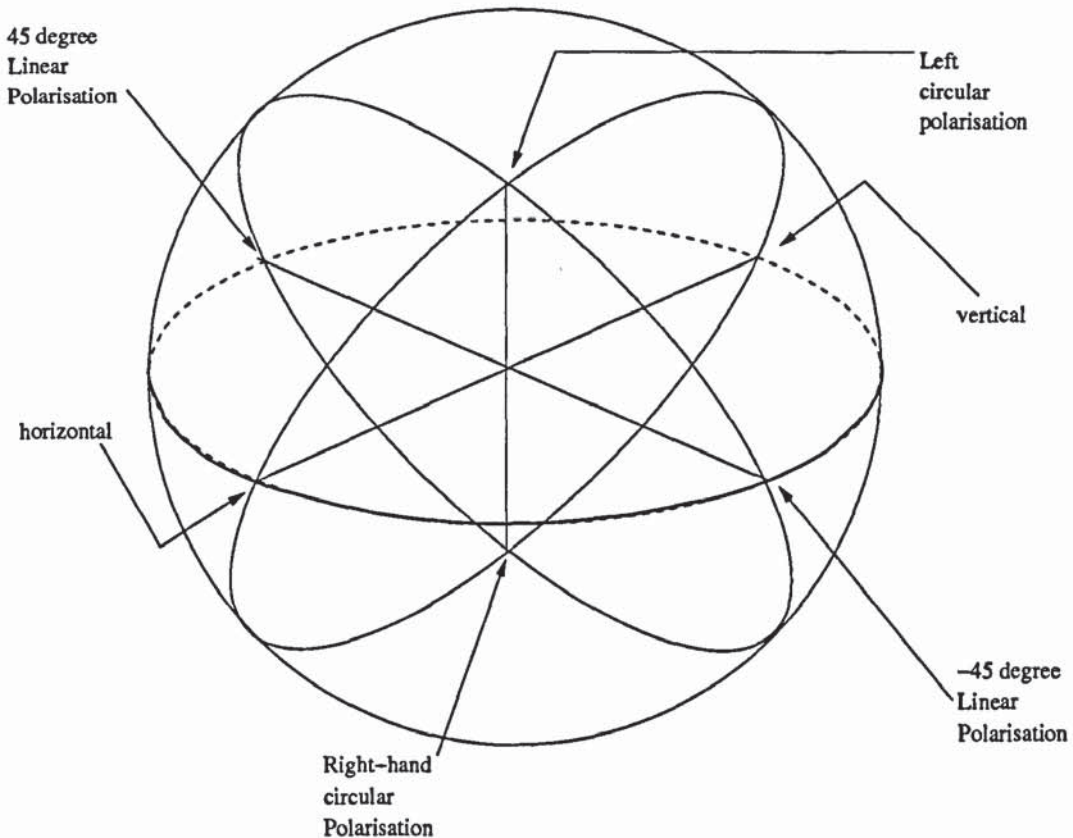
Figure 3.4: Poincaré sphere representation of the Stokes vectors

The angles θ and ϕ that are determined by the position of the Stokes vector are indicated in figure 3.5. The Mueller matrices will represent the optical element in a similar way to that of the Jones transfer matrices and will allow for an output vector s_{out} on the Poincaré to be mapped to an input vector s_{in}. So one writes,

$$s_{out} = M s_{in} \tag{3.13}$$

Where M is the transfer matrix of an optical element.
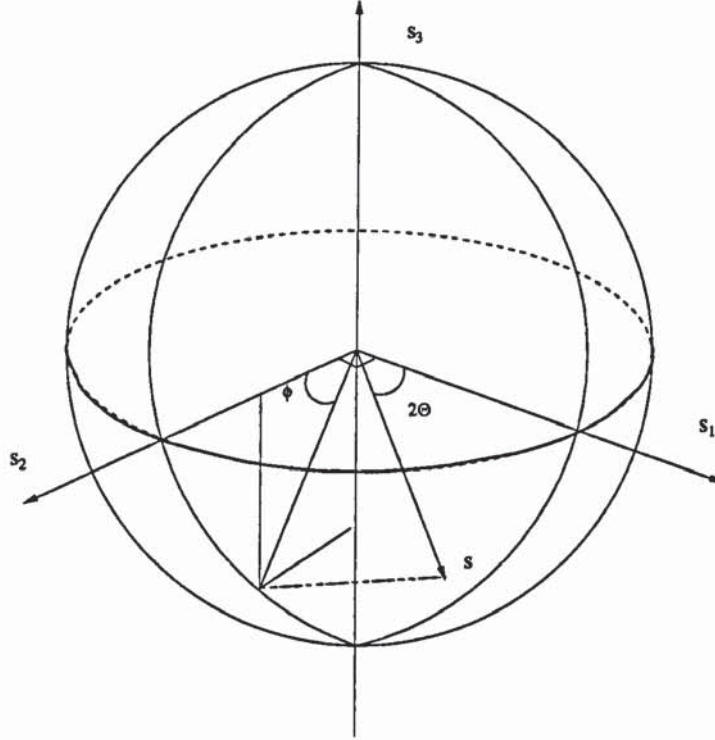
Figure 3.5: A polarisation state represented on the Poincaré sphere by the Stokes vectors.

3.5 The PMD vector

3.5.1 PMD vector and Poincaré sphere representation

In this section we will explain what the PMD vector is. The Stokes vector in a given length of a fibre segment with negligible PDL, rotates as a consequence of the frequency dependence of the transfer matrix $R(l, \omega)$ of the segment, where l indicates length. As a result,

$$s(l, \omega) = R(l, \omega) s(0, \omega) \tag{3.14}$$

the parameter $s(0, \omega)$ is the initial Stokes vector, taking the derivative of that and with no frequency dependence of the input state, one writes,

$$\frac{ds(l, \omega)}{d\omega} = \frac{dR(l, \omega)}{d\omega} s(0, \omega) \tag{3.15}$$

next Eq. 3.14 is multiplied by $R^{-1}(l, \omega)$ and produces $s(0, \omega) = R^{-1}(l, \omega)s(l, \omega)$, which is further substituted in Eq. 3.15. Thus,

$$\frac{ds(l, \omega)}{d\omega} = \frac{dR(l, \omega)}{d\omega} R^{-1}(l, \omega)s(l, \omega) = \Omega(l, \omega) \times s(l, \omega) \tag{3.16}$$

where the $s(l, \omega)$ is in the usual fashion the stokes vector representing a polarisation on the Poincaré sphere. The parameter $\Omega(l, \omega)$ is the PMD vector and $\Omega(l, \omega) \times = \frac{dR(l,\omega)}{d\omega}R^{-1}(l, \omega)$. The modulus of the PMD vector is the DGD of the link $\Delta T = |\Omega|$. The Stokes vector in Eq. 3.16 is defined as a changing quantity with carrier frequency. It should be stressed that this is in effect qualitatively the same effect as the change of the polarisation state of a pulse with distance as it travels through the fibre. The relation for the local birefringence $W(l, \omega)$ in a fixed frequency and tracing the spatial evolution is defined then as,

$$\frac{ds(l, \omega)}{dz} = W(l, \omega) \times s(l, \omega) \tag{3.17}$$

Thus the birefringence of a PMD vector will result in a closed trajectory such as in figure 3.6. This has been explained earlier and is justified if one considers the periodic evolution that the signal will undergo under a constant DGD. Such a relation describes only the first-order PMD. For practical applications in real-time systems where the magnitude and the direction of PMD changes, the definition of PMD changes to accommodate all of these effects, by expanding the PMD around a centre frequency and it takes the form,

$$\Omega(l, \omega) = \Omega(l, \omega_0) + \frac{\partial\Omega(l, \omega)}{\partial\omega}(\omega - \omega_0) + \frac{\partial^2\Omega(l, \omega)}{\partial\omega^2}\frac{(\omega - \omega_0)^2}{2} + ... \tag{3.18}$$

where l is the length of each individual fibre in the fibre ensemble, ω is the frequency parameter and ω_0 is the centre frequency. Such a random evolution of the stokes vector
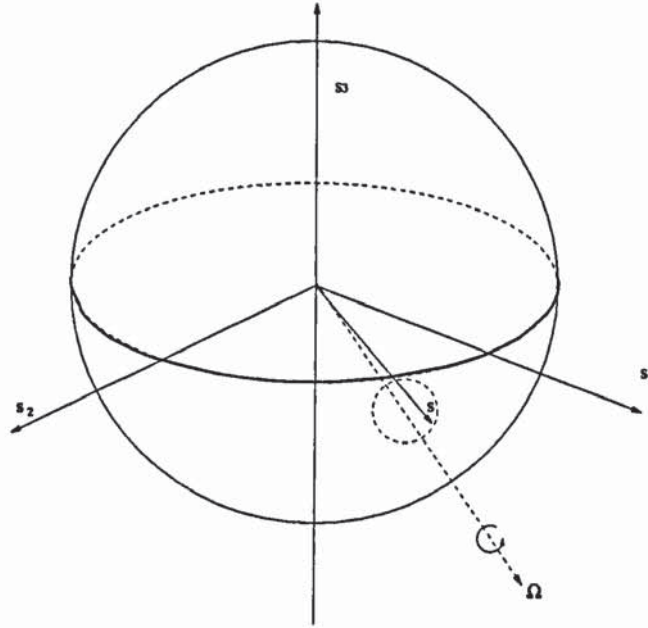
Figure 3.6: Effect of the PMD of a uniform segment on a Stokes vector

is presented in figure 3.7

3.5.2 Pulse spreading due to PMD

The theoretical evidence presented into paragraph 3.5.1 are enough to provide an expression, for the spreading caused by PMD. The final relation is of great significance to the work produced in this thesis so in the simplest of terms we follow the derivation of [57]. Taking the derivative of equation 3.16 with respect to distance and the derivative of 3.17 with respect to frequency, this implies that,

$$
\begin{aligned}
\frac{d(W \times s)}{d\omega} &= \frac{d(\Omega \times s)}{dz} \\
\frac{dW}{d\omega} \times s + W \times (\Omega \times s) &= \frac{d\Omega}{dz} \times s + \Omega \times (W \times s) \\
\frac{d\Omega}{dz} &= \frac{dW}{d\omega} + W \times \Omega
\end{aligned}
\tag{3.19}
$$

where at first the Jacobi identity was used so that $(W \times \Omega) \times s = W \times (\Omega \times s) - \Omega \times (W \times s)$ and the resulting expression was multiplied by $(\times s)^{-1}$. Assuming that the local birefringence results as a perturbation added stepwise upon a constant
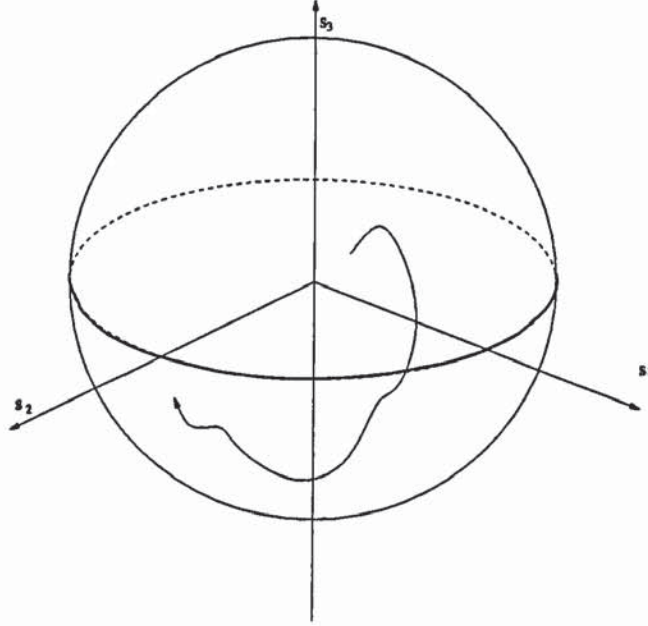
Figure 3.7: Effect of the PMD of a transmission fibre on a Stokes vector

background one writes, for the local birefringence vector,

$$W(l,\omega) = W_0(l,\omega) + \Delta W \tag{3.20}$$

with $W_0 = (\Delta\beta, 0, 0)^T$ and $\Delta W = (\Delta W_1, \Delta W_2, \Delta W_3)^T$ where $\Delta\beta = \beta_{0x} - \beta_{0y}$ represents the birefringence parameter and $\Omega(l,\omega) = (\Omega_1(l,\omega), \Omega_2(l,\omega), \Omega_3(l,\omega))^T$. Substituting these into Eq. 3.19 this leads to,

$$\frac{d\Omega}{dl} = - \begin{pmatrix} 0 & -\Omega_3(l,\omega) & \Omega_2(l,\omega) \\ \Omega_3(l,\omega) & 0 & -\Omega_1(l,\omega) \\ -\Omega_2(l,\omega) & \Omega_1(l,\omega) & 0 \end{pmatrix} \Delta W - \begin{pmatrix} 0 & 0 & 0 \\ 0 & 0 & -\Delta\beta \\ 0 & \Delta\beta & 0 \end{pmatrix} \Omega$$
$$+ \begin{pmatrix} \Delta\beta' \\ 0 \\ 0 \end{pmatrix} \tag{3.21}$$

At this point it should be noted that $\Delta W'$ is negligible. Finally selecting ΔW from a random distribution of white Gaussian noise with a standard deviation of σ then

ΔW will be substituted by $\sigma \Delta W$, thus

$$\frac{d\Omega}{dl} = -\sigma \begin{pmatrix} 0 & -\Omega_3(l,\omega) & \Omega_2(l,\omega) \\ \Omega_3(l,\omega) & 0 & -\Omega_1(l,\omega) \\ -\Omega_2(l,\omega) & \Omega_1(l,\omega) & 0 \end{pmatrix} \Delta W - \begin{pmatrix} 0 & 0 & 0 \\ 0 & 0 & -\Delta\beta \\ 0 & \Delta\beta & 0 \end{pmatrix} \Omega$$
$$+ \begin{pmatrix} \Delta\beta' \\ 0 \\ 0 \end{pmatrix} \tag{3.22}$$

As the quantity $\sigma \Delta W$ is randomly varying then Eq. 3.22 is classified as a stochastic differential equation. According to the theory of these equations any function F of the vector $\Omega(l,\omega)$, such as the DGD of a fibre $\Delta T^2 = \Omega_1^2 + \Omega_2^2 + \Omega_3^2$, obeys the law.

$$\frac{d < F(\Omega(l,\omega)) >}{dl} = < G(F(\Omega(l,\omega))) > \tag{3.23}$$

The operator G in Eq. 3.23 is defined as the generator of the vector $\Omega(l,\omega)$ The stochastic system of Eq. 3.22 is interpreted either by the Ito or the Stratonovich calculus. Both of these interpretations are equally correct and one can be transformed into the other by a translation algorithm, which for Eq. 3.22 implies that a term equal to $\sigma^2\Omega$ is subtracted from the right-hand side. The method to use is chosen according to the problem at hand. Suffice to say that concerning Eq. 3.22 the authors in [57] proved that without the aforementioned term of $\sigma^2\Omega$ and if one derives the equation for the modulus average $< |\Omega(l)|^2 >$ according to 3.21 with the help of the appropriate generator, without the driving term this moves off the sphere that it starts. This is not correct as this average should be invariant as it is given by an equation which intends to describe a process which is homogeneous with respect to length and with respect to the vector $\Omega(l,\omega)$. While adding the term, this produces the wanted result that is $< |\Omega(l)|^2 >= |\Omega(0)|^2$. After the subtraction of this term 3.22 results in,

$$\frac{d\Omega}{dz} = -\sigma \begin{pmatrix} 0 & -\Omega_3(l,\omega) & \Omega_2(l,\omega) \\ \Omega_3(l,\omega) & 0 & -\Omega_1(l,\omega) \\ -\Omega_2(l,\omega) & \Omega_1(l,\omega) & 0 \end{pmatrix} \Delta W - \begin{pmatrix} \sigma^2 & 0 & 0 \\ 0 & \sigma^2 & -\Delta\beta \\ 0 & \Delta\beta & \sigma^2 \end{pmatrix} \Omega$$
$$+ \begin{pmatrix} \Delta\beta' \\ 0 \\ 0 \end{pmatrix} \tag{3.24}$$

the key equation to producing the appropriate generator for the equation is given in Appendix B. The generator G is thus given as,

$$G = \frac{\sigma^2}{2} \Big[(\Omega_2^2 + \Omega_3^2)\frac{d^2}{d\Omega_1^2} + (\Omega_1^2 + \Omega_3^2)\frac{d^2}{d\Omega_2^2} + (\Omega_1^2 + \Omega_2^2)\frac{d^2}{d\Omega_3^2}$$
$$- 2\Omega_1\Omega_2\frac{d^2}{d\Omega_1\Omega_2} - 2\Omega_1\Omega_3\frac{d^2}{d\Omega_1\Omega_3} - 2\Omega_2\Omega_3\frac{d^2}{d\Omega_2\Omega_3} \Big]$$
$$- \sigma^2 \Big(\Omega_1\frac{d}{d\Omega_1} + \Omega_2\frac{d}{d\Omega_2} + \Omega_3\frac{d}{d\Omega_3} \Big) + \Delta\beta \Big(\Omega_3\frac{d}{d\Omega_2} - \Omega_2\frac{d}{d\Omega_3} \Big) + \Delta\beta'\frac{d}{d\Omega_1} \tag{3.25}$$

substituting $< \Delta T^2 > = < \Omega_1^2 + \Omega_2^2 + \Omega_3^2 >$ into Eq. 3.23 gives,

$$\frac{d < \Delta T^2 >}{dl} = 2\Delta\beta' < \Omega_1 > \tag{3.26}$$

one notes that only $< \Omega_1 >$ remains to be resolved in Eq. 3.26 in order to obtain a final equation that gives the evolution of $< \Delta T^2 >$ with distance. So plugging Ω_1 into Eq. 3.23

$$\frac{d\Omega_1}{dl} = -\sigma^2 < \Omega_1 > +\Delta\beta' \tag{3.27}$$

Equations 3.26, 3.27 are first order differential equations, solving first Eq. 3.27 and then substituting into Eq. 3.26 (Appendix B), results into the final relation,

$$< \Delta T^2 >= \sigma_T^2 = 2\Big(\frac{\Delta\beta'}{\sigma^2}\Big)^2 (\sigma^2 l + \exp(-\sigma^2 l) - 1) \tag{3.28}$$

from this equation it is possible to generalise and by choosing to set $\sigma = 1$, we obtain the two limits of l, being in the short or in the long length regime. As a rule [1] if $l < l_c$ this is classified as a short length while the opposite falls in the long distance regime. In the first case $(l < l_c)$ the exponential term in 3.28 is retained, so that if this is expanded up to the second order as, $e^x = \sum_{n=0}^{\infty} x^n/n!$ then,

$$< \Delta T^2 >= \sigma_T^2 \approx \Delta\beta'^2 l^2 \tag{3.29}$$

in the long length regime the exponential term becomes negligible and the term linearly proportional to the distance provides the main contribution so that one writes,

$$< \Delta T^2 >= \sigma_T^2 \approx \Delta\beta'^2 2l \tag{3.30}$$

these equations provide a clear understanding about the behaviour of a system influenced by PMD. In a short distance the spreading, which results by taking the square root of Eq. 3.29, evolves linearly while in the long length regime, where it is obtained by the square root of Eq. 3.30, it evolves with the square root of the distance. This is directly related with the physical phenomenon of power coupling which for a longer distance is adding up more, reducing the effect of the DGD per length.

3.6   Statistical properties of the PMD vector

Based on the formalism of the Mueller matrices a long fibre will be given as the product of a number of these matrices, thus [58],

$$M^n = M_n M_{n-1} .... M_2 M_1 = M_n M^{n-1} \tag{3.31}$$

the cross-product of the PMD vector which is written as $\Omega\times$, results then according to the Mueller matrices notation, $\Omega\times = \frac{dM^n}{d\omega}\frac{1}{M^n}$ this is in agreement with the expression given earlier that is $\Omega(l,\omega)\times = \frac{dR(l,\omega)}{d\omega}R^{-1}(l,\omega)$ for a rotation matrix R. A final expression for $\Omega\times$ in terms of the three components $(\Omega_1, \Omega_2, \Omega_3)^T$ can be obtained from a relation such as Eq. 3.16.

$$\Omega\times = \begin{pmatrix} 0 & -\Omega_3 & \Omega_2 \\ \Omega_3 & 0 & -\Omega_1 \\ -\Omega_2 & \Omega_1 & 0 \end{pmatrix} \tag{3.32}$$

Using these tools it is proven that according to the definition provided in [58] the PMD-vector resulting from this process is the vector sum of the vectors for each optical element transformed by the appropriate Mueller matrices to the same position. This is expressed in Eq. 3.33.

$$\Omega^n = \Omega_n + M_n\Omega^{n-1} \tag{3.33}$$

This contributes to the statement that this section intends to make, identifying the probability distribution function of the PMD. According to Eq. 3.33 the direction of the three components of the PMD vector will be varying as well as the modulus of each one of them, that is after each step the PMD vector is multiplied by a random transfer matrix. This is defined as a three dimensional random walk [57]. The PMD vector will eventually, after a long length of fibre, be given by the sum of the individual PMD vectors, which will obey the central limit theorem, which implies that its distribution will be a Gaussian. This will lead finally into the analytical model of the distribution of the PMD vector being a Maxwellian as this given as the average of the squares of the three Gaussian components and this from theory is a Maxwellian given by Eq. 3.34

$$PDF(t)_{analytical} = \frac{8}{\pi^2\Delta\tau}\left(\frac{2t}{\Delta\tau}\right)^2 \exp\left(-\frac{1}{\pi}\left(\frac{2t}{\Delta\tau}\right)^2\right) \tag{3.34}$$

the theoretical form of this distribution is presented in figure 3.8

Moreover the background autocorrelation function (ACF) of the PMD should tend rapidly toward zero. This is a direct outcome of the fact that the PMD vector for each
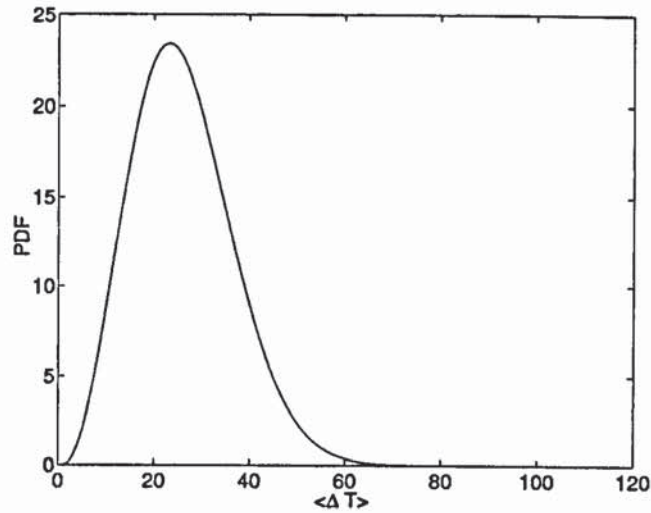
Figure 3.8: Probability density function for the distribution of ΔT

one of the individual frequencies, should be independent and should thus be correlated only with itself. This is effectively given by a quadratic decay of the background (ACF) according to,

$$ACF(\omega)_{analytical} = \frac{3}{\Delta \tau^2 (\omega - \omega_0)^2} \left[1 - \exp\left(\frac{-\Delta \tau^2 (\omega - \omega_0)^2}{3}\right) \right] \qquad (3.35)$$

This is graphically represented as in Fig. 3.9 for a $< \Delta T >= 25$ ps,
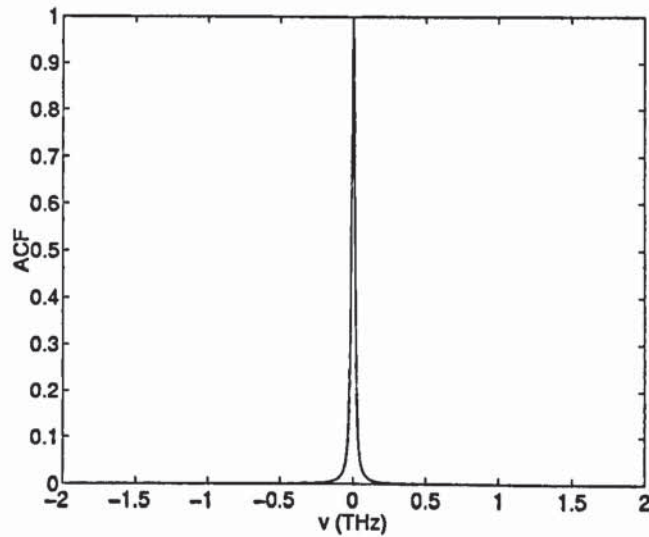
Figure 3.9: Autocorrelation function of ΔT

To give a few examples for the DGD of existing systems, the values quoted in liter-

ature for old installed fibres, generally will vary between 0.1 ~ 3 ps while for PMD in recent installations these have been reduced to approximately 0.01 ~ 0.1 ps. Based on the present day fibre models then, one assumes that the PMD phenomenon presents no significant problem. This assumption is not true as there are already many fibres installed, that are based on old-specifications and re-installment of new fibre would prove more costly in comparison to troubleshooting the problem of PMD through statistical analysis. Further by increasing the data-rates, naturally the spreading caused by PMD occupies a bigger part of the bit-slot, and thus even with the newly installed fibres the problem might resurface for certain systems.

Chapter 4

Analysis and implementation of existing methods for simulating PMD

4.1 Introduction

The coarse-step method, which is the principal method, for numerically implementing the phenomenon of PMD, will be introduced in this chapter. The theory as well as the advantages and disadvantages of this method will be analysed through theoretical evidence. The outcomes resulting from the numerical implementation of this method will be presented, in the course of this chapter investigating the evolution of the state of polarisation of the signal (SOP), in terms of the mixing on the Poincaré sphere. And the effect that the coarse-step method has on the spreading of a signal.

4.2 Coarse-step method

The common approach of simulating PMD numerically is the coarse-step method. This is based on the theory of emulating the optical fibre medium as a concatenation of fibre sections with random rotations of the birefringence-axes in between, which in turn results in mode coupling. This procedure is effectively represented by figure 4.1,

56
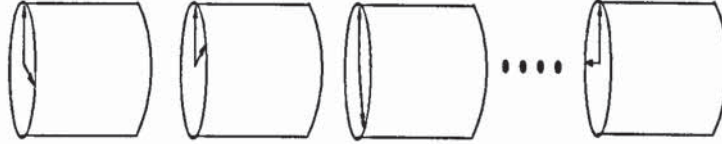
Figure 4.1: Concatenation of waveplates with a fixed DGD and random rotation in
between the segments.

Furthermore it is convenient to describe this emulation process with the help of the
CNLS equation. From equations 2.34, 2.35, assuming that all of the other effects can
be neglected apart from PMD, these equations can be written as,

$$i\left(\frac{\partial E_x}{\partial z} + \beta'_x \frac{\partial E_x}{\partial t}\right) = 0 \tag{4.1}$$

$$i\left(\frac{\partial E_y}{\partial z} + \beta'_y \frac{\partial E_y}{\partial t}\right) = 0 \tag{4.2}$$

Next Fourier transforming these relations and assuming that $\beta'_x = b'$, $\beta'_y = -b'$ we
obtain,

$$i\frac{\partial \tilde{E}_x}{\partial z} + b'\omega \tilde{E}_x = 0 \tag{4.3}$$

$$i\frac{\partial \tilde{E}_y}{\partial z} - b'\omega \tilde{E}_y = 0 \tag{4.4}$$

This represents the splitting of the two modes as the wave envelope for the vertical
direction will travel at a group velocity $v_{gx} = 1/\beta'_x = 1/b'$ while the wave envelope of the
horizontal polarisation will be retarded having a group velocity of $v_{gy} = 1/\beta'_y = -1/b'$.
Effectively this implies that the direction of the x-axis component is the fast mode
while the y-axis is the slow mode. In this case and in the absence of any other effects
and mode coupling the two pulses will be separated in a given distance by $2b'L$ where
L is the propagation distance. The second step is to include the random rotation of
the field which is accomplished by multiplying with the following rotation matrix,

$$S = \begin{pmatrix} \cos\alpha & \sin\alpha exp(i\phi) \\ -\sin\alpha exp(i\phi) & \cos\alpha \end{pmatrix} \tag{4.5}$$

This matrix physically represents the exchange of energy between the two modes, since in a given distance the axes of birefringence will change direction. The angles α and ϕ are chosen at each step of the simulation from random uniform distributions within the range $[-\pi, \pi]$ and $[-\pi/2, \pi/2]$. Further these angles refer to random rotations of angles 2α, ϕ of the Stokes vector on the Poincaré sphere. Recalling that $< s_1^2 + s_2^2 + s_3^2 >= 1$ the distribution of a state of polarisation is considered uniformly distributed on the Poincaré sphere when $< s_i^2 > \rightarrow 1/3 \approx 0.3333$ where i = 1,2,3. Using the rotation matrix of Eq. 4.5, when the signal is unaffected by Eq. 4.1,4.2 the fibre will be represented by a series of rotation matrices of the form of the Eq. 4.5 multiplied together.

This is numerically implemented in our simulations. Using a CW initially polarised in $30°$, which is represented by a resolution of 2^{10} in a time window of 512 ps and calculating the SOP through 5000 runs the uniform mixing of the state of polarisation due to the rotation matrices only, is tested by setting the differential group delay per length $b' = 0ps/km$ in our equations. This is presented in figure 4.2 for a number N = 1,2,10,100 number of steps in our simulations with a step size of $\Delta z = 0.84$ km. The spots represent states of polarisation and the dim spots are located on the opposite side of the sphere. The variance for each one of the stokes vectors for each case is numerically calculated. For N = 1 $< s_1^2 > \approx 0.37$, $< s_2^2 > \approx 0.21$, $< s_3^2 > \approx 0.42$, N = 2 $< s_1^2 > \approx 0.3456$, $< s_2^2 > \approx 0.327$, $< s_3^2 > \approx 0.326$ for N = 10 $< s_1^2 > \approx 0.3346$, $< s_2^2 > \approx 0.33$, $< s_3^2 > \approx 0.328$ and for N = 100 $< s_1^2 > \approx 0.333$, $< s_2^2 > \approx 0.333$, $< s_3^2 > \approx 0.333$. From this data it is clear that the mixing for this case is quite rapid, even with two steps the distribution approximates closely the value of 1/3 for each of the three axes.

By contrast if one uses a rotation matrix that has the form of 4.6 and starting from a linear polarisation, then all the polarisation states will be concentrated on the equator as there is no phase difference between the pulses and the only effect of Eq. 4.6 will be the change of amplitude of the two modes and thus only linear polarisation states will exist as shown in figure 4.3 since there is no phase difference accumulated between the two modes.

$$S = \begin{pmatrix} \cos\alpha & \sin\alpha \\ -\sin\alpha & \cos\alpha \end{pmatrix} \quad (4.6)$$

Neglecting the effect of the rotation matrix and including only the first-order PMD that is the splitting of the two modes and using a polarisation of $30°$ and a $b' = 0.025$ ps/km the effect of the evolution of the SOP is shown in figure 4.4,
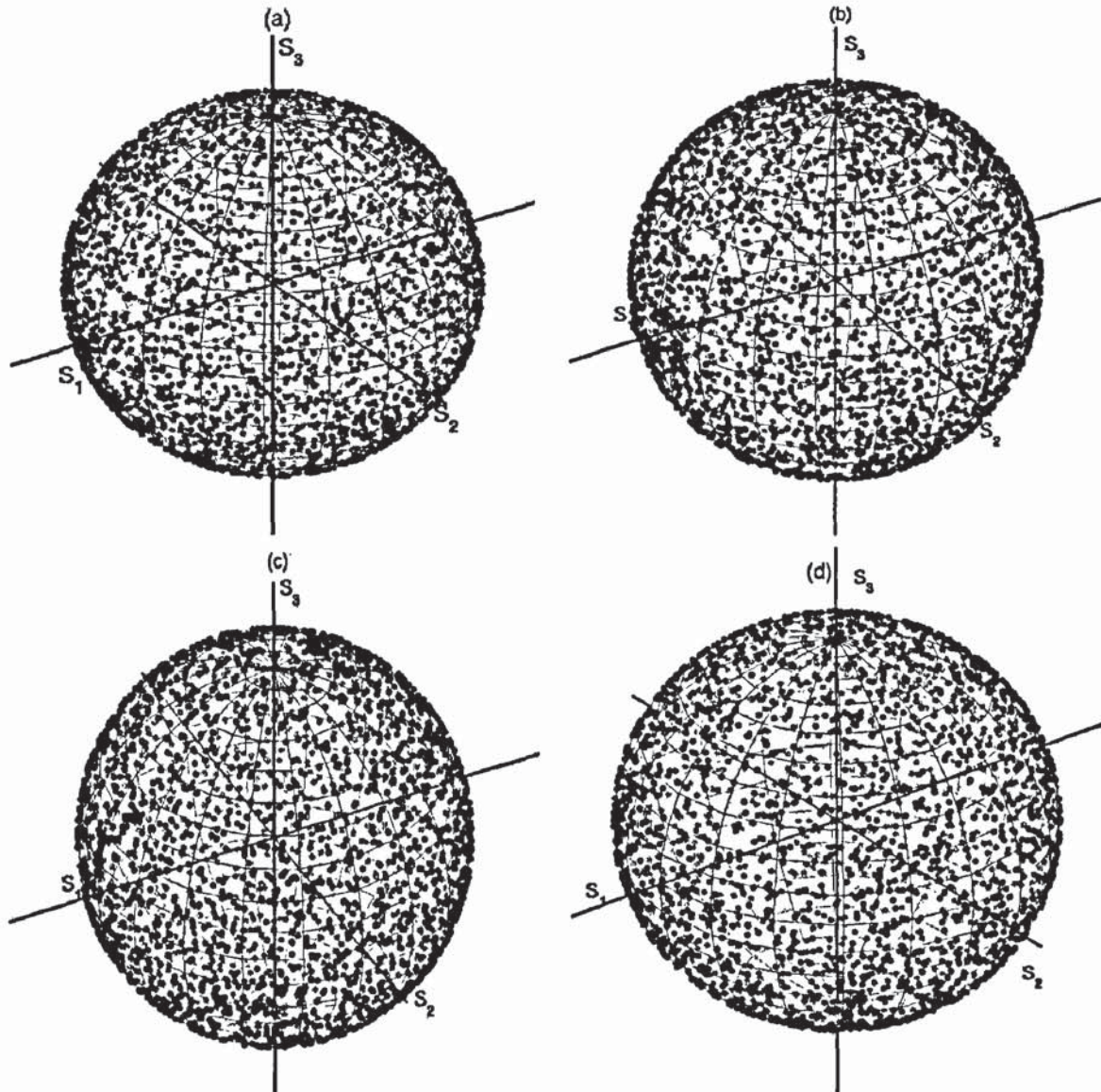
Figure 4.2: Distribution of the state of polarisation on the Poincaré sphere for Eq. 4.5 after (a) $N = 1$ step,(b) $N = 2$ steps ,(c) $N = 10$ steps (d) $N = 100$ steps

In figure 4.4 the SOP forms a closed trajectory around the PMD vector as the two
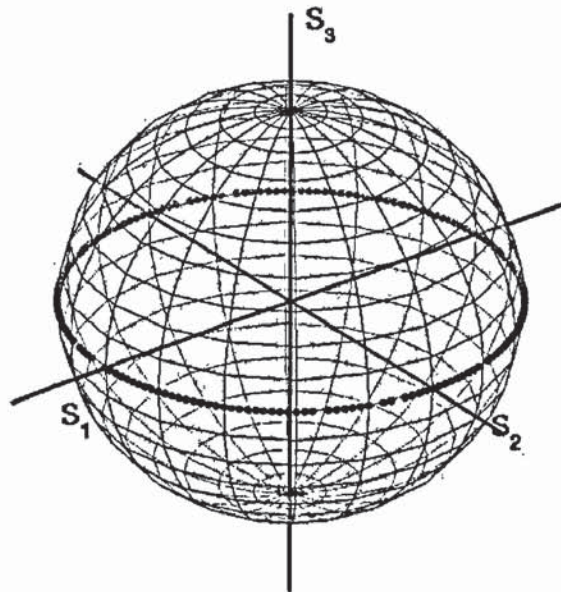
Figure 4.3: Distribution of the state of polarisation on the Poincaré sphere for a rotation matrix such as in Eq. 4.6
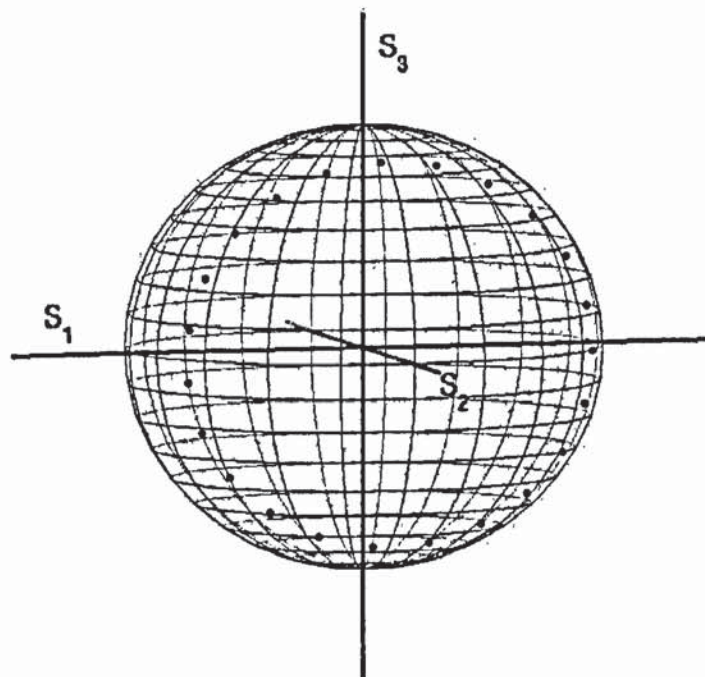
Figure 4.4: The first-order PMD effect on the distribution of a state of polarisation on the Poincaré sphere

modes drift apart with a constant rate, this as mentioned earlier is the effect for a short
piece of fibre or for a polarisation maintaining fibre. Moreover the mixing resulting
from the complete coarse-step method with the first-order PMD given by Eqs.4.1, 4.2
and the power coupling given by Eq. 4.5 is examined in figure 4.5. The step size used
is 0.8 km, and the characteristics of the simulation, $b' = 0.025$ ps/km with the signal
being represented by 2^{10} points in a time window of 512 ps. Using a single step for the
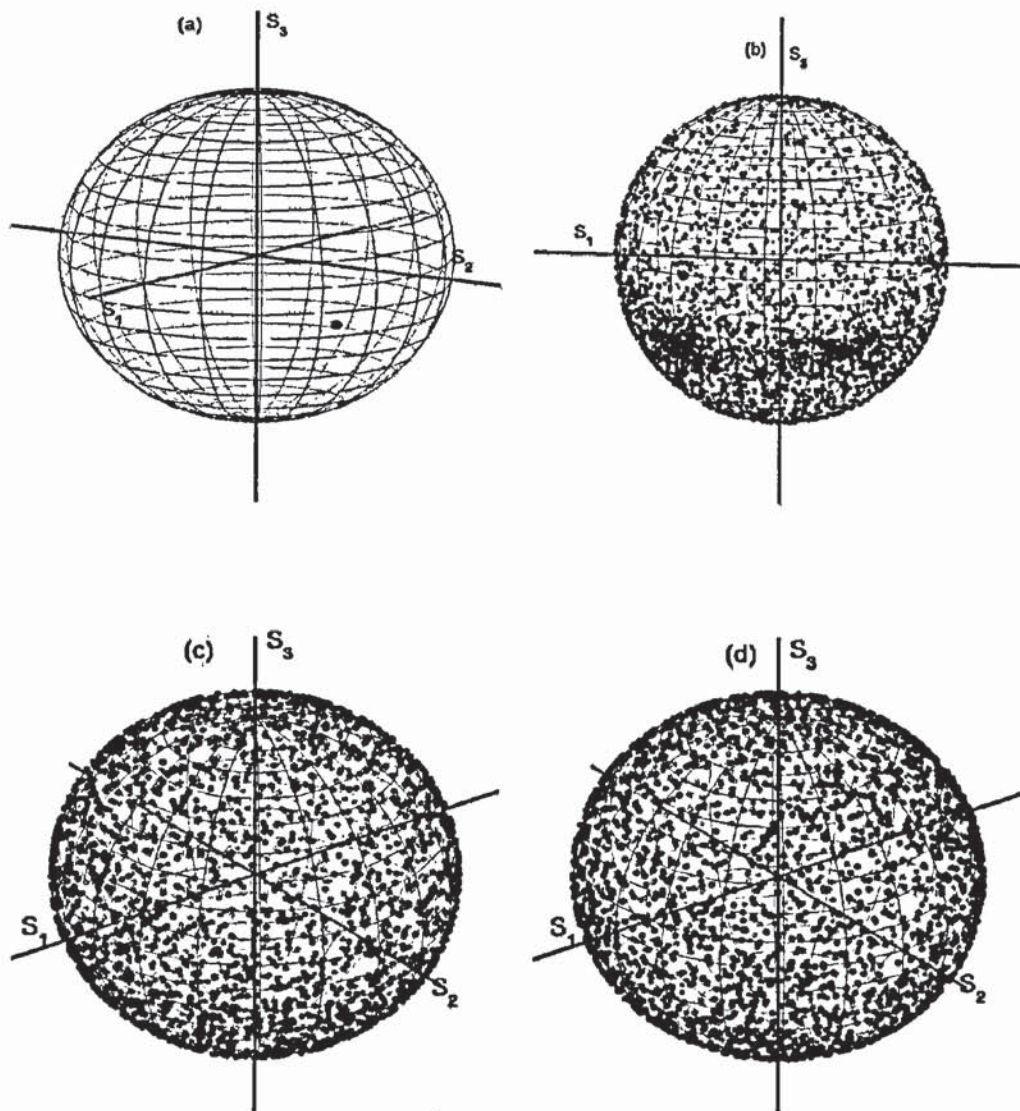
Figure 4.5: Distribution of the state of polarisation on the Poincaré sphere for the
coarse-step method after (a) N = 1 step,(b) N = 2 steps ,(c) N = 10 steps (d) N = 100
steps

coarse-step method, this in effect only includes the splitting of the two modes,and thus
the result is shown in figure 4.5(a) where only one SOP appears on the Poincaré sphere.

After the second step there is a large concentration of the states of polarisation in two areas of the sphere as presented in figure 4.5(b). This results after the two modes split, they rotate with respect to the birefringence axes and then the first order PMD follows once more. But this time can be directed on either side and thus the two modes will repel or attract each other.

Moreover this reflects on the variance for each of the three Stokes vectors, where for $N = 2 < s_1^2 > \approx 0.482, < s_2^2 > \approx 0.311, < s_3^2 > \approx 0.214$. In addition estimating the mixing after $N = 4$ steps this results in $< s_1^2 > \approx 0.465, < s_2^2 > \approx 0.283, < s_3^2 > \approx 0.253$, after $N = 8$ steps $< s_1^2 > \approx 0.455, < s_2^2 > \approx 0.295, < s_3^2 > \approx 0.255$, after $N = 10$ steps $< s_1^2 > \approx 0.335, < s_2^2 > \approx 0.334, < s_3^2 > \approx 0.328$ and after $N = 100$ steps, $< s_1^2 > \approx 0.333, < s_2^2 > \approx 0.333, < s_3^2 > \approx 0.333$.The $N = 10,100$, steps are shown in figures (c),(d) where the SOPs are uniformly distributed.

As a conclusion it is evident from our simulations that at least $8 \sim 12$ steps of the coarse-step method are needed for a proper mixing of the polarisation states as at this distance the Stokes vectors will be approximating uniformly distributed variables.

4.3 Rescaling of the polarisation mode dispersion

One of the main problems that the coarse-step method produces is the fact that this method artificially rescales the DGD resulting from a long-line of transmission. This implies that by numerically implementing systems in the long-distance regime, the DGD for the resulting signal will not follow accurately the description of Eq. 3.30 but will rather be rescaled according to the step size.

This is further shown analytically according to the notation of [61] as follows, defining the matrix for the field as,

$$E(z,t) = \begin{pmatrix} E_x(z,t) \\ E_y(z,t) \end{pmatrix} \tag{4.7}$$

and $\tilde{E}(z,\omega)$ the Fourier transform of that then after a long chain for the delay and rotation matrices,this yields,

$$\tilde{E}(z,\omega) = \prod_{n=1}^{N}(S_nS_\omega)\tilde{E}(0,\omega) \qquad (4.8)$$

where S_n are the different rotation matrices included after each DGD delay line and
S_ω are the delay matrices introducing the splitting of the two modes with Δz being
the step size,

$$S = \begin{pmatrix} \exp(ib'\omega\Delta z) & 0 \\ 0 & \exp(-ib'\omega\Delta z) \end{pmatrix} \qquad (4.9)$$

We then take the derivative of 4.8 with respect to ω. We note that $E'(0,\omega = 0) = 0$,
where the prime indicating the derivative with respect to frequency. Thus,

$$\tilde{E}'(z,\omega = 0) = \Big(\prod_{n=1}^{N}(S_nS_\omega)\Big)'\tilde{E}(0,\omega = 0) \qquad (4.10)$$

Expanding this one writes*,

$$\tilde{E}'(z,\omega = 0) = \Big(\prod_{n=1}^{N}(S_nS_\omega)\Big)'\tilde{E}(0,\omega = 0) \qquad (4.11)$$

$$= S_N S_\omega \begin{pmatrix} b'\omega\Delta z & 0 \\ 0 & -b'\omega\Delta z \end{pmatrix} S_\omega^\dagger S_N^\dagger S_N S_\omega ... S_1 S_\omega \tilde{E}(0,\omega = 0)$$

$$+ S_N S_\omega S_{N-1} S_\omega \begin{pmatrix} b'\omega\Delta z & 0 \\ 0 & -b'\omega\Delta z \end{pmatrix} S_\omega^\dagger S_N^\dagger S_\omega^\dagger S_{N-1}^\dagger S_{N-1} S_\omega S_N S_\omega ... S_1 S_\omega \tilde{E}(0,\omega = 0)$$

$$+ ...$$

It is evident that every term is multiplied by the common factor $\prod_{n=1}^{N}(S_nS_\omega)$ this
implies,

---

*The symbol † represents the conjugate transpose matrix

$$
\tilde{E}'(z, \omega = 0) = \left(S_N S_\omega \begin{pmatrix} b'\omega\Delta z & 0 \\ 0 & -b'\omega\Delta z \end{pmatrix} S_\omega^\dagger S_N^\dagger \right.
$$
$$
+ \ S_N S_\omega S_{N-1} S_\omega \begin{pmatrix} b'\omega\Delta z & 0 \\ 0 & -b'\omega\Delta z \end{pmatrix} S_\omega^\dagger S_N^\dagger S_\omega^\dagger S_{N-1}^\dagger + ... \right) \left(\prod_{n=1}^{N} (S_n S_\omega) \right) \tilde{E}(0, \omega = 0)
$$

$$(4.12)$$

And finally by noticing that $\tilde{E}(z, \omega = 0) = \left(\prod_{n=1}^{N} (S_n S_\omega) \right) \tilde{E}(0, \omega = 0)$, Eq. 4.12 results in,

$$
\tilde{E}'(z, \omega = 0) = F\tilde{E}(z, \omega = 0) \tag{4.13}
$$

The factor F results from the summation term on the right hand side of Eq. 4.12, and is equal to

$$
F = ib'\Delta z \sum_{m=1}^{N} V_m \sigma_3 V_m^\dagger \tag{4.14}
$$

With σ_3 being the Pauli matrix,

$$
\sigma_3 = \begin{pmatrix} 1 & 0 \\ 0 & -1 \end{pmatrix} \tag{4.15}
$$

and $V_m = \prod_{n=m}^{N} (S_n S_\omega)$. Also,

$$
V_m \sigma_3 V_m^\dagger = \begin{pmatrix} x_{1,m} & x_{2,m} - ix_{3,m} \\ x_{2,m} + ix_{3,m} & -x_{1,m} \end{pmatrix} \tag{4.16}
$$

The variables x_1, x_2, x_3 represent coordinates on the Poincaré sphere, this choice of matrix is physically adequate and can be justified, as this will represent an optical element describing the rotation of a unit vector on the Poincaré sphere. From [59] the

DGD of the link is given as $< \Delta \tau^2 > = -4 < det(F) >$. In the heart of this relation lies the fact that the differential group delay is proven to be $\Delta \tau = 2\lambda$. Where $\pm \lambda$ is the eigenvalue that results by solving the eigenproblem of finding the principal states of polarisation that will remain unchanged to first order with respect to frequency. This is proven in [49] by finally stating that the spreading due to PMD is given by the difference of the derivatives of the phase of the signal with respect to frequency that is $d\phi_+/d\omega - d\phi_-/d\omega$ with $\phi_\pm$ being the phase of the fast and slow axis respectively. This is otherwise stated in Eq. 3.3. Then this is generalised with respect to the determinant of the transfer matrix F simply by noticing that $2\lambda = \sqrt{-4 < det(F) >}$. The radius that results from the determinant of $V_m \sigma_3 V_m^\dagger$ is then equal to $|x_{1,m}|^2 + |x_{2,m}|^2 + |x_{3,m}|^2 = 1$ and this produces finally a factor of N as it is added through the summation of Eq. 4.14. It is important to note that in general $< det(\sum A) > \neq < \sum(det(A)) >$, however in our case the variables are independent and thus we end up with the average of the squares of the three variables as well as the average of several products of those three variables which result in the averages of the individual terms that are in turn equal to zero so in out case in particular the rule $< det(\sum A) > = < \sum(det(A)) >$ holds. We thus obtain, $< \Delta \tau^2 > = 4(b')^2 \Delta z^2 N = 4(b')^2 \Delta z L$. From [60, 6], it is well known that $< \Delta \tau^2 > = 8(b')^2 L_{corr} L$, with L, L_{corr} being the total distance and the correlation length respectively. So this makes it obvious that there is an artificial rescaling of the DGD, as it is clearly derived from the above that the value for the PMD spreading will be modified by a factor of $(\Delta z/2L_{corr})^{1/2}$ if one uses the coarse-step method to numerically solve the PMD. The effect of the algorithm on the spreading of a signal for the two regimes, the short and the long distance regime, is shown in figures 4.6, 4.7 respectively by presenting the $\sqrt{< (\Delta T)^2 >} = \sigma_T$.

In figure 4.6 the coarse-step method is numerically solved and then compared with Eq. 3.29 for a PMD parameter $D_{PMD} = 0.5ps/(km)^{1/2}$. There is perfect agreement between simulation and theory as the random coupling is not included in the coarse-step method for this case, but only the differential group delay between the two modes, this implies that using $< \Delta \tau^2 > = -4 < det(F) >$, the result is always the same and equal to $< \Delta \tau^2 > = 4(b')^2 \Delta^2 N^2 = 4(b')^2 z^2$ which is the same result otherwise defined in Eq. 3.29. This result is shown, choosing for the simulation step size different values
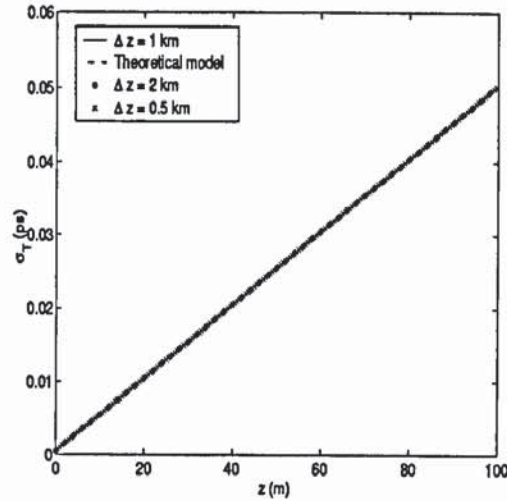
Figure 4.6: Evolution of the spreading of a signal due to PMD in the short distance regime

$\Delta z = 1, 2, 0.5$ meters and it is observed that the outcome is the same for all of these numerical estimates.
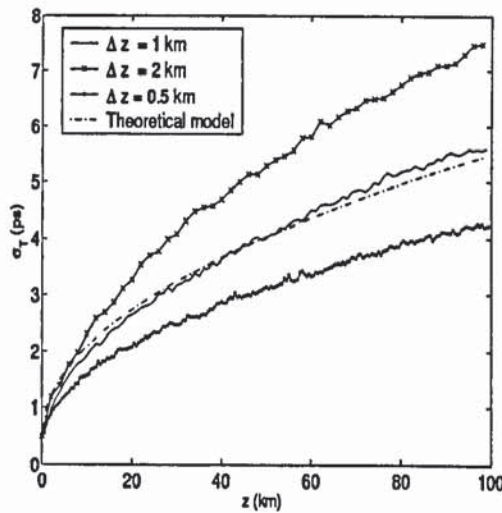
Figure 4.7: Evolution of the spreading of a signal due to PMD in the long distance regime based on the coarse-step method

Further the long-distance simulation is shown in Fig. 4.7 for $D_{PMD} = 0.5 ps/(km)^{1/2}$. Clearly the rescaling of the PMD resulting from the coarse-step method, as explained above, is observed. The curve given for 1km is simulated so that it agrees with the theoretical plot of Eq. 3.30, for what is more the curves for 2km and 0.5km differ by a $(\sqrt{\Delta z})$ term, from the theoretical curve as expected. So based on that, if one simulates

in a coarser way for more computational efficiency or if a better mixing, is required so
that one simulates on a shorter step and concatenates more rotational matrices then it
is necessary that the DGD is scaled by $\sqrt{1/\Delta z}$ in order to produce the accurate result
for the PMD so effectively $b'_{\Delta z} = b'(2L_{corr}/(\Delta z))^{1/2}$ where $b'_{\Delta z}$ the value that one needs
to choose for a given step size and b' the original value.

Chapter 5

Manakov-PMD equation theory and precomputed matrices

5.1 Review of the Manakov-PMD theory

The starting point for the second numerical algorithm is the Manakov-PMD equation as described in [61, 62, 63],

$$i\frac{\partial \Psi}{\partial z} - \frac{1}{2}\beta''\frac{\partial^2 \Psi}{\partial t^2} + \frac{8}{9}n_2 k_0 |\Psi|^2 \Psi = -ib'\sigma_3\frac{\partial \Psi}{\partial t} - \frac{1}{3}n_2 k_0 (\widehat{N} - <\widehat{N}>) \qquad (5.1)$$

The coefficients here are the equivalent of those appearing in the CNLS but it is worth defining them to clarify any slight differences in the notation. Where ψ represents the field, $b' = (\beta'_x - \beta'_y)/2$ is the group delay per unit length indicating the splitting of the two modes, β'' is the group velocity dispersion coefficient, n_2 is the Kerr coefficient, and $k_0 = 2\pi/\lambda$ and the primes denote differentiation with respect to frequency. This equation can be solved by the split-step Fourier method approach. This eventually will lead to two equations for the linear and the nonlinear part, these are the following,

$$\Psi(z + \Delta z, \omega) = \exp[\frac{i}{2}\omega^2\beta''\Delta z]M(\omega)\Psi(z, \omega) \qquad (5.2)$$

$$\Psi(z + \Delta z, \omega) = \exp[in_2 k_0 \frac{8}{9}|\Psi|^2\Delta z]\Psi(z, \omega) \qquad (5.3)$$

The linear part described by Eq. 5.2 appearing in the frequency domain includes the matrix $M(\omega)$ which is the solution of the differential equation,

$$i\frac{\partial M(z,\omega)}{\partial z} + (b + b'\omega)\Sigma(z)M(z,\omega) = 0 \tag{5.4}$$

with the initial condition,

$$M(z = z_0, \omega) = I \tag{5.5}$$

Where I is the 2×2 identity matrix

$$I = \begin{pmatrix} 1 & 0 \\ 0 & 1 \end{pmatrix} \tag{5.6}$$

Also b represents the birefringence parameter given by $b = (\beta_x - \beta_y)$ which is the difference between the two propagation constants for the two different polarisations. The factor $\Sigma(z)$ describes the evolution of the random change on the axes of birefringence that the signal experiences as it propagates through a fibre and it is equal to,

$$\Sigma(z) = \sigma_3 \cos(2\alpha(z)) + \sigma_1 \sin(2\alpha(z)) \tag{5.7}$$

Where σ_1, σ_3 are the standard Pauli matrices with σ_3 defined in Eq. 4.15 and

$$\sigma_1 = \begin{pmatrix} 0 & 1 \\ 1 & 0 \end{pmatrix} \tag{5.8}$$

It is clear that Eq. 5.4 tracks the rapid evolution of the angle on the actual length scale that this happens, within a meter or so. More specifically for each of these subintervals,

$$m(\omega) = \begin{pmatrix} m_{11} & m_{12} \\ m_{21} & m_{22} \end{pmatrix} \tag{5.9}$$

and for each of the components of these matrices one writes,

$$m_{11} = m_{22}^* = \cos\left[(b + b'\omega)\delta z\right] + i\cos(2\alpha_j)\sin\left[(b + b'\omega)\delta z\right] \tag{5.10}$$

$$m_{12} = m_{21} = i\sin(2\alpha_j)\sin\left[(b + b'\omega)\delta z\right] \qquad (5.11)$$

The individual α_j are constant in every subinterval of step-size δz. The matrices $M(\omega)$ at each of the standard simulation step-sizes Δz of the order of kilometres will then be given by the product of the sub-matrices,

$$M(\omega) = \prod_{j=0}^{N} m_j(\omega) \qquad (5.12)$$

The angles α_j are chosen so that they are randomly distributed. The second moment of this distribution is,

$$<(\Delta\alpha)^2> = \frac{\delta z}{2L_{corr}} \qquad (5.13)$$
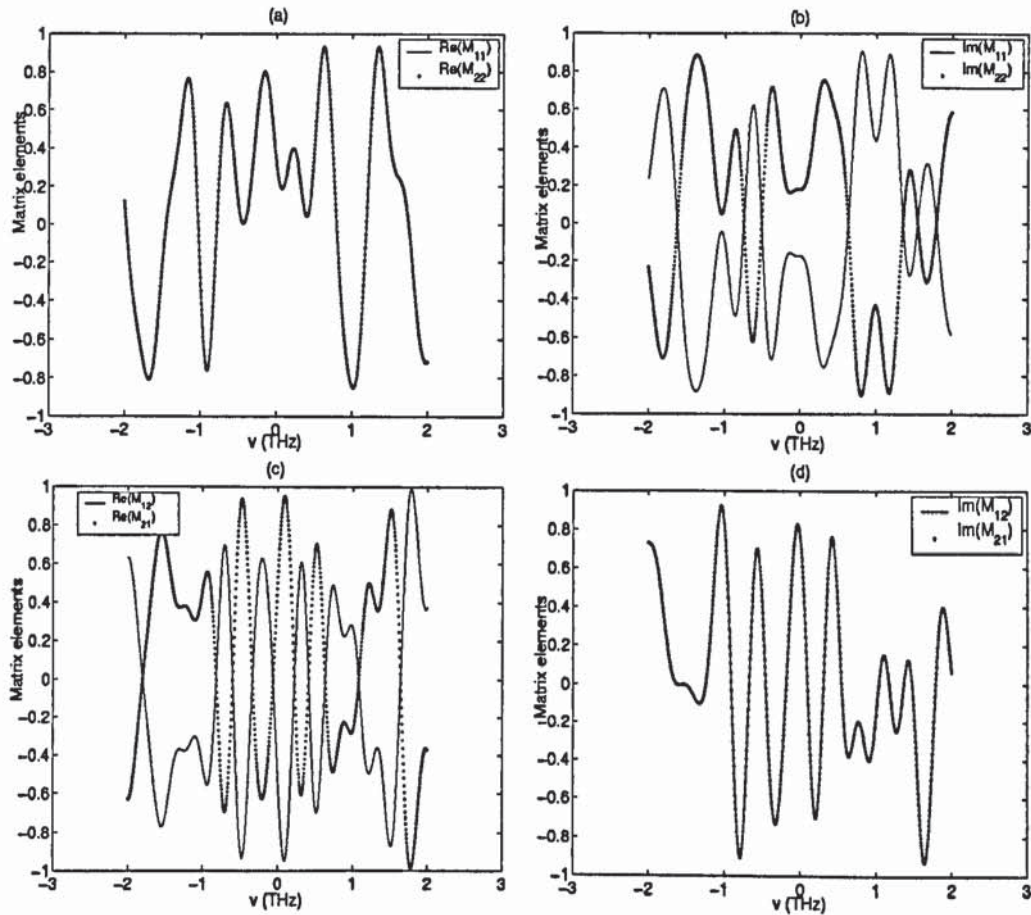
Figure 5.1: $M(\omega)$ matrices resulting from the Manakov-PMD equation (a),(b),(c),and (d) real and imaginary parts for the elements $M(1)(1), M(2)(2), M(1)(2), M(2)(1)$ respectively

Where L_{corr} is the correlation length [64, 65]. It should be pointed out that exactly because the Manakov-PMD equation follows the physical evolution of the angles this makes it more attractive than the coarse-step method. However the authors in [61] note the numerical inefficiency of this method as they followed the path that required for the matrices $m(\omega)$ to be computed at the small step size of δz and the matrices $M(\omega)$ in turn to be recomputed at every step Δz. As it is proposed through this thesis and proven later through our numerical investigation of this method it is possible to achieve great efficiency by just computing a limited number of matrices say 4~15 in the beginning of the simulation and choose between these at random at each step in the course of the transmission as they do not depend on the signal itself but just on the characteristics of the fibre. In figure 5.1 the real and imaginary parts of an $M(\omega)$ matrix is shown. It should be mentioned that a relation appears between the elements of this matrix, that is $M_{11} = M_{22}^*$, $\mathrm{Im}(M_{12}) = \mathrm{Im}(M_{21})$ and $\mathrm{Re}(M_{12}) = -\mathrm{Re}(M_{21})$. These expressions are true, and can be verified, if one produces the multiplication of Eq. 5.12.

5.2 Manakov-PMD matrices and distribution of a state of polarisation on the Poincaré sphere.

In a similar way to the one used for the coarse-step method the mixing on the Poincaré sphere is tested numerically by launching the signal with an initial polarisation and estimating the scattering on the sphere. In this case a CW initially polarised in $30°$ is used, which again is represented by a resolution of 2^{10} in a time window of 512 ps to test the algorithm over 5000 runs. This is done for a number of steps N = 1,2,4,10,100. However there are several options for each case, as one might choose to recalculate the matrices at every step or just precompute a number of matrices to test the system. Here both of these options are considered. For a number of steps N = 1, the following values for the number of matrices N_M are used N_M = 1,15,256 as well as computing a new matrix for every run. These results are shown in Fig. 5.2. The interpretation of these results is straightforward, the result by only precalculating a number $N_M = 1$ is presented in Fig. 5.2(a). For this case only one state of polarisation exists on the

sphere. For the complete opposite case, that is recalculating a new matrix in every run, the outcome is shown in Fig. 5.2(b) where the mixing is complete with $< s_1^2 > \approx 0.333$, $< s_2^2 > \approx 0.333$, $< s_3^2 > \approx 0.333$.
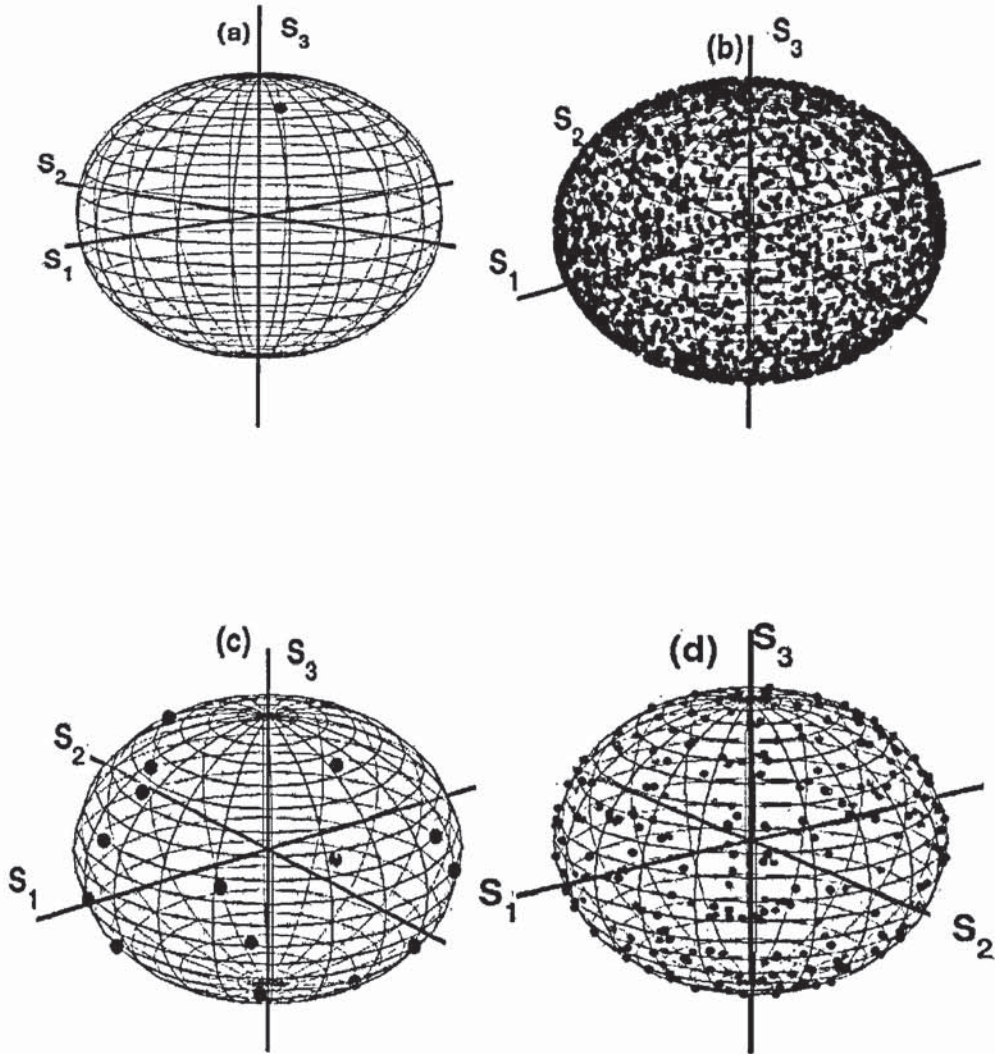
Figure 5.2: Distribution of the state of polarisation on the Poincaré sphere for the Manakov-PMD equation after $N = 1$ step for (a) $N_M = 1$, (b) recalculating N_M at every step, (c)$N_M = 15$ and (d) $N_M = 250$

Further, in Fig. 5.2(c) the algorithm is tested with a precomputed number of $N_M = 15$ matrices. As this is only one step iteration there are exactly 15 states on the Poincaré sphere. The three coordinates give $< s_1^2 > \approx 0.408$, $< s_2^2 > \approx 0.201$, $< s_3^2 > \approx 0.390$.

Last the method is given a number of precomputed matrices $N_M = 256$. In this case there are exactly 256 states on the sphere and $< s_1^2 > \approx 0.32903$, $< s_2^2 > \approx 0.33906$, $< s_3^2 > \approx 0.33189$.
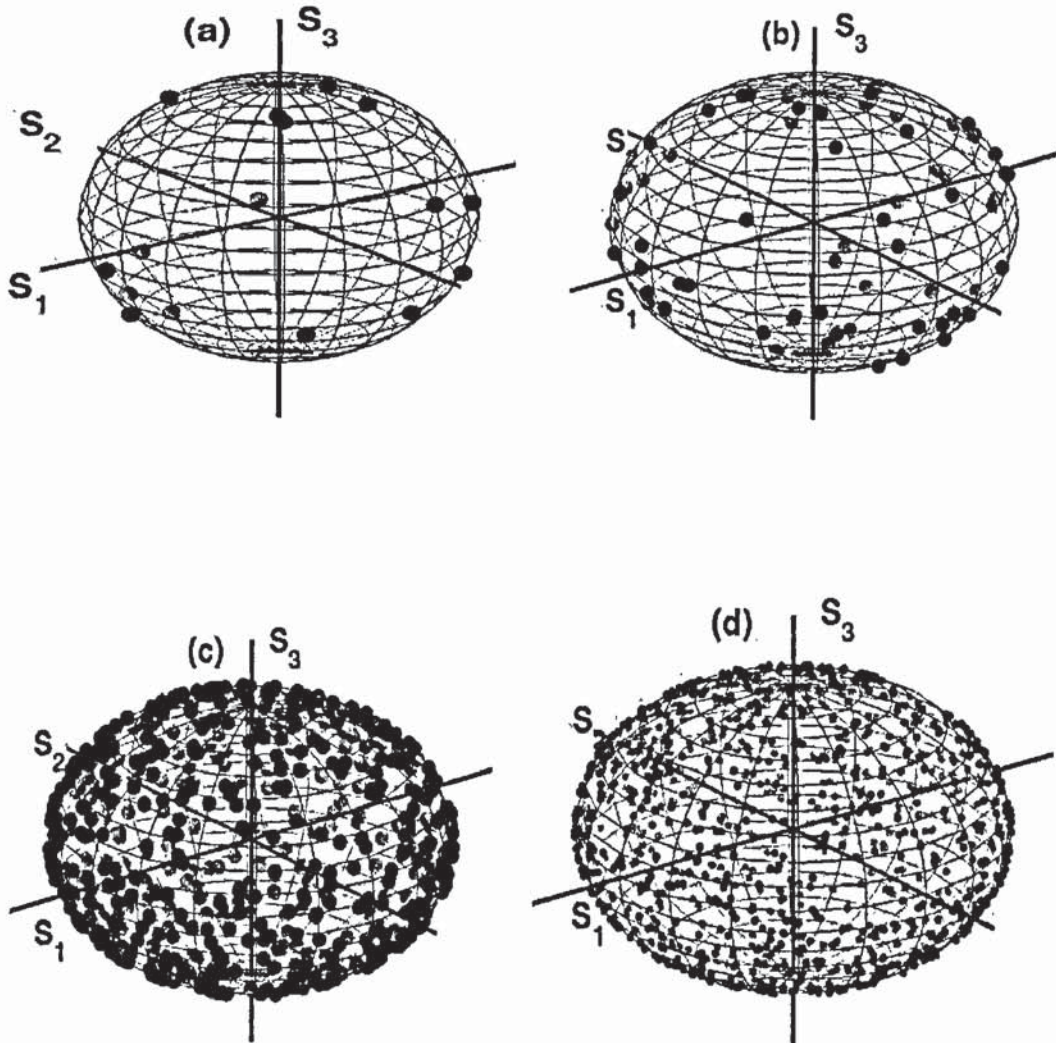
Figure 5.3: Distribution of the state of polarisation on the Poincaré sphere for the Manakov-PMD equation after $N = 2$ steps for (a) $N_M = 4$, (b) $N_M = 8$, (c) $N_M = 15$ and (d) $N_M = 32$

The same test was performed for $N = 2$ steps and the outcome is shown in Fig. 5.3. For $N_M = 4$ there are 16 output states of polarisation and for $N_M = 8$ there are 64 states of polarisation resulting. This stems from the fact that there are N_M^N combinations of

these matrices and thus the same number of output states. So as stated earlier for four matrices after two steps there are $4^2 = 16$ output states. The coordinates are $< s_1^2 > \approx 0.453$, $< s_2^2 > \approx 0.1429$, $< s_3^2 > \approx 0.403$ for $N_M = 4$ and $< s_1^2 > \approx 0.319$, $< s_2^2 > \approx 0.331$, $< s_3^2 > \approx 0.359$ for $N_M = 8$. Next the algorithm is simulated with a number $N_M = 15$ and thus having 225 output states. The three averages of the Stokes parameters are $< s_1^2 > \approx 0.335$, $< s_2^2 > \approx 0.321$, $< s_3^2 > \approx 0.345$. In Fig. 5.3(d) the result of using 32 matrices is shown, in this case $< s_1^2 > \approx 0.333$, $< s_2^2 > \approx 0.333$, $< s_3^2 > \approx 0.333$. Successively in Fig. 5.4 the mixing for $N = 4$ is shown.
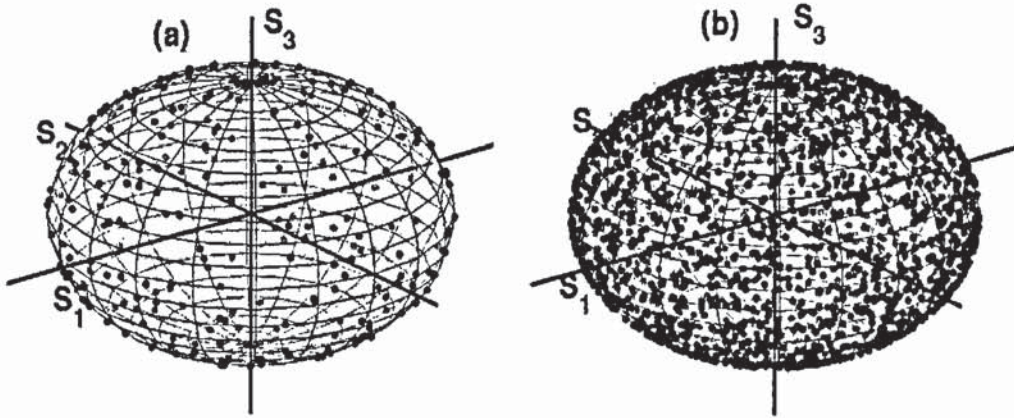
Figure 5.4: Distribution of the state of polarisation on the Poincaré sphere for the Manakov-PMD equation after $N = 4$ steps for (a) $N_M = 4$, (b) $N_M = 8$

Estimating the Stokes parameters for $N = 4$ and $N_M = 4$, these are $< s_1^2 > \approx 0.337$, $< s_2^2 > \approx 0.322$, $< s_3^2 > \approx 0.340$, while for $N_M = 8$ $< s_1^2 > \approx 0.333$, $< s_2^2 > \approx 0.333$, $< s_3^2 > \approx 0.333$. For what is more the same number of matrices are tested for $N = 10$ where for $N_M = 4$, $< s_1^2 > \approx 0.333$, $< s_2^2 > \approx 0.333$, $< s_3^2 > \approx 0.333$ also for $N_M = 8$, $< s_1^2 > \approx 0.333$, $< s_2^2 > \approx 0.333$, $< s_3^2 > \approx 0.333$ and further for $N = 100$ and also testing for $N_M = 4$ this results in $< s_1^2 > \approx 0.333$, $< s_2^2 > \approx 0.333$, $< s_3^2 > \approx 0.333$ and last having $N_M = 8$ we also find $< s_1^2 > \approx 0.333$, $< s_2^2 > \approx 0.333$, $< s_3^2 > \approx 0.333$. The pattern emerging from all the above simulations for the various number of steps and matrices is that as one moves toward higher values for N, then even by using lower values for N_M this results in a proper mixing on the Poincaré sphere.
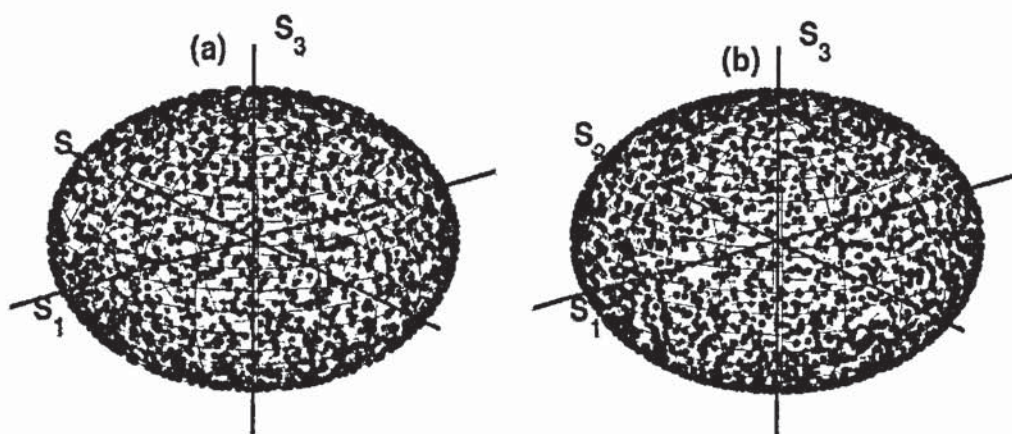
Figure 5.5: Distribution of the state of polarisation on the Poincaré sphere for the Manakov-PMD equation after $N = 10$ steps for (a) $N_M = 4$, (b) $N_M = 8$
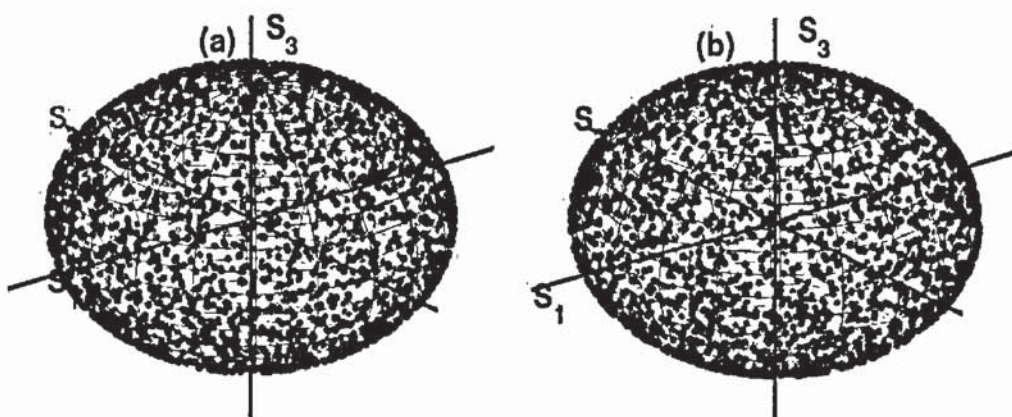

Figure 5.6: Distribution of the state of polarisation on the Poincaré sphere for the Manakov-PMD equation after $N = 100$ steps for (a) $N_M = 4$, (b) $N_M = 8$

Additionally it is observed that even for a value of N = 1 by recomputing the matrix resulting from the Manakov-PMD for every step results in the correct mixing on the Poincaré sphere. The objective is however to achieve the correct mixing on the sphere for only a few matrices so that this results in computational efficiency as well as physical accuracy. For a number of $N_M = 4$, through our simulations it is evident that uniform mixing will occur even for a number of steps N = 6. At this point it should be noted that for the coarse-step method the correct mixing will develop for N = 10 or further as proven earlier. From these results it is evident that it is correct to precompute $4 \sim 15$ matrices to simulate the phenomenon of PMD. The scattering of an SOP on the Poincaré sphere is not the only factor contributing to evaluating the Manakov-PMD algorithm. The probability density function (PDF) and the autocorrelation function (ACF) should be tested and compared to the analytical results. Such a comparison is given in chapter 6.

5.3 Manakov-PMD theory and dispersion of a signal

In this section the evolution of the dispersion of a signal is monitored in the two regimes, similarly to the coarse-step method. In Fig. 5.7 the PMD spreading in the short
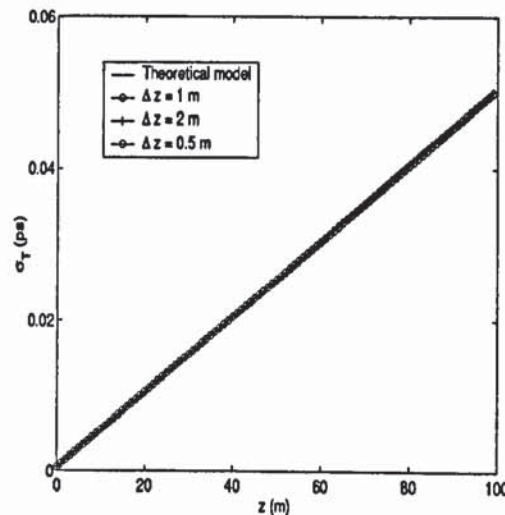
Figure 5.7: Evolution of the spreading of a signal due to PMD in the short distance regime based on the Manakov-PMD equation

distance regime is shown and compared to Eq. 3.29 over 100 meters. The parameters used are a $\Delta z = 1, 2, 0.5$ m and a $D_{PMD} = 0.5 \text{ps}/\sqrt{\text{km}}$. There is perfect agreement between simulation and theory as otherwise observed for the coarse-step method for this case. For the option of a longer distance this evolution is presented in Fig. 5.8. The parameters used in this case are a $\Delta z = 1, 2, 0.5$ km and $D_{PMD} = 0.5 \text{ps}/\sqrt{\text{km}}$.
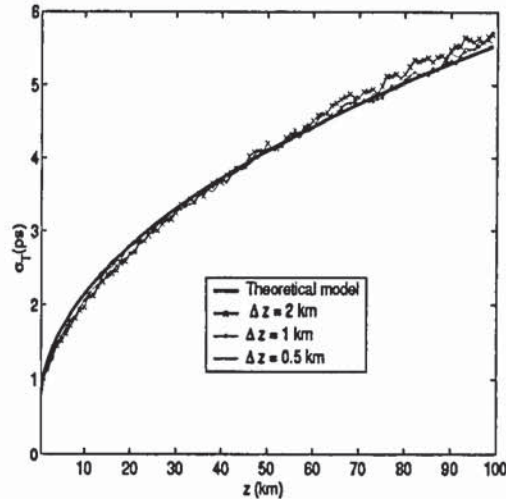
Figure 5.8: Evolution of the spreading of a signal due to PMD in the long distance regime based on the Manakov-PMD equation

Further for the long-distance regime there is a clear agreement between numerical results and theory irrespectively of the step-size used for the simulation in contrast to the coarse-step method. Which stems from the fact that the PMD phenomenon is physically accurately represented by the Manakov-PMD rather than the coarse-step method.

Chapter 6

Statistical validation and simulation results

6.1 Introduction and motivation for a statistical comparison of the numerical implementations of PMD

The coarse-step method [66, 67] is accepted as a numerically efficient method. Also in [61] it is stated explicitly that computing the $M(\omega)$ matrices is faster than integrating the Manakov-PMD equation in the short length scale of the order of meters so that the angle variation is included at every step of the integration. The question then would be how to implement the $M(\omega)$ matrices approach, so that it equals the coarse-step method in terms of numerical efficiency. In the case that this aim is achieved, the $M(\omega)$ matrices would be the preferred implementation as it is a physically accurate method resulting from the Manakov-PMD equation which takes into account a more detailed account for the evolution of the reorientation of the birefringence axes..

This can be accomplished by noticing that the matrices are eventually independent of the signal and can be precomputed. This implies that the matrices will not be recomputed at each step.

It would be better to take advantage of that in order to avoid the statistical problems of the coarse-step method, as given in [61] and explained in chapter 4, by using the Manakov-PMD equation.

6.2 Precomputing coefficients

The equation of $M(\omega)$ matrices depends on the orientation of the fibre axes and the birefringence. In these equations there is no dependence upon the signal itself. Polarisation mode dispersion is a statistical process, so that only one instance of the $M(\omega)$ matrices would not suffice to represent it accurately.

There are quite a few evidence though from papers on emulation such as in [68] that a few number of waveplates (≥ 15) would be enough. So even a smaller number of the Manakov-PMD matrices, since they represent better the rapid reorientation of the evolution angle, would suffice in our case to represent the phenomenon correctly.

The method proposed thus is the following. Computing a number of (N) matrices before starting the actual transmission and then during the simulation choose at random between these matrices, at each step of the simulation of a kilometre or more. On the top of that the same set of matrices can be used for different simulations, if for example, it is needed to produce an ensemble average so that there is no need to recompute these even in the case of different runs.

Getting into the numerical details of this comparison during the transmission it is clear that the two methods will not differ in terms of speed. The $M(\omega)$ method consists now of drawing one random number for the selection of the matrix at each step and then the multiplication of the matrix with the field. The coarse-step method consists of the splitting of the field which takes place when the linear part is computed through the Fourier transformation for each one of the polarisation modes and then again there is the draw of a random number and the multiplication for the rotation matrix exactly as in the case of the $M(\omega)$ matrices. From the physical perspective the matrices are a correct representation of the mixing on the Poincaré sphere since a single representation is derived through the integration of the Manakov-PMD and thus there exists the proper evolution of the rotation angle. In contrast the coarse-step method is the representation of PMD emulation. That is one random rotation takes place after the separation of the two modes. In no case does this present a correct mixing on the Poincaré sphere. At least a dozen number of steps are needed for the mixing to take place. In this way physically the scaling of the PMD with the step-size can be explained, as this would result to the linear PMD accumulating longer.

Further it is quoted in [61] that the coarse-step method inaccurately describes the nonlinear effect again in contrast to the $M(\omega)$ matrices. The last but interesting point that should be stressed is that these matrices provide access to all the elements of the fibre allowing to bias factors such as the angle and the birefringence and simulate more complex effects.

6.3 Analytical theory and numerical implementation of the PDF and the ACF of the PMD phenomenon

The conditions that should be satisfied as stated in [69] are the following,

1. The probability density function (PDF) of the DGD should converge to a Maxwellian distribution thus it should agree with the following equation

$$PDF(t)_{analytical} = \frac{8}{\pi^2 \Delta\tau} \left(\frac{2t}{\Delta\tau}\right)^2 \exp\left(-\frac{1}{\pi}\left(\frac{2t}{\Delta\tau}\right)^2\right) \tag{6.1}$$

2. The autocorelation (ACF) of the PMD vector should tend quadratically toward zero as it deviates from the central frequency reaching 10% for the background of the autocorrelation. Which in mathematical terms implies that the autocorrelation function should agree with the following equation.

$$ACF(\omega)_{analytical} = \frac{3}{\Delta\tau^2(\omega - \omega_0)^2} \left[1 - \exp\left(\frac{-\Delta\tau^2(\omega - \omega_0)^2}{3}\right)\right] \tag{6.2}$$

The numerical implementation used can be found in [69] and as follows,

$$ACF(\omega)_{numerical} = \left| \frac{\langle \Omega(\omega) \cdot \Omega(\omega_0) \rangle}{\langle \Omega(\omega_0) \cdot \Omega(\omega_0) \rangle} \right| \tag{6.3}$$

The parameters in these equations $\Delta\tau$, t, ω, $\Omega(\omega)$, stand for the total DGD, the time parameter, the frequency parameter and the PMD vector which can be computed as follows,

$$P(l,\omega) = \psi_u(l,\omega)\psi_u^*(l,\omega) + \psi_v(l,\omega)\psi_v^*(l,\omega) \tag{6.4}$$

$$s_1(l,\omega) = \frac{1}{P(l,\omega)}(\psi_u(l,\omega)\psi_u^*(l,\omega) - \psi_v(l,\omega)\psi_v^*(l,\omega))$$

$$s_2(l,\omega) = \frac{1}{P(l,\omega)}(\psi_u(l,\omega)\psi_v^*(l,\omega) + \psi_u^*(l,\omega)\psi_v(l,\omega))$$

$$s_3(l,\omega) = \frac{1}{P(l,\omega)}(\psi_u(l,\omega)\psi_v^*(l,\omega) - \psi_u^*(l,\omega)\psi_v(l,\omega))$$

Where $P(l,\omega)$, the power, $\psi_u(l,\omega)$, $\psi_v(l,\omega)$, $\psi_u^*(l,\omega)$, $\psi_v^*(l,\omega)$, the two orthogonal modes and their conjugates, $\mathbf{s}(l,\omega)$, the stokes vector and l the length of the fibre.

$$\Delta_-(l,\omega) = \mathbf{s}(l,\omega) - \mathbf{s}(l,\omega - \Delta\omega) \tag{6.5}$$

$$\Delta_+(l,\omega) = \mathbf{s}(l,\omega + \Delta\omega) - \mathbf{s}(l,\omega)$$

Where the $\Delta_-(l,\omega)$ and $\Delta_+(l,\omega)$ the two difference vectors,

$$\mathbf{e}_\Omega(l,\omega) = \frac{\Delta_-(l,\omega) \times \Delta_+(l,\omega)}{|\Delta_-(l,\omega) \times \Delta_+(l,\omega)|} \tag{6.6}$$

Here $\mathbf{e}_\Omega(l,\omega)$ is the direction of the PMD vector, and then the calculation of the angle θ between the $\mathbf{s}(l,\omega)$ and the PMD vector follows,

$$\cos\theta = \mathbf{s}(l,\omega) \cdot \mathbf{e}_\Omega(l,\omega) \tag{6.7}$$

and finally the modulus of the PMD vector,

$$|\Omega| = \frac{1}{\sqrt{1 - \cos^2(\theta)}}\left|\frac{d\mathbf{s}(l,\omega)}{d\omega}\right| = \tag{6.8}$$

$$\frac{\arccos(\mathbf{s}(l,\omega + \Delta\omega) \cdot \mathbf{s}(l,\omega)) + \arccos(\mathbf{s}(l,\omega) \cdot \mathbf{s}(l,\omega - \delta\omega))}{2\Delta\omega\sqrt{(1 - \cos^2(\theta))}}$$

The derivation of these expressions is given in Appendix C.

6.4 Statistical Comparisons

The simulation characteristics which we also used to demostrate these results in [70], were the following, a $D_{PMD} = 3$ ps/$\sqrt{km}$, correlation length of $L_c = 100$ m, beat length $L_{beat} = 50$m and step size $\Delta z = 1$ km. The smaller step-size to which the Manakov-PMD equation evolves is $\delta z = 1.67$m, thus Δz is divided in approximately 600 pieces. The optical spectrum of the simulation is 4 THz. This is represented as 2048 resolution points and a time window of 512 ps. The ensemble average was taken after 5000 initial conditions. Also it should be noted that no other effect is included focusing only on the $M(\omega)$ multiplication at each step.
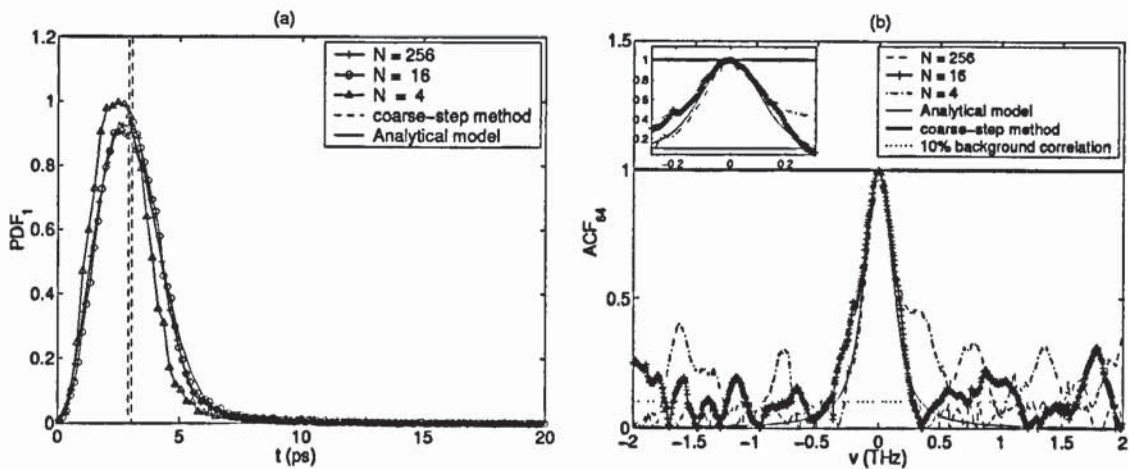
Figure 6.1: (a), (b), PDF and ACF for a distance 1 km comparing the $M(\omega)$ matrices algorithm, the coarse-step method and the analytical model of Eq. 6.1, Eq. 6.2 respectively. Results are compared by precomputing a number N = 256,16,4 of these matrices.

In figure 6.1 the probability density and the autocorrelation function for a transmission distance is given. Commenting on the PDF it should be noticed that the coarse-step method deviates completely from the analytical model, being concentrated on the value of 3 ps/$\sqrt{km}$ which is the value of the DGD per length. This is explained, as the coarse-step method in the first step includes only the splitting of the field into the two orthogonal eigenmodes without any mixing due to power coupling. The matrices of the Manakov-PMD equation include the mixing due to the evolution of the angle and thus the PDF approaches the theoretical expectation more so as the number of matrices increases so that there is more randomisation. In the case of the ACF again

a similar effect is produced, the coarse-step method is correlated completely as there is no randomisation, while the $M(\omega)$ matrices focus better around the area of the central frequency. Although the ACF of the 16 and 4 matrices peaks above the acceptable level of the 10% for frequencies that deviate from the central one, except for the case of 256 matrices which is correct, since if the number of matrices increases the mixing gets better.

Moving on to the distance of 2 km the following main points can be observed. In the case of the PDF the coarse-step method produces two peaks, each one for the two delays, to the fast and slow axis. While in the autocorrelation function of the coarse-step method there is a periodicity obtained, of peaks resulting at multiples $1/b'$. This is a numerical artifact inherent to the coarse-step method with a fixed DGD per-length which is the outcome of the numerical product of the fixed b' with frequencies multiples of π. For the case of the $M(\omega)$ matrices the agreement is much better so for the case of the PDF where the curves are nearly indistinguishable, as for the ACF where there is no periodicity and the background correlation is very close to the acceptable level of 10%.
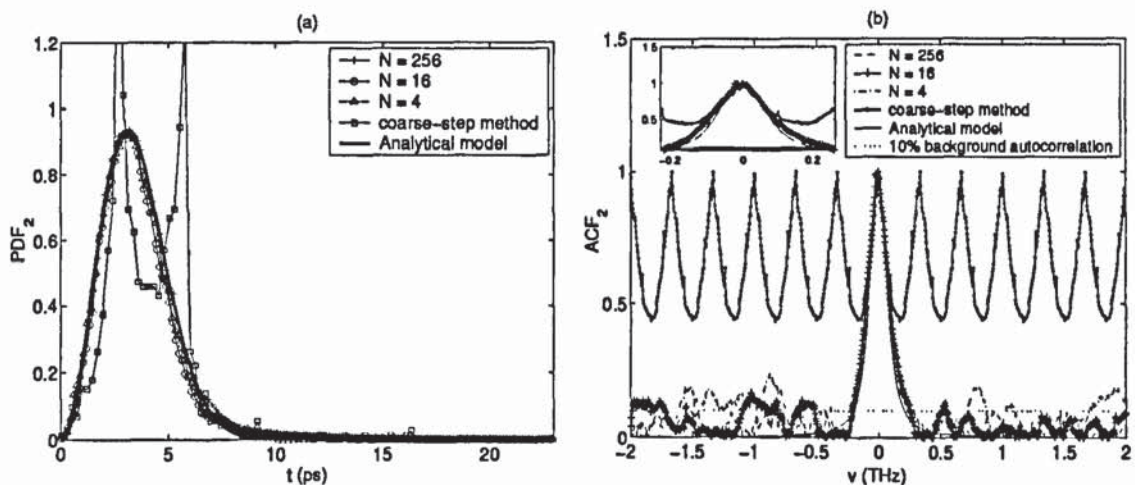
Figure 6.2: (a), (b), PDF and ACF for a distance 2 km comparing the $M(\omega)$ matrices algorithm, the coarse-step method and the analytical model of Eq. 6.1, Eq. 6.2 respectively. Results are compared by precomputing a number N = 256,16,4 of these matrices.

Furthermore the results of the 4, 8, 50 km transmission distance are presented. For each of these cases a dramatic change has occurred for the probability density of the coarse-step method. This amounts to the fact that, as the transmission gets longer

and longer there are more rotation matrices, at the end of each step contributing to a better mixing. The periodicity of the autocorrelation function remains because this effect is caused from the splitting of the two fields which always remains constant. For the $M(\omega)$ matrices the agreement is good for all cases both for the PDF and the ACF. Another important observation is that for all the distances of 4, 8, 50 km there is no significance difference between the set of N = 4, 16 and 256 matrices. For what is more for shorter distances even though the PDF and ACF improves as the number of matrices increases, still the matrices resulting from the integration of the Manakov-PMD give better results even for a small number of matrices, than the coarse-step method.

Regarding the speed of the method, and using as an example the 8 km simulation on a Pentium 3 processor with a CPU of 598.417 MHz, the time required for completing the work for the case of recomputing one matrix at each step was 10 hours. By precomputing 4 matrices the run time for the computation of the matrices required, was 7 seconds, while for the total simulation the time needed was 10 minutes. For the 16 matrices, their computation time was 28 seconds and the total simulation time 10 minutes 21 seconds. And last the 256 matrices needed approximately 7 minutes to be computed and the total simulation 17 minutes. For the coarse-step method the total time of the simulation added up to approximately 10 minutes. So there is no significant difference in terms of speed between the coarse-step method and the case of 4 or 16 matrices ($7 \sim 21$ sec), while indeed there is an enormous amount of computational time saved by using the algorithm instead of integrating the Manakov-PMD at each step.

Based on the above it is clear that the numerical algorithm devised from the Manakov-PMD algorithm has the same numerical efficiency as the coarse-step method. Moreover the physical description of the $M(\omega)$ matrices is the physical description based on the accumulation of the effect on the small length regime, while the coarse-step method, is a numerically adequate approximation, this is the reason behind the artificial rescaling. In terms of the simulation results presented it is obtained that statistically the proposed algorithm behaves better in the limit cases of 1 and 2 km of the PDF and it is clear that the ACF of the coarse-step method results in an unwanted
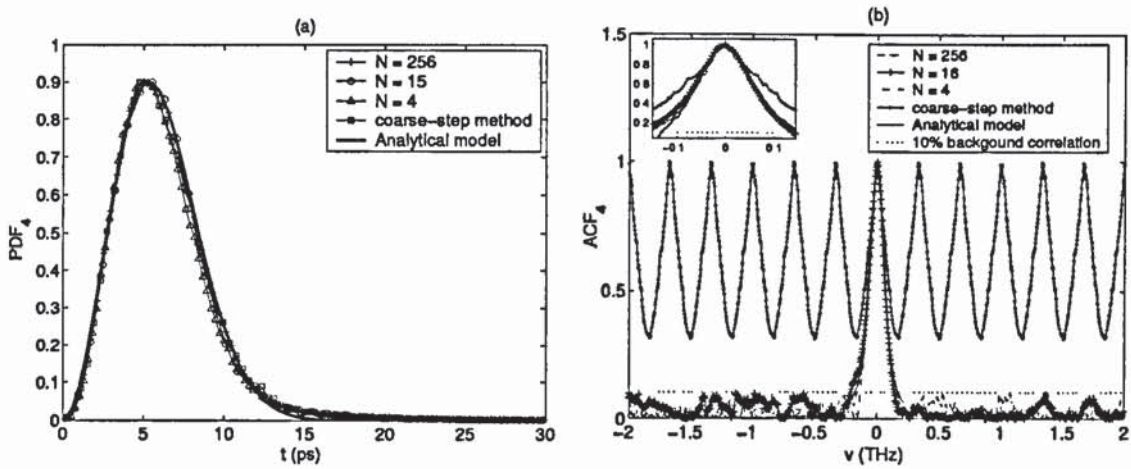
Figure 6.3: (a), (b), PDF and ACF for a distance 4 km comparing the $M(\omega)$ matrices algorithm, the coarse-step method and the analytical model of Eq. 6.1 and Eq. 6.2. Results are compared by precomputing a number N = 256,16,4 of these matrices.
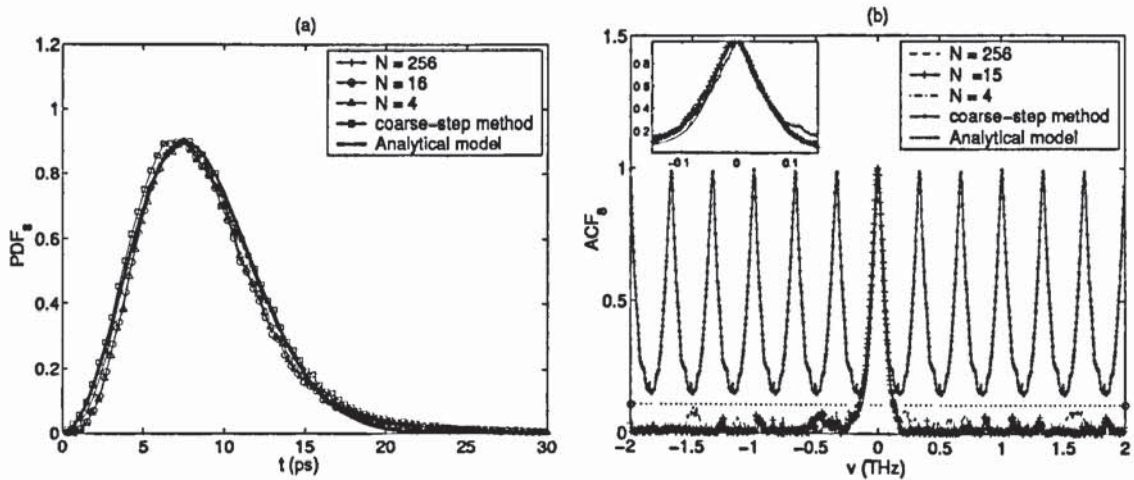
Figure 6.4: (a), (b), PDF and ACF for a distance 8 km comparing the $M(\omega)$ matrices algorithm, the coarse-step method and the analytical model of Eq. 6.1 and Eq. 6.2. Results are compared by precomputing a number N = 256,16,4 of these matrices.
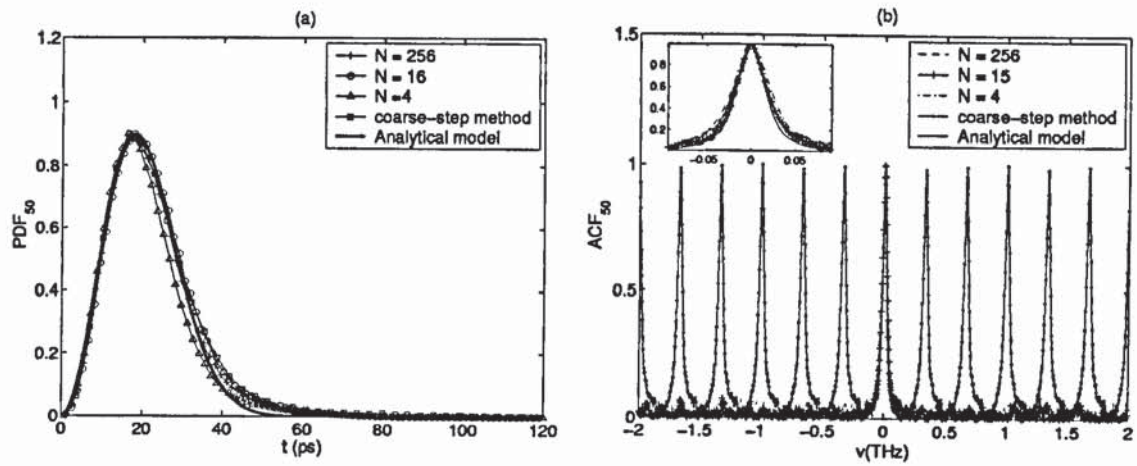
Figure 6.5: (a), (b), PDF and ACF for a distance 50 km comparing the $M(\omega)$ matrices algorithm, the coarse-step method and the analytical model of Eq. 6.1 and Eq. 6.2. Results are compared by precomputing a number N = 256,16,4 of these matrices.

periodicity. For the above reasons the $M(\omega)$ algorithm is more advantageous to use rather than the coarse-step method.

Chapter 7

PMD correlations with the coarse-step method

7.1 Theoretical background

The phenomenon of polarisation mode dispersion in optical fibres is normally modelled using the coarse-step method. This approach is based on the idea of replacing the continuous random birefringence by a sequence of randomly connected fibres each of which has a constant birefringence. It has been demonstrated [70] and shown in chapter 6 of this thesis, that this method produces an autocorrelation function (ACF), which is qualitatively different to the one calculated from a continuous analytical model. It is important to stress that the phenomenon has been observed experimentally in emulators [68, 69], that is, experimentally concatenating pieces of polarisation maintaining fibres with polarisation scattering at the beginning of each section but not in the context of numerical simulations, with the widely used coarse-step method.

The coarse-step method uses a constant differential-group delay (DGD)b' term which is applied after each integration step. This results in the polarisation ACF containing a series of harmonics instead of a single peak.

In this chapter as we demonstrated in [71, 72] we show that by allowing the DGD to vary from step-to-step the harmonic artifacts can be removed. In particular, we investigate the reduction of the side peaks as we gradually increase the number of dif-

ferent values from which we choose the DGD per length. We also allow the pool of random values to vary between a uniform and a Gaussian distribution and numerically we confirm that there is no difference in the long length regime.

7.2 Autocorrelation function of the coarse-step method

The periodicity of the ACF of the coarse-step method results numerically, from the splitting of the field to the two orthogonal polarisation modes which is the effect of the DGD per unit length.

It is convenient at this stage to represent the initial pulse as a delta function. Successively, after a number of simulation steps, and neglecting the power coupling which does not affect our case, the time domain picture will consist of a series of delta functions all of which are separated by a constant multiple of time determined by the constant parameter b'. Thus the autocorrelation of the series of delta functions in the frequency domain, will result in another series of regularly spaced delta functions.

Furthermore we can monitor the reduction of the side-peaks by having b' given as a variable chosen from a pool of random values that exist within a certain width. By gradually increasing the width of the distribution it is possible to measure the reduction of the first harmonic against the centre peak.

7.3 Numerical results

The simulations that were performed, refer to a system having the following characteristics $D_{PMD} = 3$ ps/(km)$^{1/2}$, correlation length $L_c = 100$ m, the integration step was 1 km while the optical bandwidth of the simulation was 4 THz represented by a resolution of 4096 sampling points. As can be seen in figure 7.1, using a fixed value DGD we obtain the periodic pattern in the ACF of the coarse-step method which deviates from the proposed analytic model as given in Eq. 6.2.

Continuously we use the "refined" coarse-step method. The value of b' is chosen from a range of random numbers spaced equally around the mean value of 3 ps/km. As presented in figure 7.2 the harmonics decrease as we draw more numbers for the value
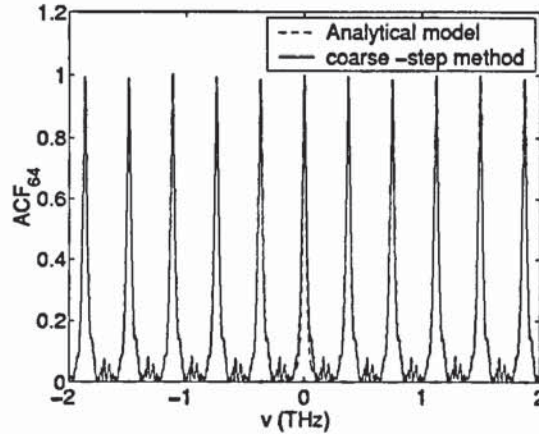
Figure 7.1: ACF of the coarse step method with a fixed DGD of 3ps/km for 64km compared to the analytical model of Eq. 6.2.

of b' and thus increase the range of choice. Initially we used a number N = 2 for b', choosing between 2.8ps,3.2ps. Progressively number N is increased to 4 numbers 2.6ps,2.8ps,3.2ps,3.4ps and finally we reach N = 8. The DGD in the last case varies between the values 2.2ps,2.4ps,2.6ps,2.8ps,3.2ps,3.4ps,3.6ps,3.8ps, thus having a range of 1.6ps around the average value of 3ps/km.
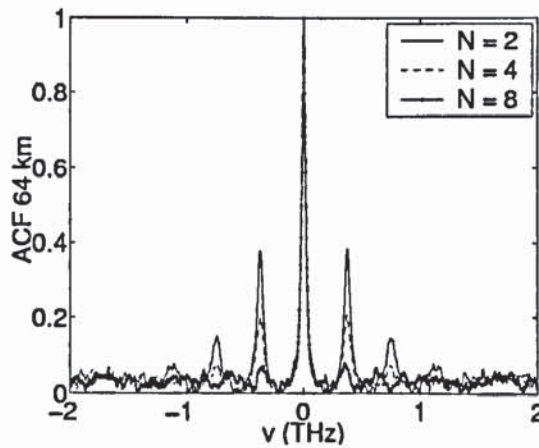
Figure 7.2: ACF simulations of the coarse-step method for an increasing number of values for the DGD per length, N = 2,4,8.

As shown in figure 7.3 it is obvious that the autocorrelation background will reduce to 10 % when we reach a value of 1ps for the width $\Delta b'$ of the random pool. We now use the modified coarse-step method for the option of using a Gaussian distribution for the random pool of $|b'|$. It is important to note that since the absolute value is used, the negative numbers for the birefringence that in any case have no physical meaning are
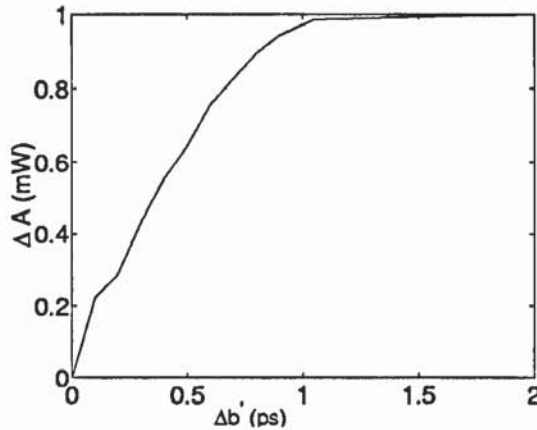
Figure 7.3: Evolution of the difference in amplitude between the fundamental frequency and the first harmonic for an increasing width of the random pool spaced evenly around an average b' of 3 ps/km.

discarded. In figure 7.4 we show that, even for a small variance for $|b'|$ of 0.05 ps, the harmonics of the ACF become suppressed. An important point to mention is that the reduction on the harmonics of the ACF is obtained in [73]. The authors there indicate that extra randomisation introduced by setting the DGD per length, of an emulator, from a Gaussian distribution leads to removing the periodicity gradually by increasing σ, the standard deviation of the distribution. The variance of $|b'|$ is increased to 1 ps
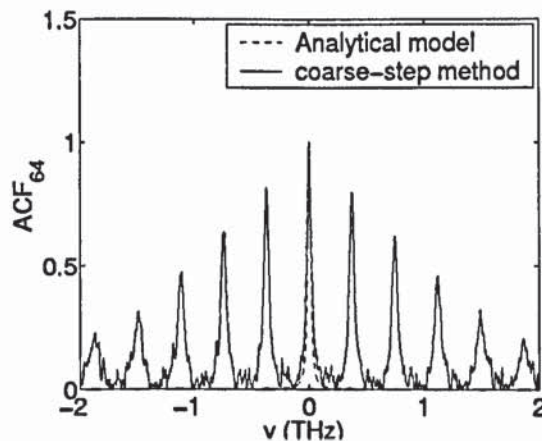
Figure 7.4: ACF of the coarse step method with DGD varying according to a Gaussian distribution of $\sigma = 0.05$ps and mean $\mu = 3$ps compared to the analytical model of Eq. 6.2, the transmission length was 64km.

in figure 7.5 where there are no longer any harmonics present and the central peak still agrees very well with the analytical prediction of Eq. 6.2. As the simulations have been performed in the long-length regime, different random distributions will produce

the same effect. This is demonstrated in figure 7.6 where a uniform and a Gaussian distribution of the same range produce the same effect on the harmonic artifacts. It is worth noting that the PDF of the DGD does not change significantly when we modify the coarse-step method, as it is shown in figure 7.7 thus it is correct to use the coarse-step method with a varying differential group delay model rather than the conventional one. Further we demonstrate results that are produced from introducing only two different values for b'. From figures 7.8 - 7.11 where we used randomly, one of two values (N = 2) for b' at each step, it is clear that the effect on the resulting ACF is multiplicative. Using only two values for b' though, results in harmonics existing within the bandwidth of interest. A better choice is to use 4 values (N = 4) as in figure 7.12 where the harmonics are totally eliminated within the frequency range of 4 THz. Thus instead of using a constant b'. Or randomising the DGD per unit length by recalculating this value at every step, based on the strategy of inserting a statistical distribution and gradually increasing the random pool of numbers we choose from, as in [73]. It was proven more numerically efficient to precalculate four numbers, that meet at higher frequencies, in the beginning of the simulation, and choose between these values at random, at every step to enlarge the bandwidth of transmission in order to produce a simulator that can accommodate WDM systems.
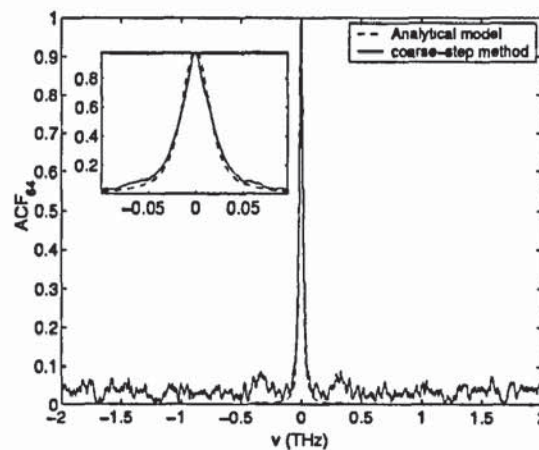
Figure 7.5: ACF of the coarse step method with DGD varying according to a Gaussian distribution of $\sigma = 1$ps and mean $\mu = 3$ps compared to the analytical model given by Eq. 6.2, the transmission length was 64km.

More specifically for a computer with the same CPU specifications, as previously given it was possible to reduce 1 hour of run time by 10 min this due to the fact that
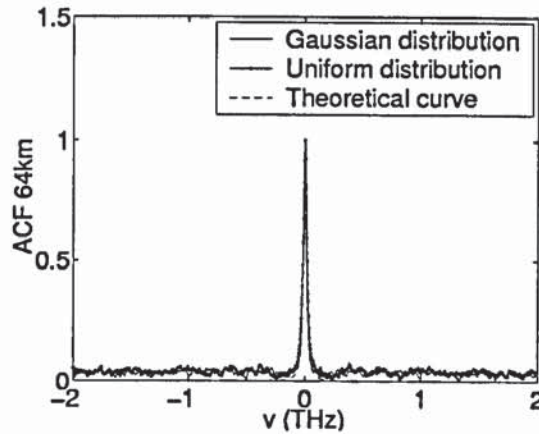
Figure 7.6: Results for the ACF of two different type of distributions, a uniform and a Gaussian
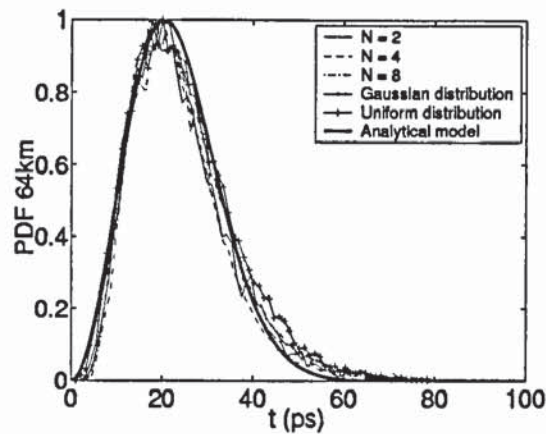
Figure 7.7: Comparison of the PDF simulations of the refined coarse-step method with a varying DGD. Results are presented for N=2,4,8 a uniform and a Gaussian distribution.
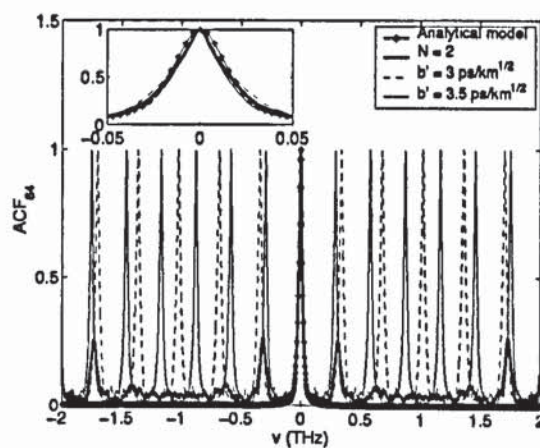
Figure 7.8: Results for the ACF, choosing $b' = 3$ ps or $b' = 3.5$ ps randomly at each step and comparing with the individual ACF for each of these two values
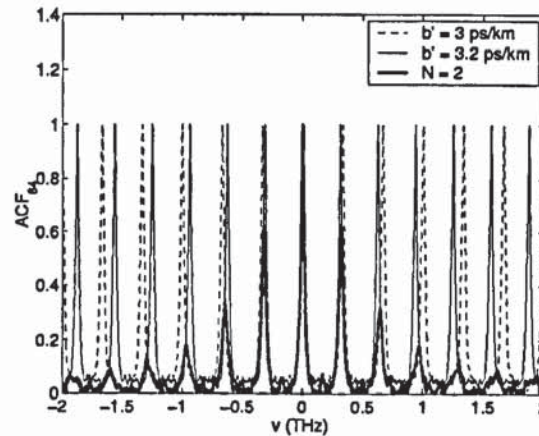
Figure 7.9: Results for the ACF, choosing $b' = 3$ ps or $b' = 3.2$ ps randomly at each step and comparing with the individual ACF for each of the two values
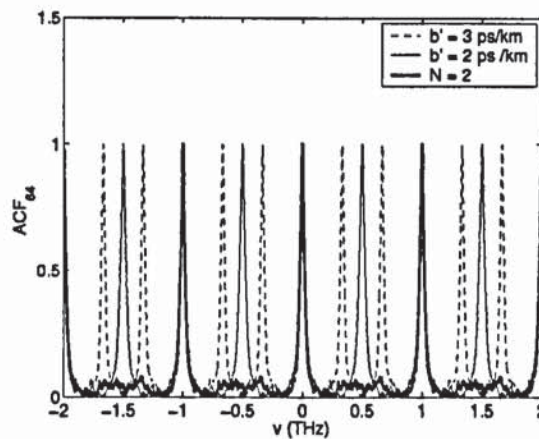
Figure 7.10: Results for the ACF, choosing $b' = 3$ ps or $b' = 2$ ps randomly at each step and comparing with the individual ACF for each of the two values
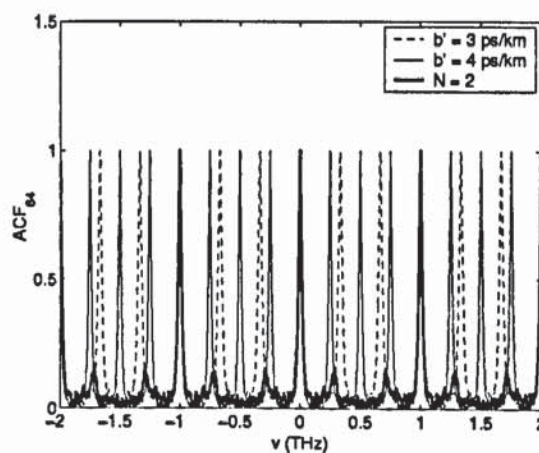
Figure 7.11: Results for the ACF, choosing $b' = 3$ ps or $b' = 4$ ps randomly at each step and comparing with the individual ACF for each of the two values
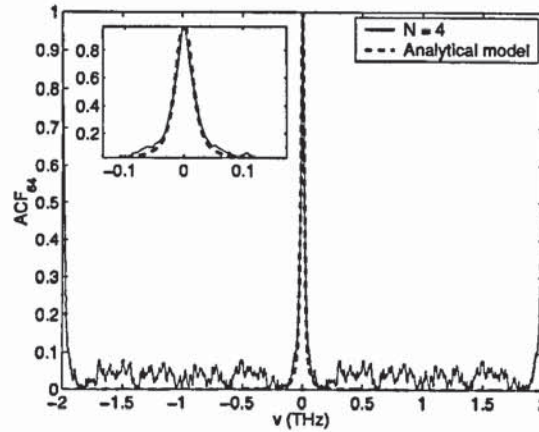
Figure 7.12: Results for the ACF, choosing b' from the values 2,4,2.5,3.5 ps randomly at each step and comparing with the analytical curve

the function to call for the various probability distributions get additively more time consuming than the proposed method.

Chapter 8

Numerical implementation of Low-PMD spun fibres

8.1 Introduction to PMD mitigation

At this stage and after introducing the statistical validations of all methods, it is straight forward to obtain a mitigation mechanism of the PMD by implementing Low-PMD spun fibres as we demonstrated in [74, 75] through the approach of the precomputed M(ω) matrices.

Experimentally, the class of low-PMD spun fibres, refers to an artificial spin that has been induced through the medium in the drawing process [76]. The correlation length of the birefringence L_{corr} shortens and as a result the polarisation evolves faster through the several stages. Because of its $L_{corr}^{1/2}$ dependence the differential group delay(DGD) $< \Delta\tau >$ is reduced. Numerically we introduce the artificial spin by adjusting the precomputed M(ω) matrices that result from the integration of the Manakov-PMD equation.

8.2 Theoretical approach

It is clear that $M(\omega)$ matrices depend on parameters such as b,b',a_z. The distribution of the angle can be accurately represented by a Gaussian, dispersing slightly around the mean induced spin $\delta\alpha$. Offsetting the angular Gaussian distribution by the fibre spin

the principal states of polarisation will couple faster and thus the overall PMD effect should be reduced. As in [34] the spreading of the angular distribution, according to which the angle will evolve is defined as,

$$<(\Delta\alpha)^2> = \frac{\delta z}{2L_{corr}} \tag{8.1}$$

8.3   Numerical implementation

The system tested had the following characteristics, a $D_{PMD} = 3ps/\sqrt{(km)}$, correlation length $L_c = 100m$, and integration step of 1 km . In figure 8.1, the evolution of the DGD distribution is shown. As we include a fibre spin and gradually increase it, the probability distribution of the DGD $< \Delta\tau >= 24ps$, progressively shifts to lower values 21ps, 18ps for a spin of respectively 0.3 rad/m, 0.4 rad/m.
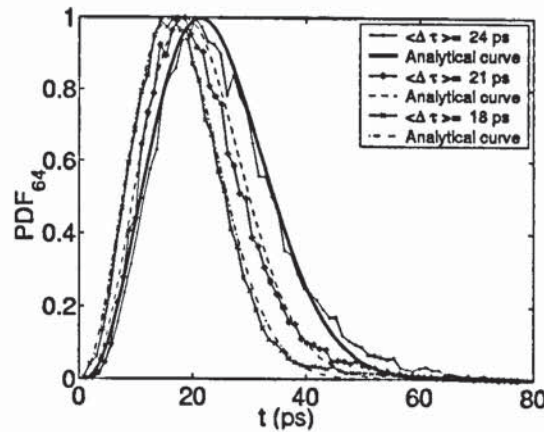
Figure 8.1: PDF of the DGD for different values of circular birefringence.

The background autocorrelation should tend rapidly toward zero as demonstrated in figure 8.2, so that the modified algorithm agrees with the theoretical requirements of PMD emulation theory that were given in section 3.6, thus it is stated through this test that by including a spin, this does not add any unwanted correlation artifacts in the ACF. Furthermore it is evident that the correlation length L_{corr} has an inverse proportional relation to the angular distribution of the fibre. Moreover in the long-length regime the total DGD scales with the square-root of the correlation length. From the above we conclude that $< \Delta\tau >\propto 1/< (\Delta\alpha)^2 >^{1/2}$ since $< (\Delta\alpha)^2 >= < (\Delta\alpha) >^2 +$

$(\Delta\alpha)^2$. In figure 8.3 the numerical results for the DGD for successive values of fibre spin is given and compared against an analytical model based on [77] for different values of constant spin $< (\Delta\alpha) >$ thus,

$$< \Delta\tau >= \frac{bb'\sqrt{L}}{\sqrt{b^2 + 4< (\Delta\alpha) >^2}} \tag{8.2}$$
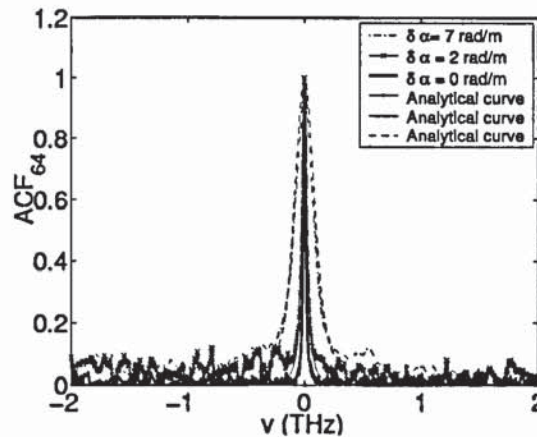
Figure 8.2: ACF for different values of the fibre spin against the theoretical model at a propagation distance of 64km.
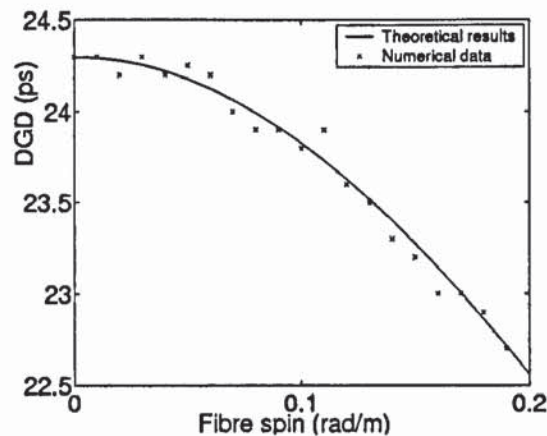
Figure 8.3: Evolution of the mean DGD $< \Delta t >$ against the theoretical model of Eq. 8.2

In conclusion for the first time we report the implementation of Low-PMD fibres with the Manakov-PMD equation. This is a "passive" element for PMD management, as it will compensate the polarisation dispersion for a certain value which will relate to the artificial spin that one includes in the drawing process of the fibre.

Chapter 9

Simulation results for transmission systems with PMD impairments

9.1 Introduction

Continuously we present our results concerning the Q-factor of transmission systems including PMD as well as other effects such as nonlinearity, losses and dispersion. For this purpose a numerical solver of the CNLS was implemented using the split step Fourier method. In this implementation, the fibre component included nonlinearity, dispersion and PMD. Also other components were implemented for the needs of the simulations and then incorporated into the general model, such as amplifiers and filters.

9.2 NRZ transmission

The first system demonstrates the propagation of a 10 Gbit/s NRZ pseudorandom bit-pattern. The launch power is 3 dBm. A rectangular optical filter of 2 THz is used in the amplifier. Another electrical filter is included in the receiver with 20 GHz bandwidth. We used 2^8 bits and a resolution of 2^{14}. The width of the time window is 25.6 ns.

The periodic map which we used to produce the same results for [75] and as presented in [47], used is shown in figure 9.1. The SMF fibre has a dispersion coefficient of 18 ps/nm/km, 80 μm^2 effective area and 0.2 dB/km loss. For the case of the system presented the DCF has a dispersion coefficient of -18 ps/km/km, 80 μm^2 effective

area and 0.2 dB/km loss, the amplifier has a saturation power of 3 dBm while the
spontaneous emission factor is 1.5.
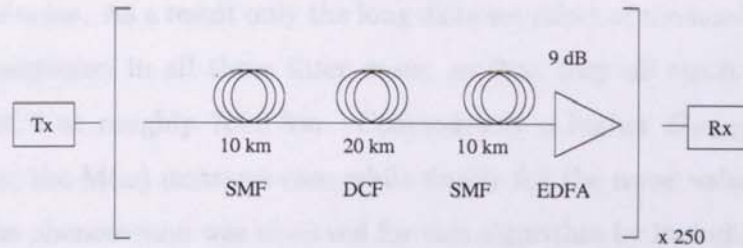
Figure 9.1: NRZ Transmission system.
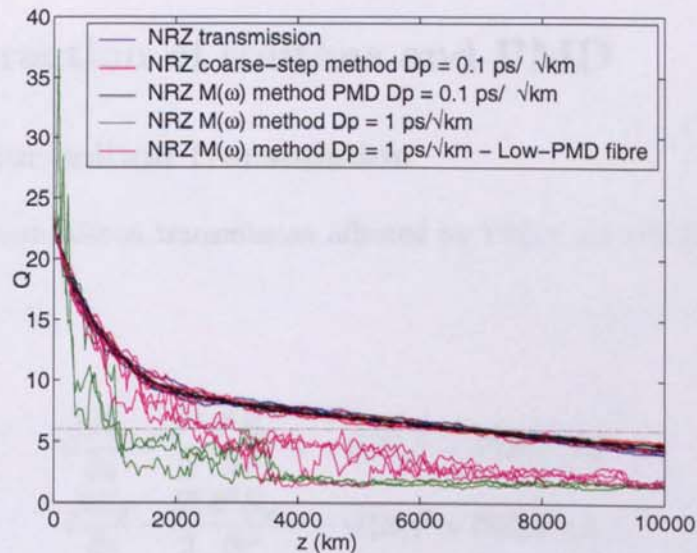
Figure 9.2: Q-factor performance for the NRZ transmission system of Fig. 9.1 (blue
line), using the coarse-step method with a $D_{PMD} = 0.1$ ps/$\sqrt{\text{km}}$ (red line), using
the $M(\omega)$ matrices for the same D_{PMD} value (black line), using the $M(\omega)$ matrices
for a $D_{PMD} = 1$ ps/$\sqrt{\text{km}}$ value (green line) and implementing low-PMD fibres after
increasing the D_{PMD} value to $D_{PMD} = 1$ ps/$\sqrt{\text{km}}$ (magenta) through the Manakov-
PMD matrices

In figure 9.2 the results of this simulation are shown. The NRZ bit-pattern was
transmitted without the effect of PMD and then with added PMD of a $D_{PMD} =$
0.1ps/$\sqrt{\text{km}}$. This was done both with the coarse-step method and the $M(\omega)$ matrices
approach. Because of the nature of the low PMD the phenomenon does not affect
significantly the transmission. At the same time the dispersion is compensated exactly
because of the periodic map as well as the losses since there is an amplifier included
in the transmission. It should also be noted that the amplifier formula used for the

gain, included the effect of the saturation of the amplifier, so that the gradual increase
in power of the signal as a result of excessive gain can be avoided. Commenting
further it was proven that the filtering used was adequate to eliminate any significant
accumulation of noise. As a result only the long distance effect of the nonlinearity really
affects the transmission in all these three cases, so that they all reach the threshold
of a Q-factor of 6 at roughly 7000 km. Continuously a higher $D_{PMD} = 1\text{ps}/\sqrt{\text{km}}$
was included for the $M(\omega)$ matrices case while finally for the same value of PMD the
mitigation of the phenomenon was observed for this algorithm by including a fibre spin
and thus implementing Low-PMD fibres, extending the distance for approximately
1000 km.

9.3 Interaction of solitons and PMD

9.3.1 Vector soliton transmission

In order to achieve soliton transmission affected by PMD, the CNLS in the following
form was used,

$$i\frac{\partial E_x}{\partial z} - \frac{\beta''}{2}\frac{\partial^2 E_x}{\partial t^2} = -\gamma(|E_x|^2 + B|E_y|^2)E_x \tag{9.1}$$

$$i\frac{\partial E_y}{\partial z} - \frac{\beta''}{2}\frac{\partial^2 E_y}{\partial t^2} = -\gamma(|E_y|^2 + B|E_x|^2)E_y \tag{9.2}$$

where this is identical to Eqs. 2.34,2.35 but the four-wave mixing term is dropped
as it is not used in the simulations and the new parameter B [78, 79] introduced
in this equation is the ellipticity parameter. That is the fibre might not be linearly
birefringent but a certain ellipticity can be introduced in the preform so that the two
nonlinear components will couple through the XPM term but the variable B will have
a different value.

To demonstrate the resilience of soliton transmission in terms of the GVD of a
link, a first order ($N = 1$) soliton pulse was launched through a fibre of 10000 km
having a GVD parameter $\beta'' = -1.275\text{ps}^2/\text{km}$, and an effective area $A_{eff} = 80\mu\text{m}^2$. A
hyperbolic secant format was used for the pulse such that,

$$E_x = \sqrt{P_0}\cos\theta\,\mathrm{sech}(\frac{T}{T_0}) \qquad (9.3)$$

$$E_y = \sqrt{P_0}\sin\theta\,\mathrm{sech}(\frac{T}{T_0}) \qquad (9.4)$$

where T_0 is the full-width of the pulse, T the time parameter, θ is the polarisation
angle which in this case was set to be $30°$ the peak power $P_0 = 0.121\mathrm{W}$ and finally
the full width at half maximum of the pulse was set as $T_{FWHM} = 5\mathrm{ps}$, of course the
peak-power and the the parameter of T_{FWHM} of the pulse are related by the expression
$P_0 \approx \frac{3.11|\beta''|}{\gamma T_{FWHM}^2}$ resulting by equating the nonlinear length and the dispersion length.
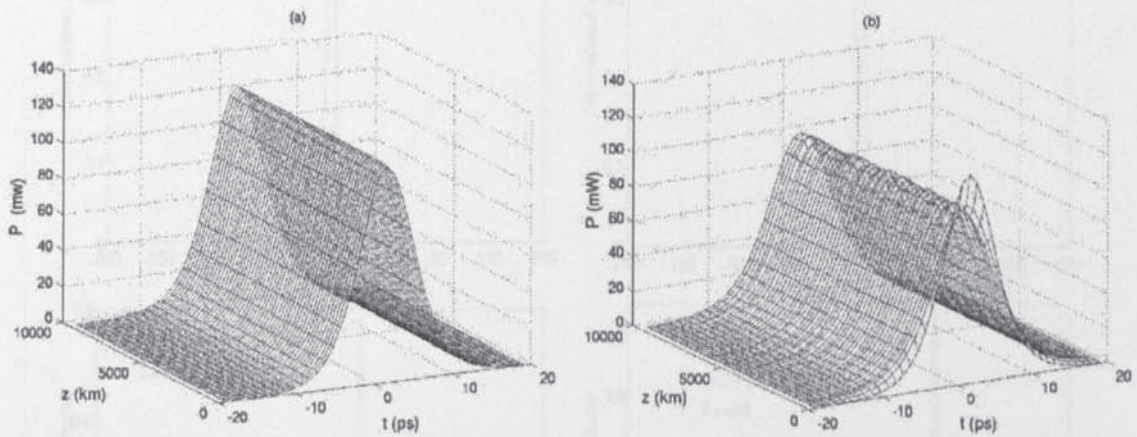
Figure 9.3: Transmission of the fundamental soliton for (a) B = 1 and (b) B = 2/3

In figure 9.3 the transmission results that are presented, demonstrate the transmis-
sion of a pulse through a fibre of (a) $B = 1$ and (b) $B = 2/3$ for the given parameters.
In the first case the soliton is transmitted undistorted through the duration of the total
transmission distance of 10000 km. This is expected and theoretically obtained in [80],
as the nonlinear phase term including the SPM and XPM term is the same for both
polarisations. In this case the soliton that results is directly derived from the CNLS
equation by using the inverse scattering method [81]-[90]. Generally though if the fibre
has not been manufactured for a B = 1 this would imply that B = 2/3 for a linearly
birefringent fibre which is represented by figure 9.3(b), where the soliton does not prop-
agate undistorted but nonetheless exhibits the properties of soliton propagation in a
sense that retains its intensity profile and does not disperse significantly due to GVD
[91]-[95].

9.3.2 Soliton trapping

The robustness of the PMD phenomenon stems from the XPM term that couples the
two directions. If $B = 0$ then the two components decouple and propagate as two
independent pulses after a constant DGD is applied at each step. The effect of the
XPM term has been investigated through theoretical results and numerically [96, 97].
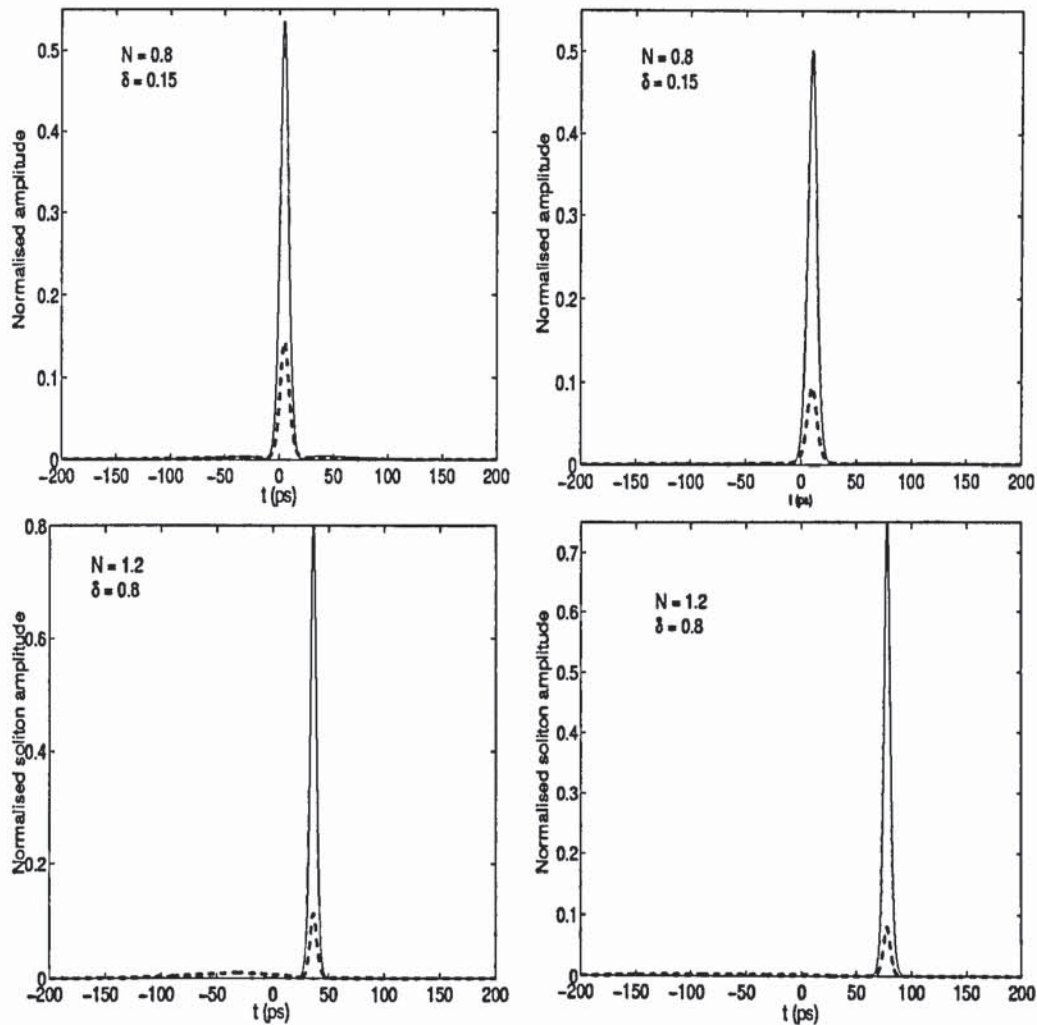
Figure 9.4: The two orthogonal modes $|u|$ (solid line) and $|v|$ (dashed line) after a
distance z = 300 km (first column) and z = 600 km (second column) for a signal
polarisation of $30°$. The soliton order N = 0.8 and the group velocity mismatch $\delta = 0.15$
for the first row while N = 1.2 and $\delta = 0.8$ for the second row.

Following the results of reference [97], numerical simulations were performed for a
soliton pulse launched at a polarisation of $30°$ represented by a time window of 1200 ps
and a resolution of 2^{11} points. The results are shown in figure 9.4 for a $\delta = 0.15$ps and

then for a $\delta = 0.8$ps. Following the formalism of [97], the parameter N is the soliton order included in the normalised field equations for the two modes,

$$u = N \cos \theta \mathrm{sech}(\tau) \tag{9.5}$$

$$v = N \sin \theta \mathrm{sech}(\tau) \tag{9.6}$$

and parameter δ is introduced and represents the group-velocity mismatch for the case of the normalised CNLS equation which is written as,

$$i\left(\frac{\partial u}{\partial \xi} + \delta'\frac{\partial u}{\partial \tau}\right) + \frac{1}{2}\frac{\partial^2 u}{\partial \tau^2} = -(|u|^2 + B|v|^2)u \tag{9.7}$$

$$i\left(\frac{\partial v}{\partial \xi} - \delta'\frac{\partial v}{\partial \tau}\right) + \frac{1}{2}\frac{\partial^2 v}{\partial t^2} = -(|v|^2 + B|u|^2)v \tag{9.8}$$

where $\xi = z/L_D$ the normalised distance and L_D the dispersion length $L_D = T_0^2/|\beta''|$, the normalised time parameter $\tau = (t/T_0)$ and $\delta = (\beta'_x - \beta'_y)T_0/2|\beta''|$. The two different values of δ were tested for different values of N that is N = 0.8 and N = 1.2 respectively. Each one was transmitted to the distances of 300 and 600 km. The results of figure 9.4 can be interpreted as follows, when the birefringence of the signal is small enough so that the two pulses do not drift apart fast, then the higher amplitude pulse will envelope above the smaller amplitude one and the two will continue to propagate with the same group velocity. From a physical viewpoint the two pulses shift their carrier frequencies so that they achieve a synchronisation in the time domain. This is defined as soliton trapping. If the δ is larger though then a portion of the smaller pulse will not be captured by the larger amplitude mode and thus dispersive waves will be created. For a larger group-velocity mismatch the soliton may give significant dispersive waves and breathers for a random initial polarisation ($\theta \neq 45°$). The general rule is that the value of N needs to be above a certain threshold [98]-[103] so that the two solitons remain bound together. This value is proportional to δ this is the reason that for different values of δ we used different N values in the simulations presented. In the next paragraph the power-coupling between the two modes is included so that the complete picture of PMD is incorporated in the simulations.

9.3.3   Q-factor and soliton transmission

The effect of soliton trapping implies that the soliton transmission should be more stable under the influence of PMD in contrast to a linear transmission. This is due to the fact that the trapping implies that soliton pulse will adjust itself to the mismatch of the group-velocities of the two modes and will preserve its profile by simultaneously emitting dispersive wave as summarised in paragraph 9.3.2.

To simulate the effect of PMD we transmit a non-soliton pulse through a fibre of 2000 km with $\beta'' = -1.275 ps^2/km$, $A_{eff} = 80\mu m^2$, and a DGD per length $\delta = 0.15$.
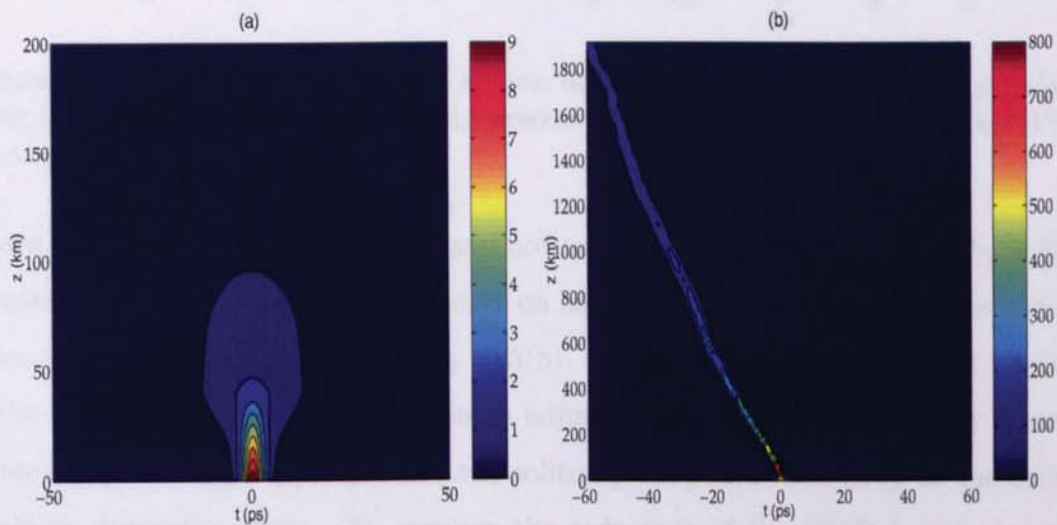
Figure 9.5: PMD transmission for a Gaussian pulse of peak-power (a) $P_0 = 10$ mW (b) $P_0 = 0.5$ W

In figure 9.5(a) we use a Gaussian pulse with a polarisation angle of 30°, a peak power $P_0 = 10$mW and finally the full width at half maximum of the pulse $T_{FWHM} = 5$ps, in this case the pulse collapses completely after the accumulated dispersion of both the GVD and PMD. In the second part of this figure (Fig. 9.5 (b)) a pulse of $P_0 = 0.5$W is used. In this case the pulse again collapses but this time under the effects of PMD and nonlinear phase accumulation as the power of the pulse excites the nonlinear refractive index of the fibre.

Next in figure 9.6 (a),(b) a soliton transmission is presented for a peak-power $P_0 = 0.121$ W, simulated with both algorithms of the coarse-step method and the precomputed $M(\omega)$ matrices. The fibre had the same parameters as otherwise for the results shown in figure 9.5. The transmission is shown to improve as the pulse is
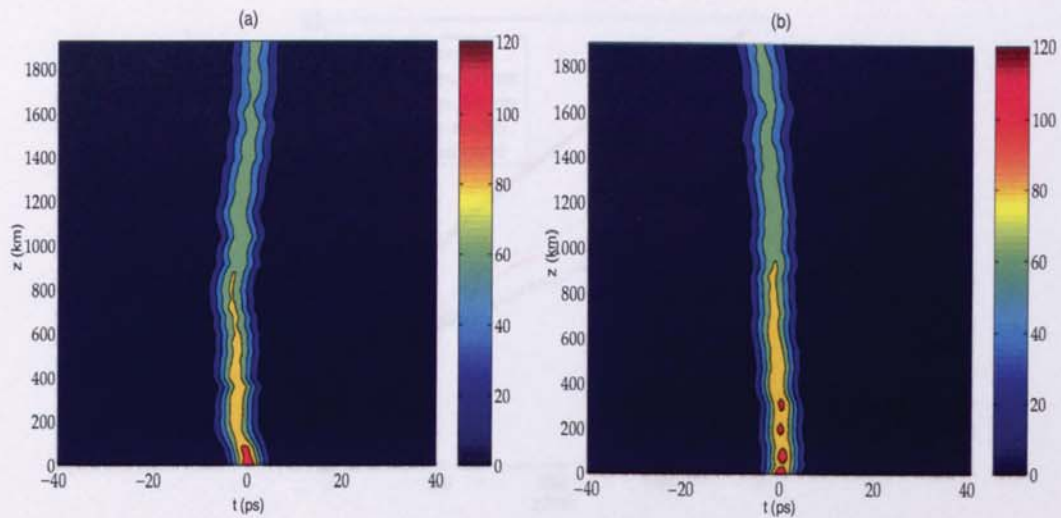
Figure 9.6: PMD transmission for a soliton of peak-power $P_0 = 0.121$ W, simulated using (a) the coarse-step method (b) the precomputed matrices of the Mananakov-PMD equation

shown to retain the intensity profile and not to disperse in comparison to Fig. 9.5(a), simultaneously the intensity levels remain on higher levels for a larger distance and the pulse does not break down as in Fig. 9.5(b). Rather the pulse will appear to jitter in the temporal domain as the two modes adjust their velocities continuously in order to remain bound together. However the soliton peak-power does drop as the soliton produces dispersive waves. To monitor the reduction of the PMD broadening due to soliton transmission, a Gaussian pulse of 10 mW peak-power is launched initially through a fibre of 2000 km with a $b' = 0.1$ ps/km, at this stage in this so called "linear case" only the PMD effect is included using the Manakov-PMD equation. Next a full soliton transmission is accomplished for the same fibre using a pulsewidth of $T_{fwhm} = 5$ ps, and for successive values of the GVD parameter $D = 0.2, 0.5, 1$ ps/nm/km. The results are shown in figure 9.7.

The numerical outcome of figure 9.7 indicates that indeed there is a reduction in the PMD broadening owing to the soliton effect. When the GVD parameter is small the PMD phenomenon is influencing greatly the transmission and can not be ignored as the curves for $D = 0.2, 0.5$ ps/nm/km reveal, as the DGD is large compared to the GVD. When the GVD is large ($D = 1$ ps/nm/km) the PMD can be treated as a perturbation and thus the reduction is even greater as further shown in Fig 9.7. In the same figure the common case of a Gaussian pulse suffering only from PMD ($b' = 0.1$ ps/km) is
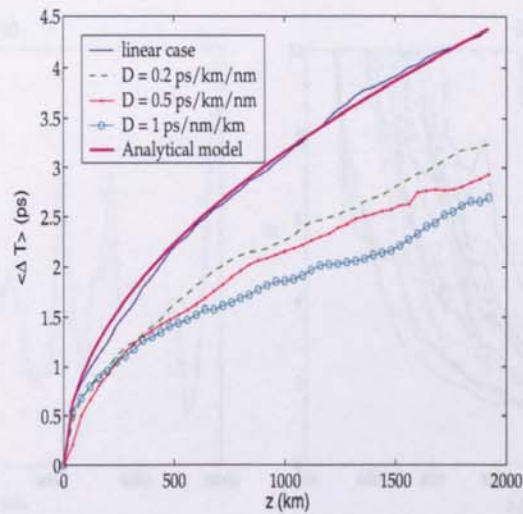
Figure 9.7: PMD broadening for a Gaussian pulse compared against the square-root of Eq. 3.30 and against the PMD broadening for soliton transmission

compared against the theoretical result for the long length regime of Eq. 3.30, which is labelled *Analytical model*. From this graph it is shown that all the soliton transmission results demonstrate a clear improvement compared to the case of the common non-soliton transmission (blue curve), as the curves presenting the broadening of the soliton pulses due to PMD produce a lower level of broadening for the same distance. Next the robustness of solitons with respect to PMD is investigated through the quality factor of different transmission systems. The Q-factor of a conventional soliton transmission system is monitored after launching a 10 Gbit/s bit-pattern through a fibre having a $D = 1$ ps/km/nm, $A_{eff} = 80\mu m^2$. The soliton signal was represented as a series of secant pulses with a resolution of 2^{11} points in a time window of 3200 ps with a number of bits of 2^5. It should be noted that in this case the ellipticity parameter $B = 1$ so that the Manakov soliton is obtained in a strict mathematical sense. In figure 9.8(a) the Q-factor of the system without PMD is shown. The Q-factor continues to be well above the limit of $Q = 6$ for over a distance of 10000 km. In contrast, in figure 9.8(b) and after PMD is added to the signal one finds that the soliton transmission is severely impaired and it falls below the limit-value of $Q = 6$ at the region of a distance of 1000 km even for a small value of $b' = 0.1$ ps/km. This reveals the significance of the PMD effect for a soliton link in general, as ultimately the Q-factor or equivalently the bit-error-rate of a system will characterise a link, as being efficient or inefficient for

transmission.
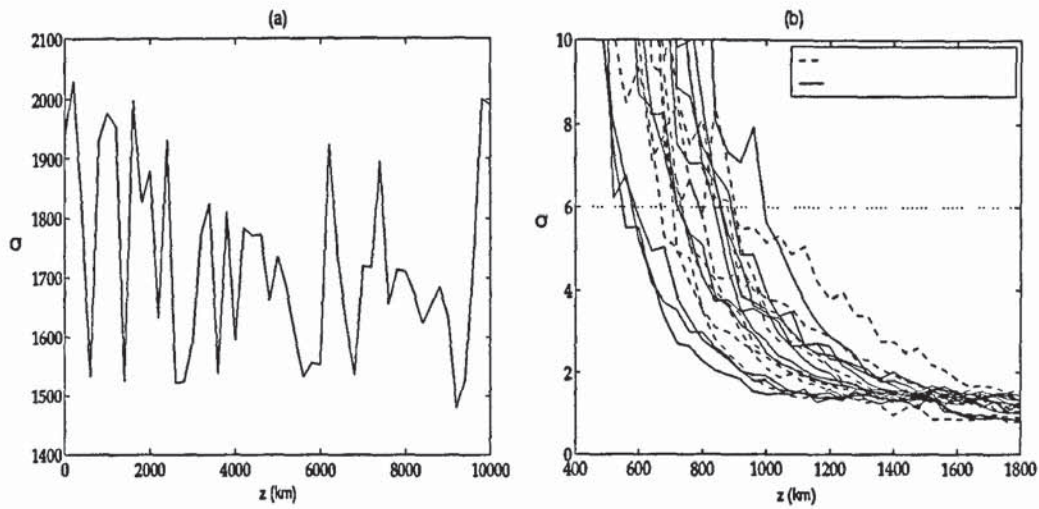
Figure 9.8: Q-factor for a soliton system (a) without PMD, (b) with a $b' = 0.1$ ps/km
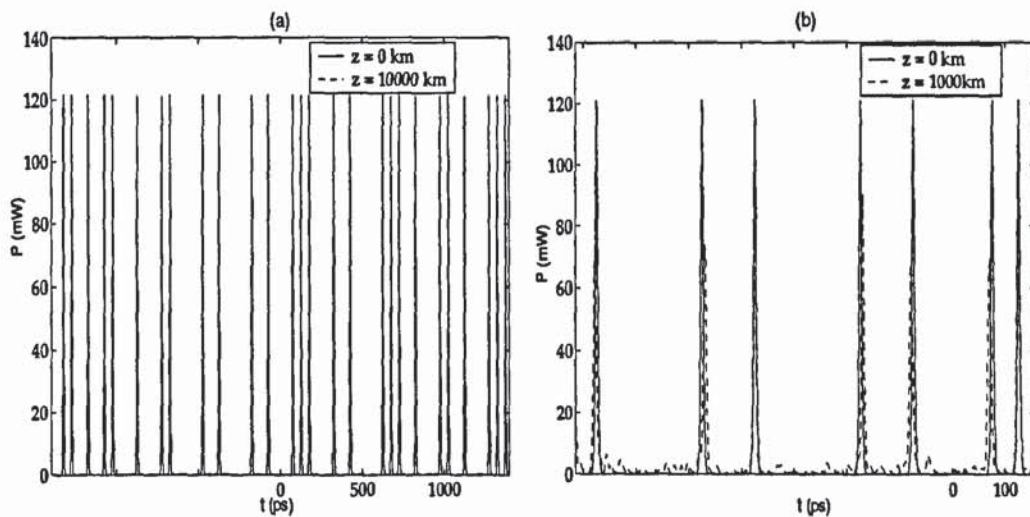
Figure 9.9: Bit-pattern of a soliton system (a) without PMD at the transmitter and
after a propagation distance of 10000 km, (b) with a $b' = 0.1$ ps/km at the transmitter
and after a propagation distance of 1000 km

The reason for the severe impairements caused by PMD are presented clearly in
figure 9.9. In Fig. 9.9(a) the soliton bit-pattern propagates error free for 10000 km.
In the second part for a shorter distance of 1000 km and focusing on a time window
between -700~100 ps (Fig. 9.9(b)) it is shown that the PMD effect causes the solitons
to produce dispersive waves that interfere with the adjacent bits giving errors and
simultaneously the "jitter" introduced by PMD as the two modes change their velocities

cause the Q-factor to drop dramatically.

We next simulate a soliton system with the dispersion map similar to [47] as shown
in figure 9.10 with the following characteristics. An input power of 26.4 mW and a
FWHM of 17.6 ps. A rectangular optical filter with 2 THz bandwidth is used in the
amplifier. The receiver includes another electrical filter of 20 GHz bandwidth. We used
a 10 Gbit/s bit-pattern simulated with 2^8 bits and a resolution of 2^{14} in a time window
of 25.6 ns. The fibre was an SMF fibre with a dispersion parameter of 1 ps/km/nm a
loss of 0.2 dB/km and an effective area $72\mu m^2$. The amplifier has a gain of 8 dB and
a noise-figure of 2.
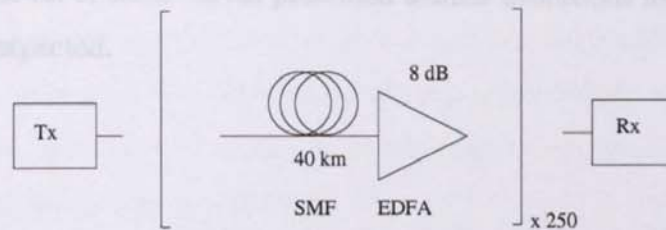
Figure 9.10: Soliton Transmission system
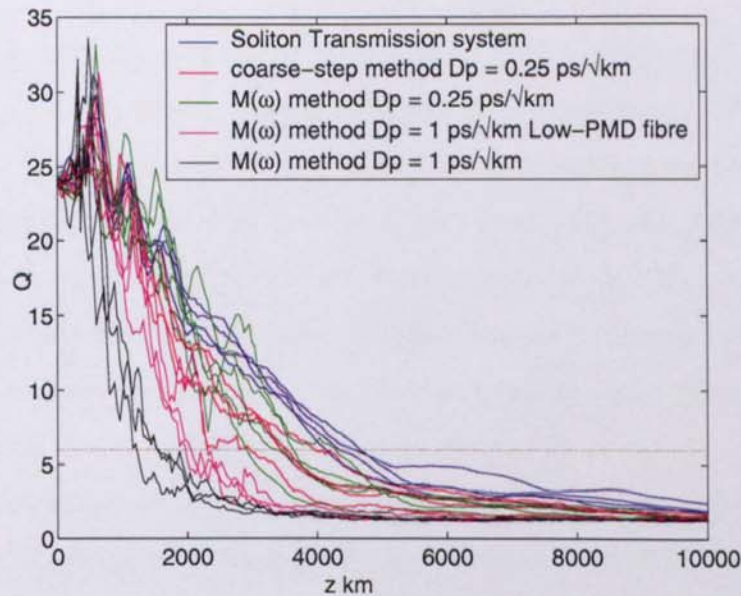
Figure 9.11: Q-factor performance for the soliton transmission system of Fig. 9.10
(blue line), using the coarse-step method with a $D_{PMD} = 0.25$ ps/$\sqrt{km}$ (red line),
using the M(ω) matrices for the same D_{PMD} value (green line), implementing low-PMD
fibres after increasing the D_{PMD} value to $D_{PMD} = 1$ ps/$\sqrt{km}$ (magenta) through the
Manakov-PMD matrices and using the M(ω) matrices for a $D_{PMD} = 1$ ps/$\sqrt{km}$ value
(black line)

The result for the Q-factor of such a system without PMD and for a constant $D_{PMD} = 0.25\text{ps/km}^{1/2}$, given by the coarse-step method, is shown in figure 9.11. In the same graph we also used the $M(\omega)$-matrices method for a $D_{PMD} = 0.25\text{ps/km}^{1/2}$ and $D_{PMD} = 1\text{ps/km}^{1/2}$ and continuously we introduced a fibre spin of 0.1 rad/m for the case of a $D_{PMD} = 1\text{ps/km}^{1/2}$, which as shown improved the Q-factor extending the transmission length. We otherwise produced the same result for [75].

It should be noted that the Q-factor of the system with the PMD given by the coarse-step method, was tested additionally for a varying D_{PMD}, uniformly and Gaussian distributed, with a width for the random distributions of 0.8 ps. The results of these tests have been grouped together with the standard coarse-step method approach (blue line), because all of these curves presented similar evolutions for the Q-factor, as it was otherwise expected.

Chapter 10

Conclusion

The fibre optic technology is considered to be a promising option for the global mesh of communication networks. The advantages of such a technology, as outlined in the introduction of this thesis include a huge bandwidth capability, low signal attenuation, low dispersion, and low power requirements.

From a financial point of view, a large amount of funds, have been directed from several telecommunications companies for the fabrication and installation of optical fibre links.

There is large amount of these links that have been implemented in the earlier days of optical communications and for lower bit rate requirements. For these links to accommodate higher rates and more sophisticated systems, need to be upgraded in order to eliminate the potential problems that arise. For that to happen either complete new systems or individual links have to be installed or high cost maintenance will have to be arranged in predetermined periods of time or on demand when a problem appears. Both of these methods are very expensive, which also reflects on the price that the individual customer will have to pay to the service provider.

A third option would be to resolve outstanding issues, through numerical simulations, which would then give accurate description of the problem and reveal the outages that might occur, for various problems. It is obvious from the above that the improvement in terms of physical accuracy, and numerical efficiency of the numerical solvers is imminent.

The aim of this thesis is that exactly, of providing computationally optimized, and

physically adequate numerical solvers for the description of the optical phenomenon of PMD that arises for higher bit rates and thus shorter time slots.

In the following paragraphs of this section an expanded index of the thesis is provided, which will present a commentary and also conclusions based on the work performed in every chapter.

In chapter 1 a historical perspective of the evolution of the optical telecommunications network was given. The obstacles that arose during the growth of the optical network were mentioned in a chronological order along with a brief description of each effect. The various ways that these problems were resolved or on the other hand the methods to utilise the phenomena, to produce a positive outcome, such as using the GVD and the nonlinearity to produce the soliton pulse, were outlined. The aim of the development of this section was to eventually introduce the PMD and the reasons behind the application of numerical methods to represent this effect, which is also the aim of this work.

Chapter 2 provides the derivation of the NLS equation and the generalisation to the CNLS. The effects that were defined briefly in chapter 1 are here identified as the terms of the NLS and the CNLS equations, namely the losses, the dispersion and nonlinearity and also the PMD effect. The derivation and description of these two relations was necessary as in the process of this research it was essential to implement the numerical solvers of the scalar and vector approximations. This due to the fact that any model of PMD will have to be included into these two equations for the description of more realistic systems subjected to PMD. Further in this chapter the limited cases for all of these effects were given, with theoretical and numerical evidence. The term "limited case", is defined as the situation where only one effect is present in a transmission link while the rest have been numerically set to zero through the different parameters and the aim for this kind of simulations is to identify if the system is responding according to well known theoretical solutions. On the other hand one of the aims of this project is to analyse any potential differences that might arise from the use of the vector instead of the widely used scalar model. Such a comparison has not been presented thoroughly and systematically in other sources.

Chapter 3 reviews the different elements of polarisation mode dispersion theory. In

more detail the different factors that contribute to the effect are the modal birefringence and the power coupling between the two modes. Moreover a detailed mathematical description of light is incorporated. Then based on that, the Poincaré sphere representation is explained. This is essential for further understanding, as later in this thesis a number of simulations and the representation of their results, on the Poincaré sphere are given. Equally important is the mathematical derivation of the spreading due to PMD as this is the element that has been used widely to describe the phenomenon in the short and long length regime and also used in this thesis to compare against, the numerical results for the spreading of a pulse due to PMD. The derivation follows the same steps of known references which are aknowledged. Last the stochastic models that are used to characterise links and PMD emulators are presented and explained, as the same models are used in this and a number of other projects to characterise a numerical simulator.

In chapter 4 a detailed account of the numerical method of the coarse-step method is given. This method is represented by the theory of the CNLS equation which introduces the delay developing between the two modes and the inclusion of power coupling through the multiplication of the modes with a rotation matrix. The mixing that the coupling introduces is shown with the help of the Poincaré sphere, where the scattering of a single polarisation state is monitored. Simultaneously through the Poincaré sphere coordinates the mixing is calculated for different steps. The purpose of this test is to identify the number of steps needed and the rate that the mixing occurs. For the rotation matrices this is found indeed to happen very fast. The same tests take place for the complete method that includes the splitting of the two modes, where it is found that a uniform mixing will result in a number of $8 \sim 12$ steps. Next the theoretical derivation of the rescaling, depended on the step size, that the method introduces is given, which is then demonstrated through the numerical simulation and the comparison with the theoretical model.

Chapter 5 describes the numerical method resulting from the Manakov-PMD equation. The theoretical derivation of the method is outlined. Through the evidence provided it is suggested that the Manakov-PMD method can be numerically effective, by precalculating a number of transfer matrices resulting from this method instead of

calculating this matrix at every step. Moreover the mixing on the Poincaré sphere, as previously shown for the coarse-step method is produced, for different number of matrices, and different number of steps. This of course concludes that for the case of calculating a matrix at every run there is a complete mixing but also here it is shown that for a smaller number of steps than the coarse-step method and by using the precomputed matrices approach it is possible to achieve a satisfactory mixing on the Poincaré sphere. Further the spreading of the pulse which results by using the Manakov-PMD equation is given and shown to always follow the theoretical model irrespectively of the size of the step used in the numerical implementation.

Chapter 6 is concerned with the statistical comparison of both methods which is essential to define if they agree with the theory behind emulation. The probability distribution function and the autocorrelation function of the coarse-step method and the Manakov-PMD matrices is numerically produced and compared with the theoretical models widely used in emulation. The motivation for this comparison is to specify the exact length over which each of the two methods will converge to the appropriate model. The Manakov-PMD equation matrices method is shown to converge much faster than the coarse-step method. Although both of these algorithms are adequate for the representation of the PMD in the long-length regime it is preferable to choose the method which will cover physically accurately all the cases including the short length regime, that is the Manakov-PMD equation which otherwise does not inherently suffer from the rescaling problem of the coarse-step method. The second and more important conclusion is that these results allow for the numerical optimisation of the Manakov-PMD method through the precomputed matrices approach. That is, even in the case where one chooses to use a number of matrices which will be equal to 4 and for a number of steps equal to 4 the PDF and the ACF converge to the required theoretical models.

In chapter 7 the focus was mainly on the artifacts that are produced in the autocorrelation function of the coarse-step method. These artifacts become evident as side harmonics appear in the ACF that are a product of a numerical property of the coarse-step method. In other words the first-order PMD remains constant from step to step and thus as the delay between the two modes is introduced by the CNLS through

the first order PMD term, side-peaks appear in the values of frequency multiples of π. This is a direct outcome of the fact that a constant DGD per length multiplies the different frequency bins in the numerical implementation at every step. This problem, which has been shown to appear with respect to emulators has not been fully resolved in terms of numerical simulators. The problem is solved by introducing a different DGD from step to step and thus randomising the location that these peaks appear in the frequency spectrum. For a large number of values and a large number of steps the peaks disappear altogether. However another step is taken so that the algorithm is further numerically optimized and that is accomplished, by noticing that the peaks appear in larger frequency intervals even by choosing only between a number of values ranging from $2 \sim 4$. Thus instead of implementing a uniform or Gaussian distribution of certain range and calculating a value at every step, one chooses only between 2 or 4 values. This additively results in reducing the overall time of computation in simulations such as calculating the PDF and the ACF in order to approach the theoretical model of PMD, as simulated in chapter 6.

Chapter 8 provides an algorithm for reducing the PMD of a fibre. This algorithm is basically the Manakov-PMD matrices approximation, with a modification. That is adding a mathematical mean to the distribution which represents the angular evolution of the fibre for the Manakov-PMD equation. For the first time thus it is evident that low-PMD spun fibres can be simulated numerically through the Manakov-PMD equation. These fibres are experimentally produced by adding an artificial spin in the drawing process which effectively masks the perturbation of the birefringence and forces the two modes to couple faster. This is essentially what the modified Manakov-PMD matrices represent.

In chapter 9 the different methods are combined to produce realistic communication systems. The different algorithms for implementing PMD are incorporated into the CNLS equation. The chapter then focuses on the two main issues of optical·transmission, first the linear transmission and second the soliton transmission. The linear system was implemented by choosing NRZ format for the signal at a low power level. The transmission system was implemented using a symmetric map of 20 km of DCF added between two 10 km segments of SMF, so that the GVD was compensated. The

losses of the fibre were reduced by an amplifier which in turn introduced noise. Through the filtering, that follows the amplifier, the majority of the noise content is removed and thus the only remaining effect is the nonlinearity accumulated in a long distance. The PMD that is added next through all of the algorithms mentioned earlier results in the deterioration of the quality of the system but not significantly due to the low-value of this $(0.1 \, ps/\sqrt{km})$. For an increased DGD value the penalties are severe but there is also improvement through the modified Manakov-PMD algorithm for low-PMD spun fibre. The soliton case is really interesting as it puts the soliton-trapping phenomenon to the test. Indeed this is demonstrated in this thesis for a constant DGD. When we include the complete model the picture changes significantly and we find that the dispersive waves deteriorate the Q-factor tremendously.

Last it is important to mentioned a few subjects that are of particular interest, have been brought forward during the course of this project and should be considered as areas of future work. First is the extremely complex task of PMD compensation techniques. As of this moment there has not been an effective way of compensating the PMD phenomenon on a fibre with random DGD sections. This would require the calculation of a mirror image of the transmission link that would be implemented in the receiver with polarisers and delay elements. This is an excellent task for numerical implementations as the experimental aspect of it could be costly, more complex, and time consuming. In contrast the numerical solvers can be optimized and transformed much faster and then the final solution can be translated into an experimental method. Another area of future work should be soliton transmission, interaction with PMD and compensation. There has been an effort nowadays to compensate for the dispersive waves produced by PMD on a soliton transmission as this is speculated to be the major source of penalties in such transmission, since the soliton pulses maintain their pulsewidth. This is attempted through filtering. However through our simulations it is evident that the quality factor reduces because of the reduction of the peak power of the pulse. It would be much easier then to use a nonlinear optical loop mirror (NOLM) to compensate for this loss and simultaneously suppress the dispersive waves as this element can produce the required transfer function to achieve such an effect. Finally the outstanding issue on the side of multichannel transmission and interaction with

PMD should be mentioned, which would be accomplished by numerically implementing elements such as WDM multiplexers and demultiplexers so that the PMD effect in realistic multichannel transmission is monitored.

Appendix A

Split-step Fourier method

The algorithm used to solve the CNLS and the NLS equation in this thesis, is the commonly used split-step Fourier approach. The theory behind the implementation of the split-step Fourier method is based on dividing the evolution of the field into a linear and a nonlinear part. Then splitting the transmission path along the fibre into small segments one calculates the two parts, the linear and the nonlinear separately.

It would suffice demonstrating the method for the NLS equation, since the CNLS differs only due to the fact that the split-step Fourier method has to be applied to each one of the two propagation modes separately, and thus be calculated twice. So starting from the NLS,

$$i\left(\frac{\partial E}{\partial z} + \beta'\frac{\partial E}{\partial t}\right) - \frac{\beta''}{2}\frac{\partial^2 E}{\partial t^2} + \gamma(|E|^2)E + \frac{ia}{2}E = 0 \qquad (A.1)$$

one writes then for the field,

$$\frac{\partial E}{\partial z} = (\hat{D} + \hat{N})E \qquad (A.2)$$

With $\hat{D}, \hat{N}$, the linear and the nonlinear part of the NLS respectively. Solving this one finds,

$$E(z + \Delta z, t) = \exp((\hat{D} + \hat{N})\Delta z)E(z,t) \qquad (A.3)$$

with the $\hat{D}$ operator for the linear part

$$\hat{D} = -i\frac{\beta''}{2}\frac{\partial^2}{\partial t^2} - \frac{a}{2} \tag{A.4}$$

and the $\hat{N}$ for the nonlinear part given by,

$$\hat{N} = i\gamma(|E|^2) \tag{A.5}$$

applying the split-step Fourier method on this result implies that

$$E(z + \Delta z, t) \approx \exp(\hat{D}\Delta z)\exp(\hat{N}\Delta z)E(z, t) \tag{A.6}$$

where the linear operator can be solved in the frequency domain while the nonlinear operator in the time domain, one then Fourier transforms Eq. A.4,

$$\hat{D} = i\omega^2 - \frac{a}{2} \tag{A.7}$$

the strategy behind using this method is summarised in this step as one can evaluate the two effects differently, the linear in the frequency domain and the nonlinear in the time domain, and thus employ the FFTW [104]-[113] package to Fourier transform from one to the other domain, which makes the overall computation extremely fast and gives the opportunity to the programmer to skip the partial derivatives resulting from the linear operator.

The overall computation accuracy can be improved if one uses the so called symmetrized split-step Fourier method which is more specifically used in this work. Using this method Eq. A.6 transforms to,

$$E(z + \Delta z, t) \approx \exp(\hat{D}\Delta z/2)\exp(\hat{N}\Delta z)\exp(\hat{D}\Delta z/2)E(z, t) \tag{A.8}$$

In more detail instead of setting say $\hat{D} = 0$ and computing the full step of the nonlinear operator and then setting $\hat{N} = 0$ and calculating the action of the full step of dispersion, with Eq. A.8 the nonlinearity is included in the middle of the simulation step. So numerically one calculates the first half of the linear step then one full nonlinear step and then the second half of the linear step.

This physically takes advantage of the slow nonlinear effect which effectively will

be accumulated additively through the step and become important later on in the transmission. The proof for the accuracy improvement of the transmission simulation is given mathematically as follows. For two operators such as $\hat{D}$ and $\hat{N}$ in general through the Baker-Hausdorff formula,

$$\exp(\hat{D} + \hat{N}) = \exp(\hat{D} + \hat{N} + \frac{1}{2}[\hat{D}, \hat{N}] + \frac{1}{12}[\hat{D} - \hat{N}, [\hat{D}, \hat{N}]] + ...) \qquad (A.9)$$

if the operators commute then $[\hat{D}, \hat{N}] = \hat{D}\hat{N} - \hat{N}\hat{D} = 0$ which would mean that they operate on a common set of eigenfunctions. However from theory in this case the operators $\hat{D}, \hat{N}$ are non-commuting thus $\exp((\hat{D} + \hat{N})\Delta z) \approx \exp(\hat{D}\Delta z)\exp(\hat{N}\Delta z)$. The general formula is then actually given by,

$$\exp(\Delta z(\hat{D} + \hat{N})) = \exp(\Delta z\hat{D} + \Delta z\hat{N} + \Delta z^2 \frac{1}{2}[\hat{D}, \hat{N}] + \Delta z^3 \frac{1}{12}[\hat{D} - \hat{N}, [\hat{D}, \hat{N}]] + ...) \quad (A.10)$$

It is obvious then that the split-step Fourier transform given by Eq. A.6 will approximate the expansion of A.10 and have a difference of up to the second order of Δz from the correct result which can be indicated as $O(\Delta z^2)$.

On the other hand if one expands Eq. A.8 this can be done in two steps, first the product $\exp(\hat{D}\Delta z/2)\exp(\hat{N}\Delta z)$ is expanded,

$$\exp(\hat{D}\Delta z/2)\exp(\hat{N}\Delta z) = \exp(\frac{\Delta z}{2}\hat{D} + \Delta z\hat{N} + \Delta z^2 \frac{1}{4}[\hat{D}, \hat{N}] + \Delta z^3 \frac{1}{24}[\frac{1}{2}\hat{D} - \hat{N}, [\hat{D}, \hat{N}]] + ...)$$
$$(A.11)$$

and for the second step, one computes the same formula by including the second term of $\exp(\hat{D}\Delta z/2)$,

$$\begin{aligned}
&\exp(\hat{D}\Delta z/2)\exp(\hat{N}\Delta z)\exp(\hat{D}\Delta z/2) \\
&= \exp(\frac{\Delta z}{2}\hat{D} + \Delta z\hat{N} + \Delta z^2 \frac{1}{4}[\hat{D}, \hat{N}] + \Delta z^3 \frac{1}{24}[\frac{1}{2}\hat{D} - \hat{N}, [\hat{D}, \hat{N}]] + ...)\exp(\hat{D}\Delta z/2) \\
&= \exp(\frac{\Delta z}{2}\hat{D} + \frac{\Delta z}{2}\hat{D} + \Delta z\hat{N} + \Delta z^3 \frac{1}{8}[[\hat{D}, \hat{N}], \hat{D}] + ...) \qquad (A.12)
\end{aligned}$$

It is clear from Eq. A.12 that mathematically this method produces a smaller difference of the third order to the step-size $O(\Delta z^3)$. So that it enables the numerical implementation to be more accurate and being then the method of choice for solving both the NLS and the CNLS equation.

Appendix B

Important differential equations and their solutions

In this appendix the several differential equations that are met throughout the text will be analytically solved, as in the main thesis only the final results were presented.

The Stochastic differential equation for the PMD vector

In chapter 3, the following differential equation was presented,

$$
\frac{d\Omega}{dz} = -\sigma \begin{pmatrix} 0 & -\Omega_3(l,\omega) & \Omega_2(l,\omega) \\ \Omega_3(l,\omega) & 0 & -\Omega_1(l,\omega) \\ -\Omega_2(l,\omega) & \Omega_1(l,\omega) & 0 \end{pmatrix} \Delta W - \begin{pmatrix} \sigma^2 & 0 & 0 \\ 0 & \sigma^2 & -\Delta\beta \\ 0 & \Delta\beta & \sigma^2 \end{pmatrix} \Omega
$$
$$
+ \begin{pmatrix} \Delta\beta' \\ 0 \\ 0 \end{pmatrix} \tag{B.1}
$$

this equation is related directly with the theory of stochastic differential equations [114]-[117], which is summarised in the following expression,

$$\frac{df(z)}{dz} = g(f(z))v(z) + u(f(z)) \qquad \text{(B.2)}$$

where $f(z)$ is an m-dimensional vector, $v(z)$ is again m-dimensional and a white noise process such as the parameter ΔW in Eq. B.1, which is chosen from a uniform distribution, $g(f(z))$ represents an $m \times m$ matrix,

$$-\sigma \begin{pmatrix} 0 & -\Omega_3(l,\omega) & \Omega_2(l,\omega) \\ \Omega_3(l,\omega) & 0 & -\Omega_1(l,\omega) \\ -\Omega_2(l,\omega) & \Omega_1(l,\omega) & 0 \end{pmatrix} \qquad \text{(B.3)}$$

and finally $u(f(z))$ will be another m-dimensional vector and in this case given by,

$$\begin{pmatrix} -\sigma^2\Omega_1(l,\omega) + \Delta\beta' \\ -\sigma^2\Omega_2(l,\omega) + \Delta\beta\Omega_3(l,\omega) \\ -\Delta\beta\Omega_2(l,\omega) - \sigma^2\Omega_3(l,\omega) \end{pmatrix} \qquad \text{(B.4)}$$

from the theory of stochastic differential equations any function F of the variable Ω will obey the rule

$$\frac{d<F>}{dz} = <G(F)> \qquad \text{(B.5)}$$

the generator G will be given from the general formula

$$G = \frac{1}{2}\sum_{j=1}^{m}\sum_{i=1}^{m} g(f(z))g(f(z))^T \frac{\partial^2}{\partial f(z)_i \partial f(z)_j} + \sum_{k=1}^{m} u(f(z)) \qquad \text{(B.6)}$$

where the superscript T denotes transpose so plugging Eq. B.3 into $g(z)$ and Eq. B.4 into $u(f(z))$ and substituting the $f(z)$ with the Ω vector one finds the generator to be equal to Eq. 3.25.

The first order differential equation of the PMD broadening

Deriving the DGD quantity from the stochastic differential equation generator G given by Eq. 3.25 as follows,

$$\frac{d<\Delta T^2>}{dz} =<G(\Omega_1^2 + \Omega_2^2 + \Omega_3^2)> \qquad (B.7)$$

after the application of the generator on $(\Omega_1^2 + \Omega_2^2 + \Omega_3^2)$ this results in the expression,

$$\frac{d<\Delta T^2>}{dz} = 2\Delta\beta' <\Omega_1> \qquad (B.8)$$

In order to define this the quantity $<\Omega_1>$ must be defined by applying the same generator operator on Ω_1, thus

$$\frac{d<\Omega_1>}{dz} =<G(\Omega_1)>$$
$$\frac{d<\Omega_1>}{dz} = -\sigma^2 <\Omega_1> +\Delta\beta' \qquad (B.9)$$

this is solved by using an integrating factor $\exp(\sigma^2 z)$,

$$\exp(\sigma^2 z)\frac{d<\Omega_1>}{dz} + \sigma^2 \exp(\sigma^2 z) <\Omega_1 >= \exp(\sigma^2 z)\Delta\beta' \qquad (B.10)$$
$$<\Omega_1 >= \frac{\Delta\beta'}{\sigma^2} + \frac{c\Delta\beta'}{\exp(\sigma^2 z)\sigma^2} \qquad (B.11)$$

and by setting the initial condition so that at $z = 0$, $\Delta T^2(0) = \Omega_1^2(0) + \Omega_2^2(0) + \Omega_3^2(0) = 0$ then $<\Omega_1 >= 0$, we find the constant $c = -1$. Then returning in Eq. B.10 this implies that,

$$< \Omega_1 >= \frac{\Delta \beta'}{\sigma^2}(1 - \exp(-\sigma^2 z)) \tag{B.12}$$

substituting this into Eq. B.7 gives,

$$\frac{d < \Delta T^2 >}{dz} = 2\frac{\Delta \beta'^2}{\sigma^4}(\sigma^2 - \sigma^2 \exp(-\sigma^2 z)) \tag{B.13}$$

by straight forward integration this will result in,

$$< \Delta T^2 >= 2\frac{\Delta \beta'^2}{\sigma^4}(\sigma^2 z + \exp(-\sigma^2 z) + c) \tag{B.14}$$

and using the same initial condition as before which is $\Delta T^2(0) = 0$ we find the constant of integration to be $c = -1$ thus the final result concludes,

$$< \Delta T^2 >= 2\frac{\Delta \beta'^2}{\sigma^4}(\sigma^2 z + \exp(-\sigma^2 z) - 1) \tag{B.15}$$

The $M(\omega)$ matrix derivation

Returning to chapter 5 we recall the first order differential equation [118]-[121] whose solution are the $M(\omega)$ matrices,

$$i\frac{\partial M(z,\omega)}{\partial z} + (b + b'\omega)\Sigma(z)M(z,\omega) = 0 \tag{B.16}$$

then by integrating this expression one finds,

$$M(z,\omega) = \exp\left(\int i(b + b'\omega)\Sigma(z)dz\right)M(0,\omega) \tag{B.17}$$

with the initial condition that

$$M(0,\omega) = I = \begin{pmatrix} 1 & 0 \\ 0 & 1 \end{pmatrix} \tag{B.18}$$

In order to focus on a shorter length scale the factor $\exp\left(\int i(b + b'\omega)\Sigma(z)dz\right)$ is approximated as $\exp\left(i(b + b'\omega)\Sigma(z)\delta z\right)$ where the integral over the distance which results in a larger length accumulation is approximated by δz. Further this factor can be written by the exponential series expansion as,

$$
\begin{aligned}
\exp\left(i(b + b'\omega)\Sigma(z)\delta z\right) &= \sum_{n=0}^{\infty} \frac{(-1)^n\left((b + b'\omega)\Sigma(z)\right)^{2n}(\delta z)^{2n}}{2n!} \\
&+ i\sum_{n=0}^{\infty} \frac{(-1)^n\left((b + b'\omega)\Sigma(z)\right)^{2n+1}(\delta z)^{2n+1}}{2n + 1!}
\end{aligned} \tag{B.19}
$$

this is further simplified by noticing that,

$$\Sigma(z)^{2n} = (\Sigma(z)^2)^n = I \quad \text{and} \quad \Sigma(z)^{2n+1} = (\Sigma(z)^2)^n\Sigma(z) = \Sigma(z) \tag{B.20}$$

and thus further substituting this into Eq. B.19,

$$
\begin{aligned}
\exp\left(i(b + b'\omega)\Sigma(z)\delta z\right) &= \sum_{n=0}^{\infty} \frac{(-1)^n\left((b + b'\omega)\right)^{2n}I(\delta z)^{2n}}{2n!} \\
&+ i\sum_{n=0}^{\infty} \frac{(-1)^n\left((b + b'\omega)\right)^{2n+1}\Sigma(z)(\delta z)^{2n+1}}{2n + 1!}
\end{aligned} \tag{B.21}
$$

so the final relation for the $m(z, \omega)$ matrices is,

$$m_j(\omega) = m(z, \omega) = \cos((b + b'\omega)\delta z)I + i\sin((b + b'\omega)\delta z)\Sigma(z) \tag{B.22}$$

while finally by accumulating a long chain of these transfer elements results in a series of multiplications which gives,

$$M(z,\omega) = \prod_{j=0}^{L} m_j(\omega) \tag{B.23}$$

where L is the total length of the coarse-step of the simulation in the order of kilometres.

Appendix C

A geometrical derivation of the PMD vector

From the two polarisations of the signal the three normalised Stokes vectors are derived as in Eq. 6.4. In order to define numerically the PMD vector, the three coordinates are needed as well as the modulus of the vector. In order to find the three directions the starting point is the expression,

$$e_\Omega(l,\omega) = \frac{\Delta_-(l,\omega) \times \Delta_+(l,\omega)}{|\Delta_-(l,\omega) \times \Delta_+(l,\omega)|} \qquad (C.1)$$

where the unit vector of the PMD directions $e_\Omega = (e_1, e_2, e_3)^T$, this vector will always be vertical to the differences of the Stokes parameters vectors, that is,

$$\Delta_-(l,\omega) = s(l,\omega) - s(l,\omega - \Delta\omega) \qquad (C.2)$$
$$\Delta_+(l,\omega) = s(l,\omega + \Delta\omega) - s(l,\omega)$$

Where the $\Delta_-(z,\omega)$ and $\Delta_+(z,\omega)$ the two difference vectors, provided that the difference $\Delta\omega$ is small compared to the bandwidth of the simulation, the PMD vector will be perpendicular on the surface defined by the two differences, between the $s(\omega)$ vector and the two vectors $s(\omega + \Delta\omega)$ and $s(\omega - \Delta\omega)$. Thus the cross-product in return will define the direction of the vector as in Eq. C.1.

This is graphically represented in Fig. C.1, where the PMD vector Ω is perpendicular to the closed trajectory defined by the two differences.
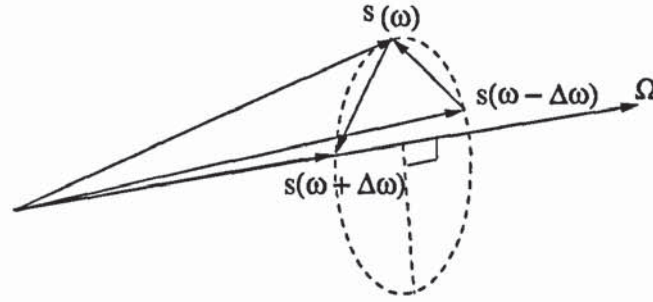
Figure C.1: PMD vector direction

What follows next is the calculation of the angle θ between the Stokes vector and the PMD vector,

$$\mathbf{s}(l,\omega) \cdot \mathbf{e}_\Omega(l,\omega) = |\mathbf{e}_\Omega(l,\omega)||\mathbf{s}(l,\omega)| \cos\theta \qquad (C.3)$$

but since both the normalised stokes vectors and the vector of the direction of PMD have $|\mathbf{e}_\Omega(l,\omega)| = |\mathbf{s}(l,\omega)| = 1$, then

$$\cos\theta = \mathbf{e}_{x\Omega}(l,\omega)\mathbf{s}_x(l,\omega) + \mathbf{e}_{y\Omega}(l,\omega)\mathbf{s}_y(l,\omega) + \mathbf{s}_z(l,\omega)\mathbf{e}_{z\Omega}(l,\omega) \qquad (C.4)$$

defining the angle it is then possible to move on to the modulus of the PMD vector from the defining expression of

$$\frac{d\mathbf{s}(l,\omega)}{d\omega} = \Omega(l,\omega) \times \mathbf{s}(l,\omega) \qquad (C.5)$$

one replaces the dot-product and as for Eq. C.3 the modulus of the Stokes-vector $|\mathbf{s}(l,\omega)| = 1$, then

$$|\Omega| = \frac{1}{sin(\theta)} \left| \frac{d\mathbf{s}(l,\omega)}{d\omega} \right| \qquad (C.6)$$

and finally by substituting the derivative by the length between the vectors $s(\omega + \Delta\omega)$, $s(\omega)$ plus the length between $s(\omega - \Delta\omega)$, $s(\omega)$, which will be given by the sum of the two angles $\arccos(\mathbf{s}(z,\omega + \Delta\omega) \cdot \mathbf{s}(z,\omega))$ and $\arccos(\mathbf{s}(z,\omega) \cdot \mathbf{s}(z,\omega - \Delta\omega))$ the final equation is given as follows.

$$|\Omega| = \frac{1}{\sqrt{1 - cos^2(\theta)}} \left| \frac{ds(l,\omega)}{d\omega} \right| = \qquad (C.7)$$

$$\frac{\arccos(s(l,\omega + \Delta\omega) \cdot s(l,\omega)) + \arccos(s(l,\omega) \cdot s(l,\omega - \delta\omega))}{2\Delta\omega\sqrt{(1 - cos^2(\theta))}}$$

List of publications

1. M. Eberhard and C. Braimiotis, Numerical implementation of the Manakov-PMD equation with precomputed M(w) matrices, In Techn. Digest Series, Conference on Nonlinear Guided Waves and Their Applications (NLGW), page MC3, Toronto, Canada, March 2004, Optical Society of America

2. C. Braimiotis and M. Eberhard, Numerical implementation of the coarse step method with a varying differential group delay, Proc. of Conference on Optical Networks and Technologies (OpNeTec), page 530-534, Pisa, Italy, October 2004, Consorzio Nazionale Interuniversitario per le Telecomunicazioni (CNIT)

3. Braimiotis and M. Eberhard, Numerical implementation of low-PMD spun fibres with precomputed M(w) matrices, Proc. on Postgraduate Research Conference in Electronics, Photonics, Communications and Networks, and Computing Science (PREP), page 100-101, Lancaster, UK, March 2005, University of Lancaster

4. C. Braimiotis and M. Eberhard, Application of the Manakov-PMD equation to a computational investigation of low-PMD fibres, Techn. Digest Series, Conference on Nonlinear Guided Waves and Their Applications (NLGW), page ThB8, Dresden, Germany, September 2005, Optical Society of America

5. C. Braimiotis, M. Eberhard and K. Blow, "Polarisation mode dispersion correlations with the coarse-step method", Opt. Comm. 262, pp. 135-139, 2006

References

[1] Govind P. Agrawal, "FIBRE OPTIC COMMUNICATION SYSTEMS", John Wiley & Sons Inc., New York (1997), Second Edition.

[2] F.P.Kapron,D.B.Keck and R.D Maurer, "Radiation losses in glass optical waveguides", Appl. Phys. Lett, vol. 17, pp. 423 - 425 (1970)

[3] T.Miya, Y.Terununa, T.Hosaka and T.Miyashita,"Ultimate low-loss single-mode fibre at 1.55 m", Electron.Lett,vol. 15, pp. 106-108 (1979).

[4] S. B. Poole, D. N. Payne, R. J. Mears, M. E. Fermann and R. I. Laming, "Fabrication and characterization of low-loss optical fibers containing rare-earth ions", J. Lightwave Technol., vol. 4, pp. 870-876, (1986).

[5] C. Lin, H. Kogelnik, and L. G. Cohen, "Optical-pulse equalization of low-dispersion transmission in single-mode fibers in the 1.3-1.7-mu-m spectral region" Opt. Lett.,vol. 5, pp. 476-478 (1980).

[6] Govind P. Agrawal, "NONLINEAR FIBER OPTICS", Academic Press, (2001), Third Edition.

[7] Shen, Y. R., "The principles of nonlinear optics", John Wiley & Sons ,New York (1984)

[8] M.J.O'Mahoney, Simeonidou D., Yu A. Zhou, "The design of a European optical network", J. of Lightwave Technol., Vol 13, pp. 817 - 828,(1979)

[9] A. Hasegawa and F. Tappert, "Transmission of Stationary Nonlinear Optical

Physics in Dispersive Dielectric Fibers I: Anomalous Dispersion," Appl. Phys. Lett., Vol. 23, pp. 142-144, (1973)

[10] R. W.Tkach, A. R.Chraplyvy, F.Forghieri, A. H.Gnauck, and R. M.Derosier, "Four photon mixing and high speed WDM systems,J. Lightwave Technol., vol. 13, pp. 841-849, (1995)

[11] W. Zeiler, F. Di Pasquale, P. Bayvel and J.E. Midwinter,"Modeling of four-wave mixing and gain peaking in amplified WDM optical communication systems and networks", J. of Lightwave Technol., vol 14, pp. 1933-1942,(1996)

[12] C. Kurtzke, "Suppression of fiber nonlinearities by appropriate dispersion management" IEEE Photon. Technol. Lett., vol. 5, pp. 1250-1253, (1993)

[13] B. Jopson and A. Gnauck, "Dispersion compensation for optical fiber systems", IEEE Commun. Mag., vol. 33, pp. 96-102,(1995)

[14] L.F. Mollenauer, R.H. Stolen, and J.P. Gordon, "Experimental Observation of Picosecond Pulse Narrowing and Solitons in Optical Fibers," Phys. Rev. Letters, Vol. 45, pp. 1095, (1980)

[15] Akira Hasegawa and Frederick Tappert, "Transmission of stationary nonlinear optical pulses in dispersive dielectric fibers. II. Normal dispersion" ,Appl. Phys. Lett.,vol. 23, pp. 171 , (1973)

[16] L. Mollenauer and R. Stolen, "Soliton laser," Opt. Lett.,vol 9, pp. 13, (1984)

[17] A.S. Gouveia-Neto, A.S.L. Gomes and J. R. Taylor, "Soliton Raman fibre ring oscillators" Opt. & Quantum Electron,vol. 20, pp. 165 (1988)

[18] K.J.Blow and N.J.Doran, "High Bit Rate Communications Systems using Non-Linear Effects", Optics Commun., vol. 42 ,pp. 403-406 (1982)

[19] N.J.Doran and K.J.Blow, "Solitons in Optical Communications", IEEE. J. Quantum Electronics,vol. 19,pp. 1883-1888, (1983)

[20] K.J.Blow and N.J.Doran, "Multiple Dark Soliton Solutions of the Nonlinear Schrodinger Equation", Physics Letters A, vol.107,pp. 55-58, (1985)

[21] W. Zhao, E. Bourkoff, "Propagation properties of dark solitons", Optics Letters vol.14, pp. 703,(1989)

[22] W. Zhao, E. Bourkoff, "Generation of dark solitons under a cw background using waveguide electro-optic modulators",Optics Letters, vol.9,pp. 405,(1990)

[23] N. J. Smith, F. M. Knox, N. J. Doran, K. J. Blow, and I. Bennion, "Enhanced power solitons in optical fibres with periodic dispersion management", Electron. Lett.,vol 32, pp. 54-55, (1996).

[24] Smith N.J., Doran N.J., Forysiak W., Knox F.M., "Soliton transmission using periodic dispersion compensation",Journal of Lightwave Technology, vol.15, pp. 1808-1822,(1997)

[25] Turitsyn S.K., Fedoruk M.P., Shapiro E.G., Mezentsev V.K., Turitsyna E.G,"Novel approaches to numerical modeling of periodic dispersion-managed fiber communication systems",Journal of Selected Topics in Quantum Electronics,vol.6, pp. 263-275,(2000)

[26] D. N. Christodoulides and E. D. Eugenieva, " Blocking and Routing Discrete Solitons in Two-Dimensional Networks of Nonlinear Waveguide Arrays ", Phys. Rev. Lett. vol. 87,pp. 233901-1 - 233901-4,(2001)

[27] Michal Matuszewski, Marek Trippenbach, Eryk Infeld, Boris A. Malomed, "Stabilization of Light Bullets by a Transverse Lattice in a Kerr Medium with Dispersion Management", Nonlinear Guided Waves and their Applications conference proceedings NLGW (2005),WD22

[28] R. W. Boyd and D. J. Gauthier, Slow and Fast Light, in Progress in Optics, Vol. 43, E. Wolf, Ed. (Elsevier, Amsterdam, 2002), Ch.6, pp. 497-530.

[29] J. C. Knight, "Photonic crystal fibres", Nature, pp. 424-847 (2003)

[30] Snitzer E., Osterberg H,"Observed dielectric waveguide modes in the visible spectrum", J.opt.Soc.Am., vol 51, pp. 499 - 505,(1961)

[31] A.Simon and R.Ulrich, "Evolution of polarization along a single mode fiber", Appl. Phys. Lett., Vol. 31,pp. 517 - 520,(1977)

[32] V. Ramaswamy and W.S.Froch, "Influence of noncircular core on the polarization performance of single mode fibers", Electron. Lett.,vol. 14, pp. 143-144,(1978)

[33] S. C. Rashleigh and R. Ulrich, "Polarization mode dispersion in single-mode fibers", optics letters, Vol. 3, pp.60-62, (1978)

[34] Marcuse, D.; Chinlon Lin, "Low dispersion single-mode fiber transmission–The question of practical versus theoretical maximum transmission bandwidth", IEEE Journal of Quantum Electronics,vol. 17, pp. 869 - 878,(1981)

[35] C.D. Poole and C.R. Giles, "Polarization-dependent pulse compression and broadening due to polarization dispersion in dispersion-shifted fiber", Optics Letters, vol. 13, pp. 155-157, (1988)

[36] Eugenio Lannone, Francesco Matera, Antonio Mecozzi, Marina Settembre, "Nonlinear Optical Communications Networks", John Wiley & sons, (1998)

[37] Artiglia M. et al., "Mode Field Diameter Measurements in Single-Mode Optical Fibres" , IEEE Journal of Lightwave Technology,vol. 7, pp. 1139-1152, (1989)

[38] Namihira Y., "Relationship Between Nonlinear Effective Area and Modefield Diameter for Dispersion Shifted Fibres" , Electronics Letters,vol. 30, pp. 262-263, (1994)

[39] Namihira Y., "Wavelength Dependence of Correction Factor on Effective Area and Mode Field Diameter for Various Singlemode Optical Fibres" , Electronics Letters,vol. 33, pp. 1483-1485, (1997)

[40] C.R.Menyuk, "Nonlinear Pulse Propagation in Birefringent Optical Fibers", IEEE Journal of Quantum Electronics, vol. QE-23,pp. 174,(1987)

[41] D.Marcuse, "Light Transmission Optics", Van Nostrand Reinhold, New York (1982), Second Edition

[42] Gerd Keiser, "Optical fiber communications", McGraw-Hill Inc., New York (1989), Second Edition

[43] N.A.Olsson,"Lightwave systems with optical amplifiers",IEEE Journal of Lightwave Technology,vol. 7,pp.1071-1082 , (1989).

[44] R.C.Steele,G.R.Walker,N.G.Walker, "Sensitivity of optically preamplified receivers with optical filtering", IEEE Photonics technology letters,vol.3,pp.545-548,(1991)

[45] T.Mukai, Y. Yamamoto, and T.Kimura, "S/N and Error rate performance in AlGaAs semiconductor laser Preamplifier and linear Repeater systems",IEEE Journal of Quantum ELectronics, vol. QE-18,No.10,pp. 1560-1568,(1982)

[46] M.Eberhard and Keith Blow, "Numerical Q parameter estimates for scalar and vector models in optical communication system simulations",Opt.comms,vol.249,pp.421-429,(2005)

[47] M.Eberhard and K.J.Blow "Semi-analytical Q parameter estimate in linear and nonlinear transmission systems",Nonlinear Guided Waves and Their Applications proceedings, ThB4(2005)

[48] Kaminow, I.,"Polarization in optical fibers" , IEEE Journal of Quantum Electronics, vol. 17, Issue 1, pp.15 - 22,(1981)

[49] C.D.Poole, R.E.Wagner, "Phenomenological Approach to Polarisation mode dispersion in long-single mode fibres", Electronics Letters, vol.22, pp.1029-1030 ,(1986)

[50] E.Hecht "OPTICS", Addison Wesley Longman Inc., New York,(1998),Third Edition

[51] W. Schurcliff, "Polarized Light", Harvard U. Press, Cambridge Mass., (1962)

[52] Mueller H., " The foundation of optics", J. Opt. Soc. Am.,vol. 38, pp.661,(1948)

[53] Walker M.J., "Matrix calculus and the Stokes Parameters of Polarized radiation",Am.J.Physics.,vol. 22,pp. 170-174,(1954)

[54] WS.Bickel and WM.Bailey,"Stokes Vectors, Mueller Matrices and Polarized Scattered Light", Am.J.Physics.,vol. 53,pp. 468-478,(1985)

[55] G. G. Stokes, "On the composition and resolution of streams of polarized light from different sources," Trans. Cambridge Phil. Soc.,vol. 9, pp.399, (1852).

[56] E.Hecht,"Note on an Operational Definition of the Stokes parameters",Am.J.Phys.,vol.38,pp.1156,(1970)

[57] G.J.Foschini and C.D.Poole, "Statistical Theory of Polarization Dispersion in Single Mode Fibers",J.Lightwave Technol.,vol.9,pp.1439-1456,(1991)

[58] Magnus Karlsson and Jonas Brentel "Autocorrelation function of the polarization-mode dispersion vector",Optics letters,Vol. 24, pp. 939-941,(1999)

[59] C.R.Menyuk and P.K.A.Wai, "Polarization evolution and dispersion in fibers with spatially varying birefringence",J.Opt.Soc.Amer.B,vol. 11,pp. 1288-1296,(1994)

[60] P.K.A.Wai and C.R.Menyuk, "Polarization mode dispersion decorrelation and diffusion in optical fibers with randomly varying birefringence", J.Lightwave.Technol.,vol.14,pp.148-157,(1996)

[61] D.Marcuse, C. R. Menyuk and P. K. A. Wai, "Application of the Manakov-PMD Equation to Studies of Signal Propagation in Optical Fibers with Randomly Varying Birefringence", Journal of Light. Tech., Vol. 15, pp. 1735 - 1746, (1997)

[62] C. R. Menyuk, "Application of multiple-length-scale methods to the study of optical fiber transmission", Journal of Engineering Mathematics, Vol.36, pp. 113 - 136, (1999)

[63] C. R. Menyuk, "Interaction of nonlinearity and polarization mode dispersion", Journal of Opt.Fiber.Comms.Rep.1, pp. 305 - 307,(2004)

[64] P.K.A.Wai and C.R.Menyuk, "Polarization decorrelation in optical fibers with randomly varying birefringence",Opt.Leters.,vol.19,pp.1517-1519,(1994)

[65] P.K.A.Wai and C.R.Menyuk, "Anisotropic diffusion of the state of polarization in optical fibers with randomly varying birefringence",Opt.Letters.,vol.20,pp.2493-2495,(1995)

[66] P.K.Wai, C.R. Menyuk and H.H.Chen, "Stability of solitons in randomly varying birefringent fibers",Opt.Lett.16,1231-1233(1991).

[67] S.C.Evangelides ,L.F.Mollenauer, J.P. Gordon and N.S.Bergano, "Polarization multiplexing with solitons", J.Lightwave Technology 10, pp. 28-35 (1992)

[68] R. Khosravani, I. T. Lima, P. Ebrahimi, E. Ibragimov, A. E. Willner, and C. R. Menyuk "Time and Frequency Domain Characteristics of Polarization-Mode Dispersion Emulators", IEEE Photonics Technology Letters, Vol. 13,pp. 127-129,(2001)

[69] Ivan T. Lima, Jr., Reza Khosravani, Paniz Ebrahimi, Edem Ibragimov, Curtis R. Menyuk and Alan Eli Willner "Comparison of Polarization Mode Dispersion Emulators", Journal of lightwave technology, vol. 19, pp. 1872-1881, (2001)

[70] M. Eberhard and C. Braimiotis, "Numerical implementation of the Manakov-PMD equation with precomputed M(ω) matrices", Nonlinear Guided Waves and Their Applications proceedings,MC3(2004).

[71] C. Braimiotis and M. Eberhard, "Numerical implementation of the coarse step method with a varying differential group delay", Proc. of Conference on Optical Networks and Technologies (OpNeTec), page 530-534, Pisa, Italy, October 2004, Consorzio Nazionale Interuniversitario per le Telecomunicazioni (CNIT)

[72] C. Braimiotis, M. Eberhard and K. Blow, "Polarisation mode dispersion correlations with the coarse-step method", Opt. Comm. 262, pp. 135-139, 2006

[73] Brian S. Marks, Ivan T.Lima,Curtis R.Menyuk,"Autocorrelation function for polarization mode dispersion emulators with rotators",Optics Letters Vol. 27,pp. 1150 - 1152,2002

[74] Braimiotis and M. Eberhard, "Numerical implementation of low-PMD spun fibres with precomputed M(w) matrices", Proc. on Postgraduate Research Conference

in Electronics, Photonics, Communications and Networks, and Computing Science (PREP), page 100-101, Lancaster, UK, March 2005, University of Lancaster

[75] C. Braimiotis and M. Eberhard,"Application of the Manakov-PMD equation to a computational investigation of low-PMD fibres", Techn. Digest Series, Conference on Nonlinear Guided Waves and Their Applications (NLGW), page ThB8, Dresden, Germany, September 2005, Optical Society of America

[76] Andrea Galtarossa, Luca Palmieri and Anna Pizzinat, "Low-PMD spun fibers", Venice Summer school proceedings on Polarization Mode Dispersion, Tuesday 08, pp.1-5,(2002).

[77] Daniel A.Nolan, Xin Chen, Ming-Jun Li, "Fibers With Low Polarization-Mode Dispersion",J.Lightwave Tech. 22, pp. 1066-1077(2004).

[78] R. Ulrich and A. Simon, "Polarization optics of twisted single-moded fibers" Appl. Opt,vol. 18, pp. 2241- 2251,(1979)

[79] C.R.Menyuk "Pulse propagation in an elliptically birefringent Kerr medium", IEEE J.Quantum Electron,vol.25, pp. 2674-2682,(1989)

[80] Manakov S.V., "On the theory of two-dimensional stationary self-focusing of electromagnetic waves", Soviet Physics JETP 38, pp. 248-253, (1974)

[81] C. S. Gardner, J. M. Greene, M. D. Kruskal and R. M. Miura, "Method for solving the Korteweg-de Vries equation", Phys. Rev. Lett. 19, pp. 1095-1097, (1967).

[82] R.M. Miura, "Bcklund Transformations, the Inverse Scattering Method, Solitons, and Their Applications" Springer-Verlag, New York, (1974)

[83] R. M. Miura, "Korteweg-de Vries equation and generalization. I. A remarkable explicit nonlinear transformation", J. Math. Phys. 9,pp. 1202-1204, (1968)

[84] A. Hasegawa and M. Matsumoto, "Optical solitons in fibers", Springer ,London (2002)

[85] Mark J. Ablowitz and Harvey Segur, "Solitons and the inverse scattering transform", Publication Philadelphia, SIAM, 1981

[86] M. J. Ablowitz and P. A. Clarkson, "Solitons nonlinear evolution equations and inverse scattering", Cambridge University Press, Cambridge, 1991.

[87] S. Novikov "Theory of solitons, the inverse scattering method" , Contemporary Soviet mathematics Series, New York (1984)

[88] P.D. Lax, "Integrals of Nonlinear Equations of Evolution and Solitary Waves", Comm. Pure Appl. Math.,vol 21,pp. 467-490 (1968)

[89] V.E. Zakharov and L.D. Faddeev, "Korteweg-deVries Equation: A Completely Integrable System", Funct. Anal. Appl.,vol 5,pp. 280-287, (1972)

[90] G. L. Lamb Jr., "Elements of soliton theory", Wiley, New York, (1980)

[91] V.E. Zakharov, E.I. Schulman, "To the integrability of the system of two coupled nonlinear Schrdinger equations", Physica D 4,pp. 270-274, (1982)

[92] K. J. Blow, N. J. Doran, and D. Wood, "Polarization instabilities for solitons in birefringent fibers", Optics Letters 12,pp. 202-204, (1987)

[93] D. N. Christodoulides, R. I. Joseph, "Vector solitons in birefringent nonlinear dispersive media", Optics Letters, Vol. 13, pp. 53-55, (1988)

[94] Tetsuji Ueda and William L. Kath,"Dynamics of coupled solitons in nonlinear optical fibers", Phys. Rev. A 42, pp. 563-571, (1990)

[95] Masato Hisakado, Takeshi Iizuka and Miki Wadati, "Coupled Hybrid Nonlinear Schrdinger Equation and Optical Solitons", Journal of the Physical Society of Japan Vol. 63, pp. 2887-2894, (1994)

[96] C.R.Menyuk,"Stability of solitons in birefringent optical fibers, I:Equal propagation amplitudes", Optics letters Vol.12, pp. 614 - 616, (1987)

[97] C.R.Menyuk,"Stability of solitons in birefringent optical fibers, II:Arbitrary amplitudes", J.Opt.Soc.Am.B, Vol.5, pp.392 - 402, (1988)

[98] Yuri S. Kivshar, "Soliton stability in birefringent optical fibers: analytical approach", J.Opt.Soc.Am.B, Vol. 7, pp. 2204-2209, (1990)

[99] R. J. Dowling, "Stability of solitary waves in a nonlinear birefringent optical fiber", Phys. Rev. A,vol. 42,pp. 5553-5560, (1990)

[100] Boris A. Malomed, "Polarization dynamics and interactions of solitons in a birefringent optical fiber", Phys. Rev. A,vol. 42,pp. 410-423, January 1991

[101] B. A. Malomed, S. Wabnitz, "Soliton annihilation and fusion from resonant inelastic collisions in birefringent optical fibers", Optics Letters, Vol. 16, pp. 1388-1390, (1991)

[102] V. K. Mesentsev and S. K. Turitsyn, "Stability of vector solitons in optical fibers," Optics Letters, vol. 17, pp. 1497-1499, (1992)

[103] X. D. Cao, C. J. McKinstrie, "Solitary-wave stability in birefringent optical fibers", J.Opt.Soc.Am. B, Vol. 10, pp. 1202-1207, (1993)

[104] I. J. Good, "The interaction algorithm and practical Fourier analysis", J. Roy. Statist. Soc., vol. B 20, pp. 361-372, (1958).

[105] J. W. Cooley and J. W. Tukey, "An algorithm for machine calculation of complex Fourier series", Math. Comp., vol. 19,pp. 297-301, (1965)

[106] W. H. Press, B. P. Falnnery, S. A. Teukolsky, and W. T. Vettering, "Numerical recipes in C: the art of scientific computing", Cambridge University Press, New York, (1988).

[107] L. Auslander, J.R. Johnson, and R.W. Johnson, "Multidimensional Cooley-Tukey algorithms revisited", Adv. in Appl. Math. 17 , pp. 477-519, (1996)

[108] E. O. Brigham, "The fast Fourier transform and its applications", Prentice Hall Signal Processing Series, Englewood Cliffs, NJ (1988)

[109] Matteo Frigo Steven G. Johnson, "The Fastest Fourier Transform in the West", MIT-LCS-TR-728 , also see http://www.fftw.org/fftw-paper.pdf,(1997)

[110] Matteo Frigo and Steven G. Johnson, "FFTW: AN ADAPTIVE SOFTWARE ARCHITECTURE FOR THE FFT", ICASSP conference proceedings, vol. 3, pp. 1381-1384, also see http://www.fftw.org/fftw-paper-icassp.pdf,(1998)

[111] Matteo Frigo, "A Fast Fourier Transform Compiler", Proceedings of the 1999 ACM SIGPLAN Conference on Programming Language Design and Implementation (PLDI '99), Atlanta, Georgia, also see http://www.fftw.org/pldi99.pdf,(1999)

[112] FFTW manual for FFTW version 2.1.5, vol. 26, http://www.fftw.org/fftw2_doc/,(2003)

[113] http://www.fftw.org/

[114] C.G. Lambe C.J. Tranter, "Differential equations for engineers and scientists", English Univ. P., London ,(1961)

[115] Oksendal Bernt, "Stochastic differential equations, an introduction with applications", Springer-Verlag, Berlin, New York, (1985)

[116] Ito Kiyosi, "Foundations of stochastic differential equations in infinite dimensional spaces", Society for Industrial and Applied Mathematics, Philadelphia. (1984)

[117] G.S. Ladde and M. Sambandham, "Stochastic versus deterministic systems of differential equations", Marcel Dekker,New York,(2004)

[118] Kreyszig Erwin, "Advanced engineering mathematics" 8th edition, Wiley, New York, Chichester, (1999)

[119] Jeffrey Alan, "Mathematics for engineers and scientists" 6th edition, Chapman and Hall, (2005)

[120] N.S. Koshlyakov, M.M. Smirnov and E.B. Gliner, "Differential equations of mathematical physics", translated by Scripta Technica Inc., Amsterdam, (1964)

[121] Robinson James C., "An introduction to ordinary differential equations", Cambridge University Press,Cambridge, (2004)